Chair of Hydrological Modeling and Water Resources

Albert-Ludwigs-University of Freiburg i. Br.

Tamara Leins

Impact of climate and land-use change on transport characteristics in a large karst aquifer in Slovenia

MSc-Thesis under the guidance of Prof. Dr. Andreas Hartmann
Freiburg i. Br., April 2022

Chair of Hydrological Modeling and Water Resources

Albert-Ludwigs-University of Freiburg i. Br.

Tamara Leins

Impact of climate and land-use change on transport characteristics in a large karst aquifer in Slovenia

Examiner: Prof. Dr. Andreas Hartmann
Co-examiner: Dr. Natalie Orlowski
Scientific Advisor: Dr. Cyril Mayaud

MSc-Thesis under the guidance of Prof. Dr. Andreas Hartmann
Freiburg i. Br., April 2022

Acknowledgements

I would like to gratefully thank many people who helped me in this process of completing my master thesis. First, I want to thank my supervisor Prof. Dr. Andreas Hartmann for making this thesis possible by providing the topic and letting me participate in this interesting project and also for his advice and support throughout the thesis. Then, I want to thank Dr. Natalie Orlowski for agreeing to be my co-examiner. And also a big thank you to the great team at the Karst Research Institute in Postojna for having me there as a guest and providing me with an office place and with great opportunities to join them in the field. Especially thank you to Dr. Cyril Mayaud, AdjProf. Dr. Nataša Ravbar and AdjProf. Dr. Metka Petrič for their scientific advice on the project. And thank you to Dr. Cyril Mayaud for the excellent mentoring throughout the thesis. I also would like to thank the team of the Chair of Hydrological Modeling and Water Resources at the University of Freiburg for their company in the office and for always being supportive when I needed some help. Here especially thank you to Dr. Yan Liu for helping me out with my modelling and to Mirjam Scheller for introducing me to the project and also being open to questions throughout my thesis. And last but not least, thank you to my friends for not only supporting me with my thesis, but especially for the moral support through some stressful periods. A special thank you here to my HydrologinnenAG for agreeing to be my last-minute correctors and also for making my whole master's program such a great time. And of course, thank you to my family for always being so supportive, not only during my master thesis, but throughout my entire life.

Table of Contents

Table of Figures

Table of Tables

List of Abbreviation

Symbol	Unit	Description
A	[km²]	Recharge area
α	[-]	Albedo
$(a_s + b_s)$	[-]	Fraction of extra-terrestrial radiation reaching earth on clear-sky days
α_{fsep}	[-]	Distribution coefficient of diffuse and concentrated recharge
α_{GW}	[-]	Groundwater variability constant
α_{SE}	[-]	Soil and epikarst distribution coefficient
c	[-]	Standardised tracer concentration
c_p	[MJkg^{-1}°C^{-1}]	Specific heat of the air
Ca^{2+}		Dissolved calcium
$CaCO_3$		Calcite
CH_4		Methane
CO_2		Carbon dioxide
D_L	[m²*s^{-1}]	Longitudinal dispersion coefficient
d	[m]	Zero plant displacement height
d_r	[-]	Inverse relative distance Earth-Sun
Δt	[d]	Modelling time step
Δ	[kPa °C^{-1}]	Slope vapour pressure curve
δ	[rad]	Solar decimation
E_{act}	[mm]	Actual evapotranspiration
Ec_{pot}	[mm day^{-1}]	Potential evaporation from interception over the vegetated fraction
E_{pot}	[mm]	Potential evapotranspiration
Es_{pot}	[mm day^{-1}]	Potential bare soil evaporation rate over the bare soil fraction
e_a	[kPa]	Actual vapour pressure
e_s	[kPa]	Saturation vapour pressure
$(e_s - e_a)$	[kPa]	Saturation vapour pressure deficit
f_C	[-]	Separation factor
φ	[rad]	Latitude
G	[MJm^{-2} day^{-1}]	Soil heat flux density
$guessAD$	[m]	Estimated actual distance from tracer injection point to spring
γ	[kPa °C^{-1}]	Psychrometric constant
G_{so}	[MJm^{-2}day^{-1}]	Solar constant
h	[m]	Crop height
H_2O		Water
HCO_3^-		Bicarbonate
i	[-]	Number of model compartment
J	[-]	Number of the day in the year
k	[-]	Von Karman's constant
K_C	[d]	Conduit storage coefficient
K_{epi}	[d]	Mean epikarst storage coefficient
K_{GW}	[d]	Groundwater storage coefficient

$K_{max,epi}$	[d]	Maximum epikarst storage coefficient
K_t	[sday^{-1}]	Time conversion factor
KGE		Kling-Gupta-Efficiency
LAI	[-]	Leaf area index
LAI_{max}	[-]	Annual maximum value of the LAI during growing season
LAI_{min}	[%]	Percentage reduction in the LAI during dormant season
λ	[MJkg^{-1}]	Latent heat of the vaporisation of water
m asl		Meters above sea level
μ	[variable]	Mean
N	[-]	Number of total model compartments
n	[h]	Actual duration of sunshine
N_m	[h]	Maximum possible duration of sunshine
N_2O		Nitrous oxide
σ	[MJK^{-4}m^{-2}day^{-1}]	Stefan-Boltzmann constant
P	[mm]	Precipitation
p	[kPa]	Atmospheric pressure
Q_{epi}	[mm d^{-1}]	Epikarst outflow
Q_{GW}	[mm]	Groundwater contribution
Q_{inj}	[m³s^{-1}]	Discharge recorded during tracer injection
Q_{main}	[m³s^{-1}]	Spring discharge
Q_{mean_cal}	[m³s^{-1}]	Mean discharge during the tracer experiment
Q_{peak}	[m³s^{-1}]	Peak discharge assigned to a certain tracer breakthrough curve
Q_{surf}	[mm]	Surface runoff
r	[-]	Linear correlation coefficient
r_a	[sm^{-1}]	Aerodynamic resistance
$r_{a,can}$	[sm^{-1}]	Canopy aerodynamic resistance
$r_{a,soil}$	[sm^{-1}]	Soil aerodynamic resistance
ρ_a	[kgm^{-3}]	Air density
R_a	[MJm^{-2}day^{-1}]	Extra-terrestrial radiation
R_n	[MJm^{-2} day^{-1}]	Net radiation at the crop surface
R_{conc}	[mm]	Concentrated groundwater recharge
R_{diff}	[mm]	Diffuse groundwater recharge
R_{epi}	[mm]	Recharge from the soil to the epikarst
R_{nl}	[MJm^{-2}day^{-1}]	Outgoing net longwave radiation
R_{ns}	[MJm^{-2}day^{-1}]	Incoming net shortwave/solar radiation
R_s	[MJm^{-2}day^{-1}]	Solar radiation
R_s/R_{so}	[-]	Relative shortwave radiation
R_{so}	[MJm^{-2}day^{-1}]	Clear-sky radiation
$r_{s,can}$	[sm^{-1}]	Canopy surface resistance
$r_{s,soil}$	[sm^{-1}]	Soil surface resistance
r_{st}	[sm^{-1}]	Stomatal resistance
RCP		Representative concentration pathway
RH_{max}	[%]	Maximum relative humidity

RH_{min}	[%]	Minimum relative humidity
Tn		Tracer test number n
T	[°C]	Air temperature
t	[s]	Time after tracer injection
t_0	[s]	Advection time
T_{pot}	[mm day^{-1}]	Potential transpiration rate over the vegetated fraction of the area
$T_{max,K}$	[K]	Maximum absolute temperature during the 24h-period
$T_{min,K}$	[K]	Minimum absolute temperature during the 24h-period
u_z	[ms^{-1}]	Wind speed at height z
V_e	[mm]	Mean epikarst storage capacity
V_{epi}	[mm]	Amount of water stored in the epikarst layer
$V_{GW,i}$	[mm]	Amount of water stored in the ground water layer
$V_{max,e}$	[mm]	Maximum epikarst storage capacity
$V_{max,S}$	[mm]	Maximum soil storage capacity
V_S	[mm]	Mean soil storage capacity
V_{soil}	[mm]	Amount of water stored in the soil layer
ω_s	[rad]	Sunset hour angle
x	[m]	Linear distance from tracer injection point to spring
z	[m]	Elevation above sea level
z_{0h}	[m]	Roughness length governing transfer of heat and vapour
z_{0m}	[m]	Roughness length governing momentum transfer
z_h	[m]	Height of humidity measurements
z_m	[m]	Height of wind measurements

Abstract

Karst aquifers play an important role in global water supply. Due to their intrinsic heterogeneity the quality and quantity of karst water resources can be very vulnerable to contamination as well as to environmental changes. In order to still use karst water resources in a sustainable and safe way, the assessment of their vulnerability is of great importance. However, most available methods for the assessment of karst vulnerability do not consider the influence of the hydrological conditions. If the impacts of changing environmental conditions on contaminant vulnerability should be evaluated, the consideration of the hydrological conditions in the vulnerability assessment is however essential. In this thesis, the impacts of climate and land-use change on transport characteristics in the catchment of the Unica Springs in southwestern Slovenia are analysed. This is achieved using a simple transport model based on the VarKarst discharge model. Correlations between transport parameters and flow and site characteristics are established using available tracer test data from the catchment area. These correlations are then used to predict simplified breakthrough curves based on discharge simulations of the VarKarst model. Climate and land-use scenarios for the catchment area are applied to the discharge and transport modelling. Initial and scenario simulations are compared to analyse the impacts of changes in climate and land-use on discharge and transport. The results show that using this method, most discharge and tracer test data can be reproduced by the model. The application of the climate and land-use scenarios to the model shows that the impact of the climate scenarios exceeds the impact of the land-use scenarios. The simulated changes are however never larger than the model uncertainty. However, for specific tracer tests shifts in simulated discharge and transport can be observed, which can lead to higher discharges and faster contaminant transport with higher maximum concentrations in the model, and could thus increase contaminant vulnerability. This modelling approach can be seen as a contribution to the quantitative vulnerability assessment in karst areas and in the analysis of possible impacts of future changes on karst water resources. But it also emphasises the need for continuous improvements in this field in order to ensure a safe management of karst water resources in the future.

Keywords: Karst aquifer, Transport modelling, Karst vulnerability, Climate Change, Land-use Change, Unica Springs, Slovenia

Zusammenfassung

Karstgrundwasserleiter spielen eine entscheidende Rolle in der weltweiten Wasserversorgung. Aufgrund ihrer charakteristischen Heterogenität können die Qualität und Quantität von Karstwasserressourcen jedoch sehr anfällig für Verunreinigungen und Umweltveränderungen sein. Um Wasserressourcen aus Karstaquiferen dennoch nachhaltig und sicher nutzen zu können, ist die Bewertung ihrer Vulnerabilität von großer Bedeutung. Die meisten verfügbaren Methoden zur Bewertung der Vulnerabilität von Karstaquiferen berücksichtigen jedoch nicht den Einfluss verschiedener hydrologischer Bedingungen. Dies ist allerdings von entscheidender Bedeutung, wenn die Auswirkungen veränderter Umweltbedingungen auf die Vulnerabilität von Karstaquiferen durch Schadstoffen bewertet werden sollen. In dieser Arbeit werden die Auswirkungen von Klima- und Landnutzungsänderungen auf die Transporteigenschaften im Einzugsgebiet der Unica-Quellen in Südwestslowenien analysiert. Dies wird mit Hilfe eines einfachen Transportmodells durchgeführt, das auf dem VarKarst-Abflussmodell basiert. Korrelationen zwischen Transportparametern und Abfluss- sowie Standorteigenschaften werden anhand verfügbarer Tracer-Testdaten aus dem Einzugsgebiet hergestellt. Diese Kor-relationen werden dann verwendet, um vereinfachte Durchgangsskurven auf der Grundlage von Ab-flusssimulationen des VarKarst-Modells vorherzusagen. Klima- und Landnutzungsszenarien für das Einzugsgebiet werden auf die Abfluss- und Transportmodellierung angewendet. Ausgangs- und Szenariosimulationen werden verglichen, um die Auswirkungen von Klima- und Landnutzungs-änderungen auf Abfluss und Transport zu analysieren. Die Ergebnisse zeigen, dass mit dieser Methode die meisten Abfluss- und Tracer-Testdaten vom Modell reproduziert werden können. Die Anwendung der Klima- und Landnutzungsszenarien auf das Modell zeigt, dass die Auswirkungen der Klimaszenarien die Auswirkungen der Landnutzungsszenarien übersteigen. Die simulierten Veränderungen sind jedoch nie größer als die Modellunsicherheit. Es sind jedoch einige Verschiebungen zu beobachten, die in bestimmten Zeiträumen zu höheren Abflüssen und schnellerem Schadstofftransport mit höheren Maximalkonzentrationen im Modell führen können und somit die Kontaminationsvulnerabilität erhöhen könnten. Dieser Modellierungsansatz kann Beitrag zu der quantitativen Bewertung der Vulnerabilität in Karstgebieten und bei der Analyse möglicher Auswirkungen zukünftiger Veränderungen auf Karstwasserressourcen angesehen werden. Er unterstreicht allerdings auch die Notwendigkeit kontinuierlicher Verbesserungen in diesem Bereich, um eine sichere Bewirtschaftung von Karstwasserressourcen in Zukunft zu gewährleisten.

Schlüsselwörter: Karstaquifer, Transportmodellierung, Vulnerabilität, Klimawandel, Landnutzungs-änderung, Unica-Quellen, Slowenien

1. Introduction

1.1 Introduction to Karst

Karst aquifers supply approximately one quarter of the world's population with drinking water (Ford and Williams, 2007). In the areas of Dinaric Karst, this proportion is even higher and for some countries it can exceed half of the demand (Stevanović and Eftimi, 2010). According to Iván and Mádl-Szőnyi (2017), the necessity to rely on freshwater from karst aquifers might even increase in the future due to a decline in surface water quality or due to the impacts of climate change. Karst aquifers show special and complex characteristics that distinguishes them from other groundwater systems. These characteristics arise in karst landforms as well as in karst hydrology and develop from a combination of well-developed secondary fracture porosity and high rock solubility (Ford and Williams, 2007; Bakalowicz, 2005).

Historically, the word "Karst" originates from the Kras region in Slovenia, where karst phenomena were first described by engineers and scientists. It is now used as a common basic expression to describe the flow conditions as well as landforms that occur mainly in the carbonate rocks limestone and dolomite (Bakalowicz, 2005). The term "karst rocks" refers to chemically soluble rocks, where carbonate rocks represent the most important proportion (Goldscheider and Drew, 2007). The solubility of karst rocks leads to their dissolution along the groundwater flow path, which is the most distinctive characteristic of karst according to Ford and Williams (2007). The dissolution of carbonate rock, which is represented by Calcite ($CaCO_3$), can be described by the simplified chemical equilibrium in equation (1).

$$CaCO_3 + H_2O + CO_2 \rightleftarrows Ca^{2+} + 2HCO_3^- \quad (1)$$

Dissolved calcium (Ca^{2+}) and biocarbonate (HCO_3^-) are the products of the equilibrium reaction. The carbon dioxide (CO_2) in equation (1) represents dissolved CO_2 in the water (H_2O). It originates from atmospheric CO_2 that is taken up by the water when raindrops form in the atmosphere. Its partial pressure in the water can be enhanced by vegetation or microbial processes when the water infiltrates into the soil. This partial pressure of CO_2 in the water as well as temperature or lithological factors influence the dissolution equilibrium (Hartmann et al., 2014a). This dissolution leads to a process called karstification, where karst aquifers form special features over long time periods. The features can be distinguished into endokarst, which describes features that developed underground like caves and conduits, and exokarst, which describes features that develop at the surface like karren, poljes, swallow holes or dolines (Ford and Williams, 2007). One of the largest geomorphological features in karst areas are large flat closed depressions, which are called poljes. They can get flooded regularly after intense rainfall or snowmelt. As a result of these floods intermittent lakes can arise in the poljes that can prevail for months (Mayaud et al., 2019). "Small-scale dissolution pit, groove and channel forms" are another typical karst landform and are referred to as karren (Ford and Williams, 2007). Natural depressions or holes in the ground are called dolines or sinkholes. They can be caused by surface dissolution or by karstification in the subsurface leading to a collapse of the surface layer (Hartmann et al., 2014a). A feature similar to dolines are swallow holes or ponors. In general, water drains in them towards the subsurface and even entire allogenic streams can infiltrate through them into the karst system (Hartmann et al., 2014a).

The existence of a solute which can be dissolved, mostly carbonate rocks, is one condition for the development of karst. Another condition is the existence of a groundwater flow, which flows according to a hydraulic gradient. In the process of karstification groundwater can then flow and transport the products of the dissolution process out of the system. This leads to a positive feedback loop, which makes karstification a very selective process. Higher flow rates through slightly wider fractures lead to higher calcite solution rates, which again lead to a faster growth of these fractures compared to narrower fractures. As a result, the slightly wider fractures become even wider and so on. In this way,

karstification leads to an increasing heterogeneity and to a progressing organisation into a hierarchical structure, allowing the development of a conduit system within the karst aquifer. These karst conduits can become several meters wide and kilometres long, while conduit flow can become a free surface flow with high flow rates and velocities (Hartmann et al., 2014a; Bakalowicz, 2005). This can lead to very complex and heterogeneous structures in karst aquifer systems (Ravbar et al., 2012).

This conduit system can also be referred to as the tertiary porosity of karst aquifers, including conduits, large fractures and caves which arise from the karstification process. The primary porosity or matrix porosity, which describes the micropores originating from the carbonate rock genesis, and the secondary or fracture porosity, small fissures and fractures that develop from tectonic processes, that also occur in karst aquifers are often referred to as the matrix system (Ford and Williams, 2007; Hartmann et al., 2014a; Geyer, 2008). A karst aquifer can also typically be distinguished into different zones. The main differentiation can be made between the vadose zone and the phreatic zone. The phreatic zone spreads below the water table, whereas the vadose zone is located between the water table and the ground surface. The two zones differ in their main direction of flow. In the phreatic zone water mostly flows horizontally, while water mostly percolates vertically through the vadose zone. In addition, the area between the minimum and maximum water table is referred to as the epiphreatic zone, which is thought to be the most active area of karst dissolution, while the topmost layer of carbonate rock close to the surface is referred to as epikarst (Fiorillo, 2014; Hartmann et al., 2014a). The formation of soil on limestone takes place only very slowly. This is due to the dissolution of almost all rock material, which then flows dissolved in water towards the karst springs and is thus transported out of the system. The basic mineral aggregate for soil development is only provided by a small percentage of insoluble material in the limestone (Kogovšek et al., 1999). The soil cover in karst regions is therefore usually clayey, very thin or even absent and the karst surface is very permeable (Kovačič et al., 2020).

In karst hydrology, the special characteristics of karst landscapes and aquifers lead to special characteristics in flow dynamics, hydrological properties and transport behaviour, which can differ a lot from other aquifer systems. In several processes there can be a duality. For example, infiltration into the ground cannot only happen in a diffuse way where the water percolates more slowly through the soil and the matrix, but also in a very concentrated way. This concentrated infiltration can happen through shafts, swallow holes or dolines and can reach the groundwater much more rapidly (Hartmann et al., 2014a; Fiorillo, 2014). Typically, diffuse and concentrated infiltration in karst systems can be very fast (Kovačič et al., 2020). Furthermore, in karst watersheds it can be differentiated between autogenic and allogenic recharge. Autogenic recharge comprises water recharging directly into the karst aquifer. Allogenic recharge on the other hand describes water that sinks into the karst aquifer but originates from neighbouring non-karst areas (Ravbar et al., 2012; Fiorillo, 2014). Karst aquifers also show a very high anisotropy and heterogeneity, which is mainly influenced by the position of the karst conduits and is created and organised by the groundwater flow (Bakalowicz, 2005). This leads to a strong and rapid hydrological variability with a duality in groundwater flow with slow diffuse flow on the one hand and fast conduit flow on the other hand (Malík, 2015). Low and continuous flow occurs in dry periods when discharge is dominated by matrix flow whereas during rainfall events, high spring discharges with a high temporal variability can occur and are dominated by flow through the karstic conduits (Hartmann et al., 2014a). Thus, karst springs can show very high flow rates with a high variability in discharge and the flow velocities in karst aquifers can become very high (Kovačič et al., 2020). The large variability in discharge and flow conditions leads to complex flow patterns, where the flow direction and rate can change depending on the hydrological conditions (Ravbar et al., 2012). Therefore, subsurface catchments in karst areas often differ from the topographical catchments and the lateral karst aquifer boundaries can be very variable (Stevanović, 2015). A conceptual model of a typical karst system as well as the characteristic processes that can occur in karst aquifers are visualised in Figure 1.

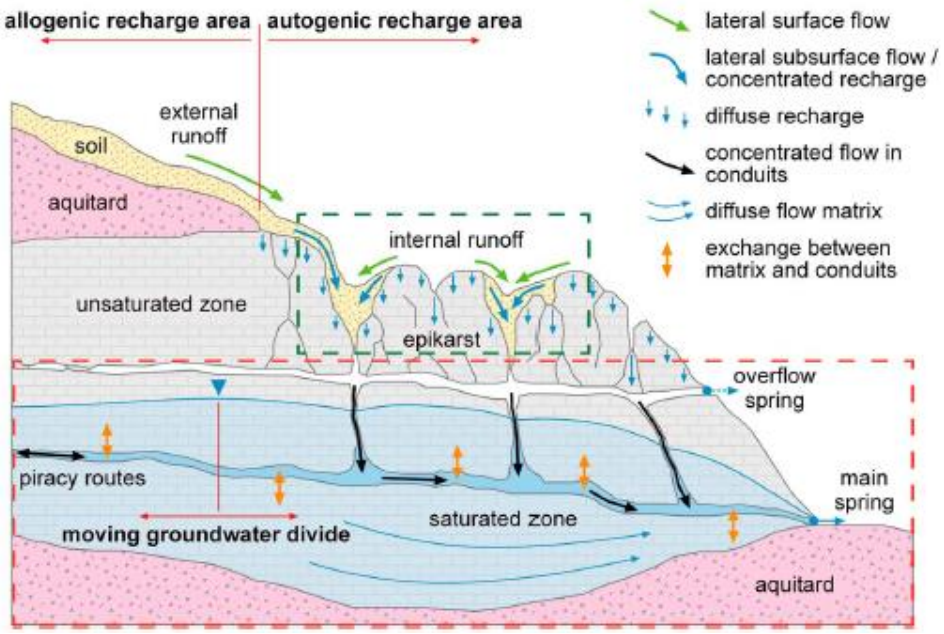

Figure 1: Conceptual model of a karst aquifer with characteristic processes (Hartmann et al., 2014a)

Compared to other less permeable systems, the hydrological processes in karst aquifers can make them especially susceptible to environmental changes (Kovačič et al., 2020). And as in a typical karst aquifer water can move very rapidly through the underground in fissures and conduits, pollutants can spread quickly and there can be very little attenuation leading to a high risk of pollution (Kogovšek et al., 1999; Goldscheider, 2000). According to Bakalowicz (2005), karst is therefore considered a very vulnerable medium and Ravbar et al. (2012) state that, compared to other hydrogeological environments, karst aquifers are more susceptible to contamination due to the special infiltration characteristics and the rapid conduit flow over long distances. This higher vulnerability of karst systems to contamination and environmental changes due to their special characteristics show the importance of the assessment of transport and contamination risk in karst systems. However, as stated by Ravbar et al. (2012), the prediction of groundwater or contaminant flow in karst aquifers can be very difficult due to their high complexity. And in general, the methodology used for analysis in classical hydrogeology like bore holes, pumping tests and distributed models are less successful or even invalid in karst aquifers as in karst the results of these methods cannot be simply interpolated to the whole aquifer (Bakalowicz, 2005). This is why for the analysis of karst systems, specialised investigation methods are necessary (Goldscheider and Drew, 2007).

Goldscheider and Drew (2007) introduce nine methods for the analysis of karst systems: speleological investigations, analysing the geological and geomorphological framework, hydrological methods, hydraulic methods, hydrochemical methods, isotopic methods, tracer techniques, geophysical methods and the modelling of karst hydrodynamics. According to Stevanović (2015) the used methods in analysing karst are not fundamentally different from methods used for porous media, they just need to be specially adapted. There is one group of methods that is very specific for karst areas: speleological techniques. They can for example be used for directly monitoring and sampling groundwater or for studying the conduit network. And while a lot of analysing methods were applied in and developed for porous aquifers and later adapted to karst systems, tracer techniques were first used in karst systems and later applied to other aquifer systems (Goldscheider and Drew, 2007). In the executing of artificial tracer tests, for instance a fluorescent dye is released into the aquifer at one point and the resulting concentration at one or more other points is recorded. The concentrations can be measured with manual or automatic sampling or in-situ by using fluorimeters. The application of artificial tracers can be useful for the investigation of different scientific questions in karst, for instance to assess vulnerability by

identifying flow pathways or quantifying travel times or in general to investigate how water or contaminants flow through the vadose zone and the phreatic zone (Gabrovšek et al., 2010). Especially in karst, this can differ with the prevailing hydrological conditions in the aquifer (Gabrovšek et al., 2010). Therefore, tracer tests executed at the same injection point can lead to different results depending on the hydrological condition. On the one hand it is important to consider the hydrological condition when interpreting tracer tests. On the other hand tracer tests executed (at the same injection point) at different hydrological conditions can further improve the understanding of a karst aquifer system. For instance Ravbar et al. (2012) conducted a multi-tracer test and combined it with time series analyses of natural tracers. In this way they investigated the hydraulic behaviour and characteristics of a karst system and were able to analyse how solutes are transported in the system depending on their recharge pathways.

1.2 Vulnerability assessment in karst areas

The high sensitivity and heterogeneity of karst aquifers in combination with their importance in water supply lead to the necessity of effective and accurate protection strategies in order to preserve the quality of karst groundwater resources (Daly et al., 2002). To establish protection measures, the vulnerability of the aquifer at different points needs to be assessed first. Different vulnerability methods are available for this purpose for different scales or data availabilities. The term vulnerability is for instance defined by Foster and Hirata (1988) as the characteristics that determine the sensitivity of different aquifer parts to a negative impact caused by imposed contamination. When vulnerability is assessed, different concepts of vulnerability can be distinguished. First, intrinsic and specific vulnerability can be differentiated. Intrinsic vulnerability describes the vulnerability of groundwater to anthropogenic contaminations by considering the characteristic geology, hydrology and hydrogeology of an area. However, the characteristics of the contaminants are not considered in the intrinsic vulnerability. The contaminant is therefore assumed to be conservative and behave like a water molecule. For specific vulnerability on the other hand, the characteristics of the contaminant are also considered as well as the possible interactions of the contaminant with the intrinsic vulnerability (Zwahlen, 2004; Daly et al., 2002; Iván and Mádl-Szőnyi, 2017). According to Daly et al. (2002) for the quantification of intrinsic vulnerability three aspects should be taken into account, which are the advection time, the relative contaminant amount that reaches the target and the physical attenuation that occurs, e.g. through dilution or dispersion. Another differentiation can be made between source and resource vulnerability regarding the target of the vulnerability assessment. While resource vulnerability refers to the groundwater table and therefore only considers the vertical transport of contaminants through the vadose zone, source vulnerability refers to a certain source, which could for instance be a spring or a well. In this case, also lateral contaminant transport through the phreatic zone is considered. This concept is for example applied in the identification of well protection zones in drinking water supply (Iván and Mádl-Szőnyi, 2017).

A variety of methods have been developed in order to assess groundwater vulnerability. The first detailed and often used approach, the DRASTIC method, was published by Aller et al. (1987). This DRASTIC method however, like many other approaches, was not specifically developed for the application in karst areas and therefore does not consider their special characteristics making them especially vulnerable compared to other hydrogeological systems (Moreno-Gómez et al., 2018; Iván and Mádl-Szőnyi, 2017). The first vulnerability method developed especially for karst areas is the EPIK approach, published by Doerfliger et al. (1999). It includes karst networks and the concentration of flow and therefore the heterogeneity of flow velocities in karst aquifers in the identification of different vulnerability classes, which can then be used to identify protection zones (Daly et al., 2002; Iván and Mádl-Szőnyi, 2017). Another important step in karst vulnerability assessment was the COST Action 620 (European Cooperation in the Field of Scientific and Technological Research) about “Vulnerability

and risk mapping for the protection of carbonate (karst) aquifers" (Zwahlen, 2004; Daly et al., 2002). The international cooperation project was in operation from 1997 until 2002 with the goal of defining a broad and consistent protection strategy for karst water resources. Basic concepts of karst aquifer vulnerability were clarified and the so called "European approach" was developed, which is a general, non-prescriptive karst groundwater protection approach that can be adapted to different local conditions (Zwahlen, 2004; Iván and Mádl-Szőnyi, 2017). It is based on an origin-pathway-target model, which serves as a basic theoretical background in almost all later literature (Iván and Mádl-Szőnyi, 2017). In this concept the origin or hazard refers to activities that can pose a threat to groundwater resources through the potential release of a contaminant. The target refers either to the groundwater resource in general or a certain source or abstraction point, as described earlier with a differentiation between resource and source vulnerability. The pathway describes everything between the target and the point where contaminants are released (Daly et al., 2002). In addition, the importance of a validation process for quality assurance as well as the need for more precise and physically based methods in vulnerability assessment arise from the COST Action 620 (Daly et al., 2002; Iván and Mádl-Szőnyi, 2017).

In the twenty-first century, many different vulnerability assessment methods for karst aquifers were developed. They can be classified into different groups in many ways. Iván and Mádl-Szőnyi (2017) for instance differentiate all methods into three groups: the qualitative, semi-quantitative and quantitative vulnerability methods. Statistical methods can also be a way of vulnerability assessment. They try to predict the probability of pollution or the contaminant concentrations based on observed data of aquifer properties, contaminant sources and occurrences in varying complexity. They are usually applied for specific contaminant issues at the local scale (Focazio, 2002). Qualitative and semi-quantitative methods are so called Parametric System Models, where several parameters are selected that are considered to be important for vulnerability. These parameters can comprise geomorphological, lithological, hydrogeological, hydrological, meteorological and pedeological information. The parameters are then classified, either into categories or into discrete intervals. The intervals or categories are then allocated to a value, which describes their relative vulnerability to contamination (Iván and Mádl-Szőnyi, 2017; Vrba and Zaporožec, 1994). The qualitative and semi-quantitative approaches can then be further differentiated into Matrix Systems, Point Count System Models or Rating Systems, depending on how the scores in a matrix are combined, cumulatively with weights or multiplicatively. An example for a method that uses both, a Matrix System and a Rating System, is the PI method developed by Goldscheider (2000). In this method two parameters, the protective factor P and the infiltration factor I are estimated to assess vulnerability. The P factor depends on how protective the layers between the ground surface and the groundwater are and is estimated using a Rating System. These layers include the soil, subsoil, non-karst rock as well as the unsaturated karst rock. The I factor describes the resulting vulnerability when the protective cover is bypassed due to lateral surface flow or subsurface flow. It is estimated according to a Matrix System and determines whether the relevant flow process is diffuse infiltration, surface flow or subsurface flow (Goldscheider, 2000; Iván and Mádl-Szőnyi, 2017). The already mentioned EPIK methodology by Doerfliger et al. (1999) is an example for a Point count system model. It determines vulnerability classes based on geomorphological and hydrogeological factors using weighting factors to emphasise the importance of specific features.

The results from qualitative and semi-quantitative vulnerability methods are usually classified maps that show the vulnerability of different areas. These maps can be a valuable tool in environmental management and an important step in the development of groundwater protection strategies. However, the generation of these maps is very conceptual and therefore subjective. Thus, when several methods are applied over the same study area, their results can be quite different or even contradictory. Furthermore, there is only a limited possibility for the validation of these qualitative and semi-quantitative methods. The possibility of estimating the reliability of a produced vulnerability map is however essential (Zwahlen, 2004). And in addition, the temporal variation of vulnerability due to

varying hydrological conditions are also not considered by these mapping methods (Butscher and Huggenberger, 2008). Due to these restrictions, scientific literature generally expresses the need for the development of more process- and physically based approaches to assess karst vulnerability in a quantitative way (Daly et al., 2002; Moreno-Gómez et al., 2018; Iván and Mádl-Szőnyi, 2017; Butscher and Huggenberger, 2008). Existing quantitative vulnerability methods will therefore be described more in detail in the following chapter.

1.3 Transport modelling in karst areas: quantitative vulnerability assessment

Quantitative process-based methods generally simulate the movement and transport of water and contaminant caused by physical and chemical processes (Iván and Mádl-Szőnyi, 2017; Focazio, 2002). Transport in karst systems can be influenced by many different factors. In general, like in porous aquifers, the important processes controlling solute transport are advection and dispersion as well as adsorption. The large heterogeneity of flow in karst aquifers has a large impact on contaminant transport and makes it a very complex process (Ghasemizadeh et al., 2012; Vesper et al., 2003). For instance Gabrovšek et al. (2010) showed with the execution of tracer tests that higher flow rates and flow velocities were connected to higher dispersivities. And of course the flow conditions also influence the advection velocity of solute transport. Also other studies emphasise that the hydrological flow conditions as well as the meteorological conditions, pre- and post-injection, highly impact transport processes in karst systems (Ravbar et al., 2012; Petrič et al., 2018; Field and Nash, 1997). In Chu et al. (2021) the influence of different parameters on the longitudinal dispersion coefficient was analysed for saturated flow in karst aquifers. They found that the average transport velocity of the tracer had the strongest impact on the longitudinal dispersion coefficient. Depending on the flow conditions, also different relationships of the longitudinal dispersion coefficient with the peak tracer concentration, with the time of peak tracer concentration, with the linear distance between injection point and receiving point, with the initial time of tracer breakthrough and with the aquifer porosity were observed. In general, they stated that the aquifer structure and the water flow state of the aquifer are the main factors that affect solute transport. The structure of the aquifer can impact contaminant transport by influencing the flow path of the contaminant. The specific mixture and distribution of the matrix, fissure and conduit permeability components as well as the conduits' geometry and connectivity, the flow length and the gradient play an important role here (White et al., 2018; Petrič et al., 2018). Also the thickness of the vadose zone and the occurrence of systems that promote concentrated infiltration, like dolines, can influence the dispersion and residence times of contaminants (Petrič et al., 2018). For retardation, different physical, chemical and biochemical processes are relevant. However, these processes also depend on the properties of the respective contaminant. For a specific contaminant, transport and storage can be determined by multiple, complex and interacting mechanisms (Vesper et al., 2003; Ghasemizadeh et al., 2012). Regarding tracer tests, usually dye tracers are assumed to be conservative, which means they are assumed to behave like water. However, their transport also depends on their real degree of conservative behaviour, which can vary between different tracer types (Petrič et al., 2018).

The first quantitative, process-based karst vulnerability approach is the VULK method published by Jeannin et al. (2001). The analytical computer program models advection-dispersion transport of a conservative contaminant and is based on transfer time mapping. Breakthrough curves are modelled along the contaminant pathway. The model structure consists of four to five sub-systems, depending whether resource or source vulnerability should be assessed, which are soil, subsoil, non-karst rock, unsaturated karst rock and, only for source vulnerability, the saturated zone. The model outputs are the transfer time, the maximum concentration and the duration of the contamination. Retardation and degradation are not taken into account and concentrated infiltration is not implemented in the model. Furthermore, the VULK approach is based on a steady-state flow modelling and therefore does not consider changes in hydrological conditions. The transport model is one-dimensional, it can however be

coupled with GIS in order to obtain a spatial vulnerability map (Iván and Mádl-Szőnyi, 2017). In general, numerical modelling is often used for the simulation of groundwater flow and solute transport. However, as previously mentioned, the high heterogeneity of karst aquifers makes the application of numerical models more challenging and limits the application of traditional methods (Ghasemizadeh et al., 2012).

There are two general types of modelling approaches for discharge or transport modelling: spatially lumped or spatially distributed models. In distributed models, the modelled aquifer is discretised into a grid of sub-units with specific properties. Specific conditions are assigned to the model boundaries. The differential flow and transport equations are then numerically solved for the modelled aquifer. While distributed modelling is very common for porous aquifers, in karst aquifers their model setup and calibration would require extensive field data. To estimate the exact occurring transport processes, a detailed description of the caves, conduits and fractures in the aquifer would be necessary. However, this extensive data is difficult to obtain and therefore rarely available for karst aquifers (Butscher and Huggenberger, 2008; Ghasemizadeh et al., 2012). There are still approaches that assumes that flow and transport behaviour in karst aquifers are equivalent to the flow and transport behaviour in porous media. This is for instance the case for the so-called Equivalent Porous Media (EPM) approach. It assumes that the karst rock matrix, fractures and conduits can be represented by an equivalent porous medium that, in a certain area, has equivalent hydraulic conductivity. This overall local conductivity is approximated with an enhanced equivalent conductivity. Especially in highly karstified aquifers and especially for solute transport however, the applicability of this approach is very limited (Ghasemizadeh et al., 2015).

In spatially lumped models on the other hand, the hydraulic, physical or chemical response of an aquifer is simulated globally and spatial variations in flow patterns or contaminant distribution are not considered. This leads to the great advantage that the data requirements are much lower than for spatially distributed models because the heterogeneous structure of the karst aquifer does not need to be known in detail. The parameterisation of these lumped models can however not be determined directly from physical, measureable processes. But well-calibrated lumped models can still be a good tool for the simulation of processes in karst aquifers as well as for the prediction of possible changes under uncertain conditions (Mudarra et al., 2019; Ghasemizadeh et al., 2012). An example for a lumped approach to numerical contaminant transport modelling in karst areas is the intrinsic vulnerability assessment method by Butscher and Huggenberger (2008). In this quantitative vulnerability approach spring discharged is modelled using a global approach with mixed reactor compartments to represent different flow systems. In addition, two vulnerability measures are introduced. The vulnerability index VI assesses the temporal variations of vulnerability of a spring based on the relative proportions of spring discharge that originate from the conduit system or from the matrix system. As discharge originating from the matrix system is assumed to be related to slower flow and therefore longer residence times with more effective processes of contaminant adsorption, degradation or filtration, the sensitivity of a karst spring to contamination is assumed to be reduced by a larger proportion of discharge from the matrix system. Furthermore, the vulnerability concentration Cv is introduced, which is the simulated concentration of a standard contaminant in spring water that results from a standardised contaminant input into the aquifer. In this simulation of contaminant transport using a mixed reactor model however, advection processes cannot be accounted for because the time-lag between the input of contaminant and the arrival at the spring cannot be modelled. Butscher and Huggenberger (2008) therefore state that their transport model is applicable to small catchments with short residence times, but the application to point-source contaminant transport in larger catchments is critical. Furthermore, flow through the unsaturated zone is not considered in their approach. In an extension to their previous study (Butscher and Huggenberger, 2008), Butscher and Huggenberger (2009a) extended their approach by integrating their numerical model with the EPIK vulnerability mapping approach (Doerfliger et al., 1999). They thereby

wanted to account for spatial as well as temporal aspects of vulnerability. This however still does not solve the limitations in modelling point-source contaminant transport.

One quantitative vulnerability approach that assesses resource vulnerability is the Time-Input method by Kralik and Keimel (2003). In this approach, contaminant transport is not modelled from an injection point to a spring or well but from the injection point at the surface to the uppermost groundwater body. The approach is specialised on mountainous areas and considers two main factors, the travel time from the surface to the groundwater and the amount of precipitation input as groundwater recharge. The two factors are weighted with approximately 60 % for the travel time factor and 40 % for the input factor. The vertical travel time for the travel time factor can be approximated by dividing the thickness of the overlying layers, like the soil and subsoil as well as the unsaturated zone, through the hydraulic conductivities of the respective layers. The classified input factor is used for the correction of the travel time factor and can be calculated according to a simple water balance considering precipitation, solar radiation, slope, vegetation and soil data. The vulnerability is therefore not expressed as a dimensionless number but as a real time. In this way the evaluation of the method results is much easier. However, it is also stated that the resulting time values are not really exact mean travel-times to the groundwater but rather indicate tendencies. The approach is based on "the mean bad conditions of a hydrological year" (Kralik and Keimel, 2003). Temporal variations in vulnerability or vulnerability during extreme events are not considered. Furthermore, the method considers the contaminants to behave like an ideal tracer and therefore assesses intrinsic vulnerability.

Another quantitative method by Živanović et al. (2016) for time-dependant vulnerability assessment specifically incorporates travel time components. It uses the Time-Input method by Kralik and Keimel (2003) for the simulation of vertical travel times through the unsaturated zone as one component. Additionally, a horizontal travel time component is considered based on the duality of flow in karst aquifers. Furthermore, a surface component towards ponor zones is considered by this method. The method by Živanović et al. (2016) is designed for groundwater protection zoning and therefore assesses source vulnerability. The study shows the advantages of vulnerability assessment that is based on flow travel time components. It reduces the subjectivity of vulnerability assessment by partly avoiding a parameterization of ranking of vulnerability. Furthermore, the resulting travel times are therefore easier to validate. This time-dependant vulnerability method can be applied to different hydrological conditions. However, it is stated that the results strongly depend on the level of exploration of the analysed area (Živanović et al., 2016).

Furthermore, there are some attempts at vulnerability assessment on the basis of the semi-distributed lumped process-based VarKarst discharge model. The model was first applied by Hartmann et al. (2013) and will be described in more detail in Chapter 3.2.2. Modelling tracer transport directly with the VarKarst model by adding the injected tracer to the model compartments, assuming complete mixing, was for instance attempted by Mudarra et al. (2019). Based on the VarKarst model, spring discharge as well as tracer test results are considered for the calibration of the model. Also two other independent methods, the Soil Water Balance and the APLIS approach for the estimation of mean annual autogenic recharge based on GIS (Andreo et al., 2008), are included in the approach for water resource evaluation. Based on information by these two methods and on field investigations, the ranges for parameter estimation are confined. The model estimates the contribution of allogenic and autogenic components to the total recharge in a quantitative way (Mudarra et al., 2019). However, as mentioned by Mudarra et al. (2019), the lumped structure of the VarKarst model is not able to model advection processes, which are however crucial in contaminant transport. Scheller (2020) specifically tested tracer transport modelling with the VarKarst model for the catchment of the Unica Springs. In a similar way to Mudarra et al. (2019) the parameter estimation is based on discharge data as well as on tracer test data. However, no parameter sets could be found which were able to predict all tracer tests as well as the discharge time-

series with a sufficient performance. Furthermore, it was not possible to account for advection processes of tracer transport.

1.4 Impacts of climate and land-use change on karst areas

The world's climate is warming, which is extremely likely caused by human activities. Anthropogenic emissions of greenhouse gases, which have increased since the pre-industrial era, have led to an increase in atmospheric concentrations of carbon dioxide (CO_2), methane (CH_4) and nitrous oxide (N_2O), leading to a warming of atmosphere and ocean. This warming has also affected other human or natural systems and processes, for instance the sea level is rising and the amounts of snow and ice are decreasing (Pachauri and Mayer, 2015).

The climate will continue to change in the future and will therefore also influence other systems and processes. However, to what extent changes will occur depends on the current greenhouse gas emissions as well as their development in the future (Bertalanič et al., 2019). In Pachauri and Mayer (2015), different Representative Concentration Pathway scenarios (RCPs) are introduced to quantify possible future developments of emissions. The different scenarios define different radiative forcings until the year 2100 relative to pre-industrial times. A larger radiative forcing corresponds to a larger enhancement of greenhouse effect. They are based on the emissions of air pollutants like CO_2, CH_4 or N_2O caused by human activities and depend on different global socio-economic developments and climate policies that influence for example land use change or primary energy and oil consumption. Examples for these socio-economic factors are the extent of population growth, the technological development or the change in gross domestic product during the 21st century (Bertalanič et al., 2019). These RCPs can be the basis for studies on future climate change and its impacts. They are indicated in W/m². There are four RCPs: the RCP2.6, the RCP4.5, the RCP6.0 and the RCP8.5, which correspond to a radiative forcing of 2.6 W/m², 4.5 W/m², 6.0 W/m² or 8.5 W/m² in the year 2100 compared to pre-industrial times. Pachauri and Mayer (2015) describe the RCP2.6 as a "stringent mitigation scenario", the RCP4.5 and RCP6.0 as intermediate scenarios and the RCP8.5 as a scenario with very high greenhouse gas emissions.

The changes in the climate system can also lead to changes in precipitation and evapotranspiration or to the melting of snow and ice and therefore lead to changes in hydrological systems. This can in tern affect the quantity and quality of available water resources (Pachauri and Mayer, 2015). Even though the changing climate is expected to influence water balance components around the world, there is no uniform pattern and the expected changes differ a lot between regions (Maček et al., 2018). The expected changes also vary in-between different seasons and can for instance lead to shifting precipitation patterns. In combination with changing meteorological variables, discharge quantities as well as river or spring regimes can be affected by these shifting precipitation patterns. In karst areas, these changes might even lead to an increase of the already high variability in flow and transport processes (Kovačič et al., 2020). Amongst other factors, the increase of extreme events can pose a threat to not only the quantity, but also the quality of spring water in karst areas (Ravbar et al., 2018). In different karst areas around the world climate related effects like a decrease in water resource quantities in the long term or an increase of extreme event frequencies in the short-term have already been observed (Kovačič et al., 2020). For instance, Wu et al. (2017) analysed discharge changes in a typical karst watershed in Southwestern China and the response of discharge changes to different driving factors for a time series from 1984 to 2015. They especially analysed the impacts of climate change and of human activities on changes in discharge. They found that discharge and precipitation will continuously decline in their persistent times. Evaporation on the other hand will continuously increase. They also found that while the contribution of climatic factors to discharge changes was high, the contribution of human activities to discharge changes was only low. Sapač et al. (2019) investigated the impact of climate change on the flow conditions of two karst rivers in Slovenia. They found that while there could be an increase in the

magnitude of extreme events as well as in mean discharge, low-flow indices could decrease. But they also show that due to a high uncertainty in climate change projections, the expected changes in discharge are not always clear. They furthermore emphasise that due to the large vulnerability of karst systems, more additional modelling and analysis should be conducted in order to further investigate the effects of climate change on the flow dynamics of karst rivers. Regarding the vulnerability of karst groundwater, Beaujean et al. (2014) state that even though the predicted changes in meteorological variables are recognised as a stress factor for groundwater resources, most groundwater vulnerability assessment studies and methods focus only on the issues of contamination and not on environmental changes. And according to Butscher and Huggenberger (2009b), while some studies have assessed the impact of climate change on groundwater resources, their focus was mostly on the amount of available water. But only very few studies focussed on the impacts of climate change on water quality and therefore on the vulnerability of groundwater to contamination. For one spring in northwest Switzerland, Butscher and Huggenberger (2009b) therefore modelled the effects of climate change on karst groundwater vulnerability using their method described earlier (Butscher and Huggenberger, 2008). They used two scenarios, the "summer heat wave" scenario and the "sever rainfall event" scenario for the analysis. For conduit flow vulnerability they show that for the "summer heat wave" scenario the impact of short-lived contamination is likely to decrease in their study site. For the "severe rainfall event" they state that conduit flow vulnerability "rises dramatically directly after the event". For the long-term they however state that for the "severe rainfall event" scenario conduit flow vulnerability slightly decreases due to an increase of recharge to the matrix flow system and therefore an enhanced dilution of the potential contaminant (Butscher and Huggenberger, 2009b). Overall, there are only few studies that assess the sensitivity of karst water resources to the effects of climate change, in spite of the important role of karst aquifers in water supply (Kovačič et al., 2020).

In addition to possible direct influences of changing climate conditions on the water balance components, changing weather patterns can also lead to changes in vegetation cover, especially the changing frequency and magnitude of extreme events. An example for climate induced changes in land-use is a changing share of forests due to large-scale forest disturbances caused by ice breakage, drought, natural fires or windthrows (Kovačič et al., 2020). Changes in land-use patterns can also be directly induced by anthropogenic activities, for example due to urbanisation and industrialisation. These changes of land-use composition can affect the water balance components like the evapotranspiration, recharge and discharge. They can therefore lead to changed water pathways and storage and thus influences the availability of water resources. Kovačič et al. (2020) for instance studied the influence of climate and land-cover changes on groundwater recharge and on spring discharge in two karst catchment areas in Slovenia. They found that in addition to climate changes, also vegetation cover changes can significantly impact spring hydrology. Changing vegetation covers can also affect the quality of water resources, for instance due to changes in filtration and nutrient or sediment load. However, the exact impacts on water resources caused by land-use change are not clear and can vary between regions. In different areas, a similar change of land-use can lead to different magnitudes or types of impacts. It is stated that also for karst systems, soil and vegetation play an important role in the water cycle. Changes in the land-use composition of a catchment can therefore also lead to short- and long-term impacts on the hydrology of karst springs. However, in the analysis of future developments in karst hydrology, the possible impacts of land-use have only rarely been considered (Glavan et al., 2013; Kovačič et al., 2020). And in addition, Sarrazin et al. (2018) state that there is not much knowledge on the combined impact of climate and land-use changes on karst hydrology at large scales.

1.5 Research gaps

To conclude from the literature review, due to the special characteristics of karst aquifers, they can be described as especially vulnerable to contamination as well as to environmental changes (Bakalowicz,

2005; Ravbar et al., 2012; Kovačič et al., 2020). In order to still protect and manage karst water resources in a sustainable way, special methods are necessary for the assessment of their vulnerability (Daly et al., 2002). There are some available qualitative and semi-quantitative methods for the creation of vulnerability maps. However, these methods are rather subjectivity, the possibilities for their evaluation are limited and they are unable to consider hydrological conditions in the assessment of vulnerability. The consideration of hydrological conditions in vulnerability assessment becomes especially important when possible impacts of future environmental changes should be accessed. Therefore, there is a need for more quantitative, physically-based vulnerability methods that simulate occurring transport processes in karst aquifers (Butscher and Huggenberger, 2008; Iván and Mádl-Szőnyi, 2017). In addition to the vulnerability of karst water resources to contamination, there is an increasing pressure due to environmental changes. Anthropogenic climate change as well as changes in land-use can affect the quantity and quality of karst water resources. However, only few studies have been conducted to assess the sensitivity of karst water resources to changing climate and land-use conditions (Kovačič et al., 2020). Therefore, there is also a lack of studies that focus on the impacts of climate change as well as land-use change on karst water resources. In this context, the necessity for the development and application of karst vulnerability methods that are able to consider hydrological conditions and their potential future changes becomes apparent.

1.6 Objectives

The main objectives of this thesis are the development and the application of a method for contaminant transport modelling in order to assess karst vulnerability under changing climate and land-use conditions. In this way, the lack of quantitative vulnerability assessment methods on the one hand and the lack of studies on the impacts of climate and land-use changes on karst water resources on the other hand should be addressed collectively.

The development of a simple transport model should be done on the basis of the VarKarst model by Hartmann et al. (2013), using tracer test data. The goal is not to model the exact observed tracer breakthrough curves, but to simulate the main transport characteristics that describe contaminant transport in a simplified way. In order to achieve this, the impact of hydrological conditions and aquifer structure on the transport in karst aquifers should be quantified and linked to observed transport characteristics. In the next step, these linkages should be used to predict transport characteristics depending on the hydrological conditions and the spatial characteristics of the tracer or contaminant injection point within the catchment area. The hydrological conditions are based on discharge simulations of the VarKarst model. For the consideration of land-use in the approach, a simple way of including land-use in the VarKarst model should be implemented.

To analyse the impacts of climate and land-use change on contaminant transport, scenarios of possible changes should be developed. Therefore, possible changes should be quantified by finding realistic values of future climate variables or land-use compositions. To finally analyse the impacts of changes in climate and land-use on transport characteristics and therefore on vulnerability, the defined future scenarios should be applied to the developed transport model.

2. Study site

2.1 Catchment area

The study site for this thesis is the catchment of the Unica Springs in south-western Slovenia, near the town of Postojna. It is located in the Dinaric karst, which extends from the South of Slovenia until northern Albania (Kovačič and Ravbar, 2010). Figure 2 shows the location of the catchment area.

With a catchment size of over 800 km² (Kovačič et al., 2020) the catchment of the Unica Springs can be described as a large karst system. The elevation in the catchment ranges from 450 m asl to 1796 m asl. Both autogenic and allogenic recharge through sinking rivers contribute to recharging the Unica River (Gabrovšek et al., 2010). Over 73 % of the catchment area is covered with rocks with karst porosity (Jurassic and Cretaceous limestones) while 13 % of the catchment area is composed of Triassic dolomites with a predominating fissured porosity (Kovačič and Ravbar, 2010). At the bottom of the poljes and along surface streams alluvial deposits from the Quaternary period occur and Triassic dolomite and Eocene flysch rocks can lead to surface runoff in some parts of the catchment area (Gabrovšek et al., 2010). Figure 2 shows the spatial distribution of the hydrogeological units composing the catchment area.

Within the catchment area three sub-catchments can be distinguished. The largest sub-catchment, located in the centre of the catchment area, is the Javorniki-Snežnik massif, a high karst plateau. The Javorniki range is a chain of mountains that runs northwest to southeast and is 11 kilometres wide and 30 kilometres long (Kovačič et al., 2020; Petrič et al., 2018). The highest elevations between 600 and 1300 m asl are reached in the central ridge of the Javorniki. The Javorniki plateau transitions into Snežnik towards the southeast. The Snežnik summit reaches an elevation of almost 1800 m asl (Petrič et al., 2018). The Javorniki karst plateau is covered with forest and is mostly uninhabited (Ravbar et al., 2012).The mountainous watershed consists of highly karstified Jurassic and Cretaceous limestones. These carbonate rocks can reach a thickness of over 1000 m (Ravbar et al., 2012). Plateaus with many dolines as well as conical hills are the typical landscapes in the Javorniki area. There are no river valleys or surface drainages. Furthermore, the soil in this sub-catchment can be very thin, all in all leading to a lot of direct infiltration of rainfall into the ground (Kovačič et al., 2020). In the underground there is assumed to be a typical karst aquifer with conduits and fissures, allowing rapid flow of water. This assumption is strongly supported by speleological data as well as the lithology tectonic structure (Kogovšek et al., 1999). The unsaturated zone in this area can be up to several hundred meters thick (Ravbar et al., 2012). Important groundwater quantities are located in the Javorniki karst plateau, which, especially during low-water level, contribute a significant proportion of water to the Unica Springs (Gabrovšek et al., 2010).

The two other sub-catchments are a series of karst poljes located on the north-eastern side of the Javorniki range as well as the Pivka River basin on the western side of the Javorniki range. The chain of four karst poljes at the eastern edge of the Javorniki plateau is distributed in the SE-NW direction (Gabrovšek et al., 2010) and has developed along a neo-tectonic strike-slip fault zone. Sinking rivers flow through these poljes towards the springs (Ravbar et al., 2012). From northwest to southeast the poljes are arranged as follows: Planinsko Polje, Cerkniško Polje, Loško Polje and Babno Polje (Petrič et al., 2018). The lowest polje is Planinsko polje with elevations between 444 and 447 m asl, which is approximately 10 km² large (Mayaud et al., 2019; Kovačič and Ravbar, 2010). Therefore, the general direction of water flow underground in this area is towards Planinsko polje. In the Dinaric karst Planinsko Polje is the westernmost active polje. It is frequently flooded after abundant rainfall or snowmelt in the catchment area (Mayaud et al., 2019; Kovačič and Ravbar, 2010; Blatnik et al., 2017). The next and biggest polje along the fault is Cerkniško polje with elevations between 547 m asl and 552 m asl, covering an area over 70 km² (Ravbar et al., 2021; Kovačič and Ravbar, 2010; Kogovšek et al.,

1999). Also water from a Triassic dolomite area east of the polje is gathered there. At high groundwater level flooding occurs in the Cerkniško polje and the intermittent Cerknica Lake is formed, which can have an extent of up to 30 km². Underground, water from Cerkniško Polje can flow directly to the springs of the Ljubljanica River in the North or it can flow towards the springs of Planinsko Polje through the hydrological system of Rakov Škocjan (Ravbar et al., 2012; Kovačič and Ravbar, 2010).

In the Pivka Valley west of the Javorniki plateau, impermeable Eocene flysch prevails. The elevation in the Pivka basin ranges from 500 to 600 m asl. The Pivka River flows here. At the north-eastern edge of the Pivka valley the Pivka River sinks and continues to flow underground towards Planinsko Polje. The Pivka River can therefore be described as a large allogenic input to the karst aquifer. The river runs through Postojnska Jama, a very well-developed cave system, and then flows to the Pivka branch of the cave Planinska Jama. With five known entrances and an explored system of over 24 km, Postojnska Jama is the second longest cave in Slovenia and it is the hydrological connection between the Pivka basin and Planinsko Polje. While the Pivka River flows through the Pivka Branch of Planinska Jama, there is another active river in Planinska Jama, the Rak River. It flows in the Rak Branch of Planinska Jama and discharges water from Cerkniško Polje over Karlovica, Zelške and Tkalca Jama. These two sub-surface river channels converge underground in Planinska Jama (Ravbar et al., 2012; Kaufmann et al., 2016).

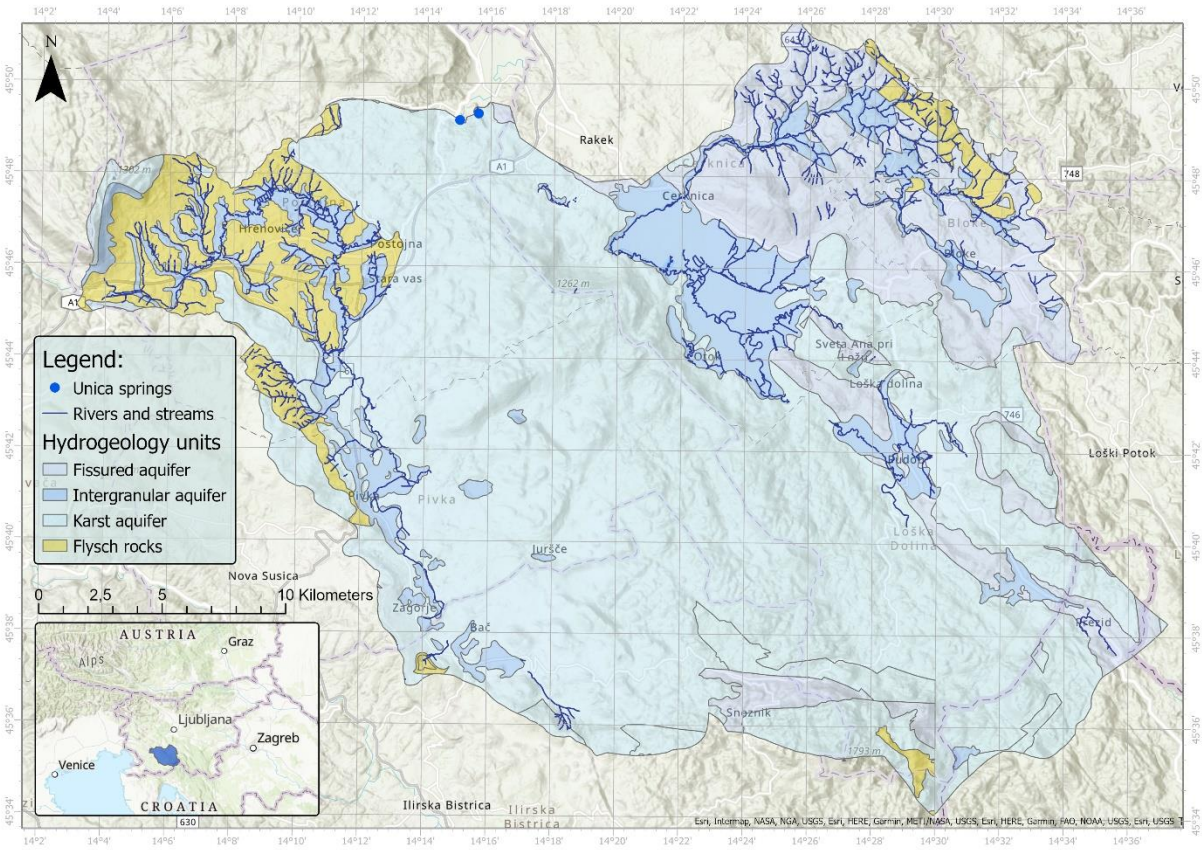

Figure 2: Hydrogeology and location of the catchment of the Unica Springs

The catchment is drained by a few overflow springs and 2 main springs, the Malenščica spring and the Unica spring, which will further be referred to cumulatively as the Unica Springs. The two permanent karst springs are located close to each other at the southern suburbs of Planinsko Polje and then join together into the Unica River. After crossing the polje surface, the Unica River sinks again on the western and northern edges of the polje. At the edge of the Ljubljana basin it then resurfaces as the

Ljubljanica River (Gabrovšek et al., 2010; Ravbar et al., 2012). The Ljubljanica continues to flow into the Save, which then flows into the Danube, which finally discharges to the Black Sea.

In spite of their close location, the two main springs differ in their hydrodynamic, their hydrochemistry as well as their morphology (Ravbar et al., 2012). The Malenščica spring emerges from a narrow pocket valley. Between an elevation of 448 m asl and 470 m asl, the spring diffusely flows out of a system of many orifices. Due to its quantity and quality, the Malenščica spring is used as the drinking water source for Postojna and Pivka, supplying the two municipalities with over 20000 inhabitants (Ravbar et al., 2012; Gabrovšek et al., 2010). The mean discharge of Malenščica spring is 6.7 m^3/s with a range from 1.1 m^3/s to 9.9 m^3/s (Gabrovšek et al., 2010). At high-water levels the discharge is constrained because surplus waters are directed towards the other main spring through underground conduits (Ravbar et al., 2012; Kaufman et al., 2020). East of Malenščica spring some smaller temporary springs occur. The Unica spring emerges approximately one kilometre west of Malenščica spring out of the Planinska Jama, a big, conduit-shaped cave at an elevation of 454 m asl. The discharge of the Unica spring at the entrance of Planinska Jama ranges from only a few hundred l/s until up to 100 m^3/s. All springs combined have a mean discharge of 21 m^3/s with a range from 1.1 m^3/s to over 100 m^3/s (Gabrovšek et al., 2010; Blatnik et al., 2017; Ravbar et al., 2012; Kaufman et al., 2020).

A moderate continental climate, also called premontane, prevails in the catchment area (Kovačič et al., 2020; Perko et al., 2020). Currently, Abieti-Fagetum dinaricum forests account for the largest proportion of land-use in the catchment area. The proportions of urban structures like settlements or industries as well as agriculturally used areas in the catchment are rather low and can mostly be found in the Pivka basin or at the bottom of the karst poljes (Kovačič et al., 2020; Ravbar et al., 2012). The distribution of the different land-use types is shown in Figure 3. In the Javorniki karst plateau at Poček the main military training area of Slovenia is located. Tracer tests were able to show that water recharged in the military training area contributes a significant proportion to the water discharging at Malenščica spring, indicating a potential risk for the spring water quality by polluting activities in the military area (Kogovšek et al., 1999).

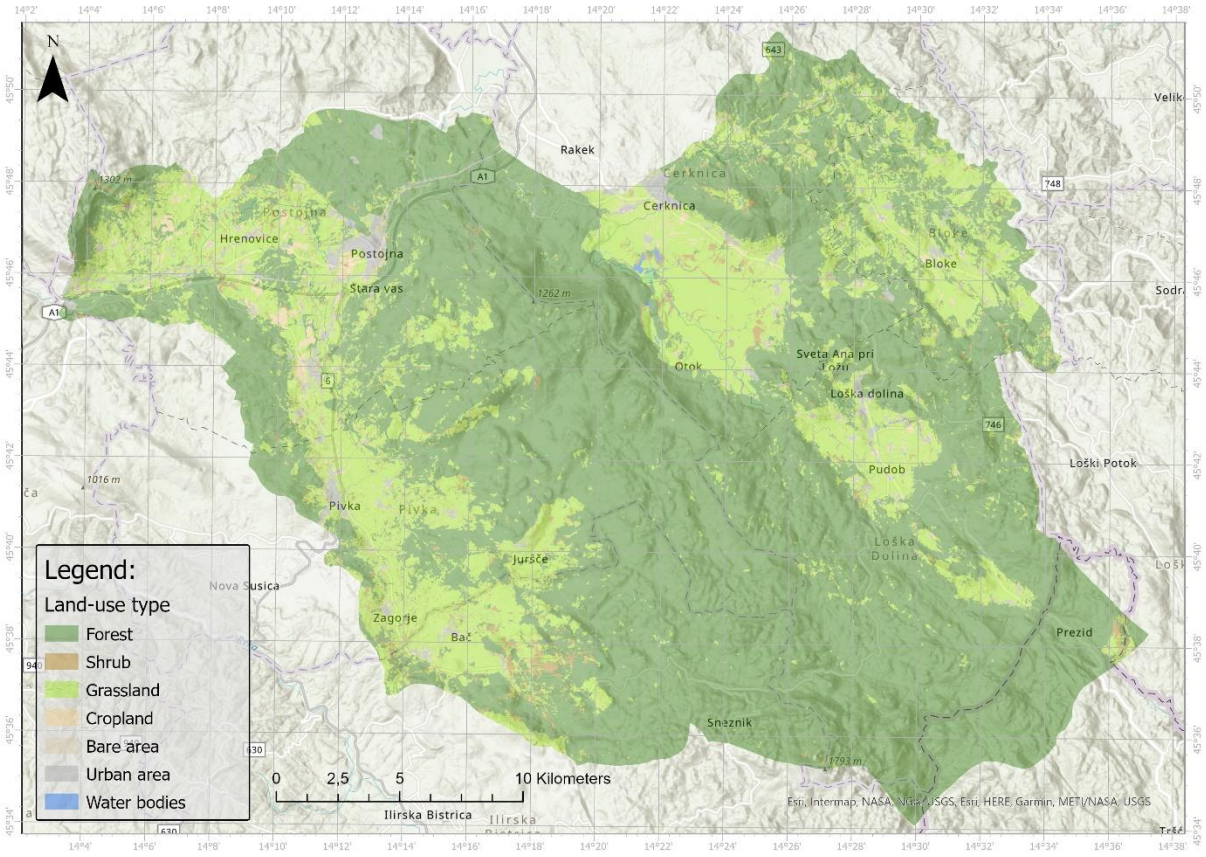

Figure 3: Land-use types in the catchment of the Unica Springs

2.2 Available data

A long time-series of discharge data as well as meteorological data are available for the study area. The discharge data used in this thesis are from the Hasberg gauging station (ARSO, 2021b). The station measures the discharge of the Unica River at an elevation of 445 m asl, approximately 1 km downstream of the Unica Springs. The location of the Hasberg gauging station is shown in Figure 6. The discharge time-series from 1992 until 2018 is used. Figure 4 shows the calculated mean monthly discharge for the used time-series.

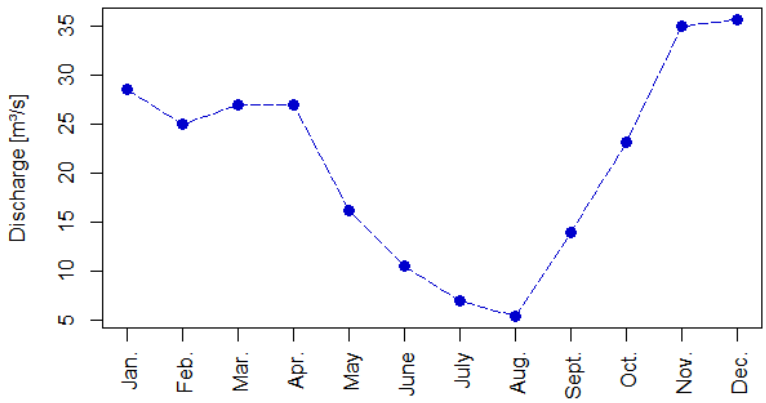

Figure 4: Average monthly discharge at Hasberg gauging station (1992-2018) based on data from ARSO (2021b)

For very low discharges as well as for very high discharges, the accuracy of discharge measurements from Hasberg gauging station is considered to be not ideal as it is located in the middle of Planinsko

Polje. Therefore, discharges higher than approximately 80 m³/s cannot be measured at the station as the Unica River then overflows its bank.

Meteorological data used are obtained from ARSO METEO (ARSO, 2021a). The closest meteorological station is situated in Postojna at an elevation of 533 m asl. Its location within the catchment area is shown in Figure 6. From the used meteorological data from 1992 until 2018 the mean annual precipitation recorded at the Postojna meteorological station is of 1490 mm/year while the mean annual temperature is of 9.8 °C. Figure 5 shows the mean monthly precipitation as well as mean monthly temperature calculated from the used time series of the Postojna meteorological station. The figure shows that mean precipitation is the highest in November and is generally high in autumn. Precipitation is the lowest in January, followed by July and August. The mean monthly temperature shows a typical annual oscillation with mean temperatures of approximately 20 °C in summer and approximately 0 °C in winter.

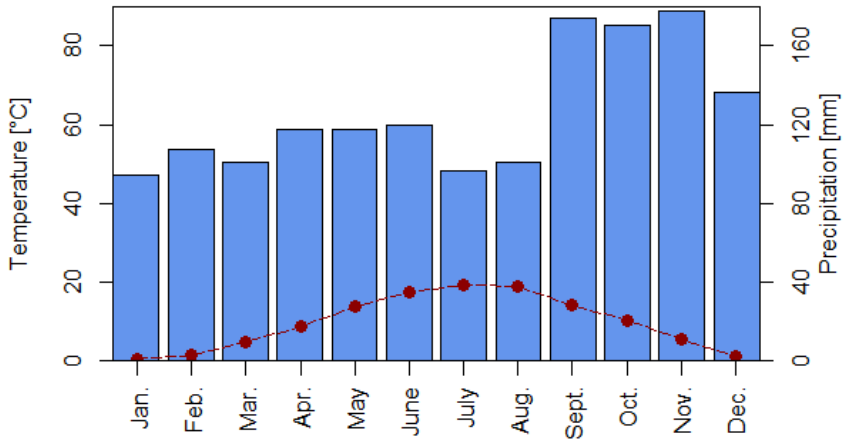

Figure 5: Average monthly precipitation (blue) and temperature (red) registered at the Postojna meteorological station during the 1992-2018 period based on data from ARSO (2021a)

In addition to meteorological data and discharge data, the approach of this study is based on the result of several tracer tests that were conducted in the catchment area. These will further be described in the next chapter. The locations of the injection points of the tracer tests are shown in Figure 6.

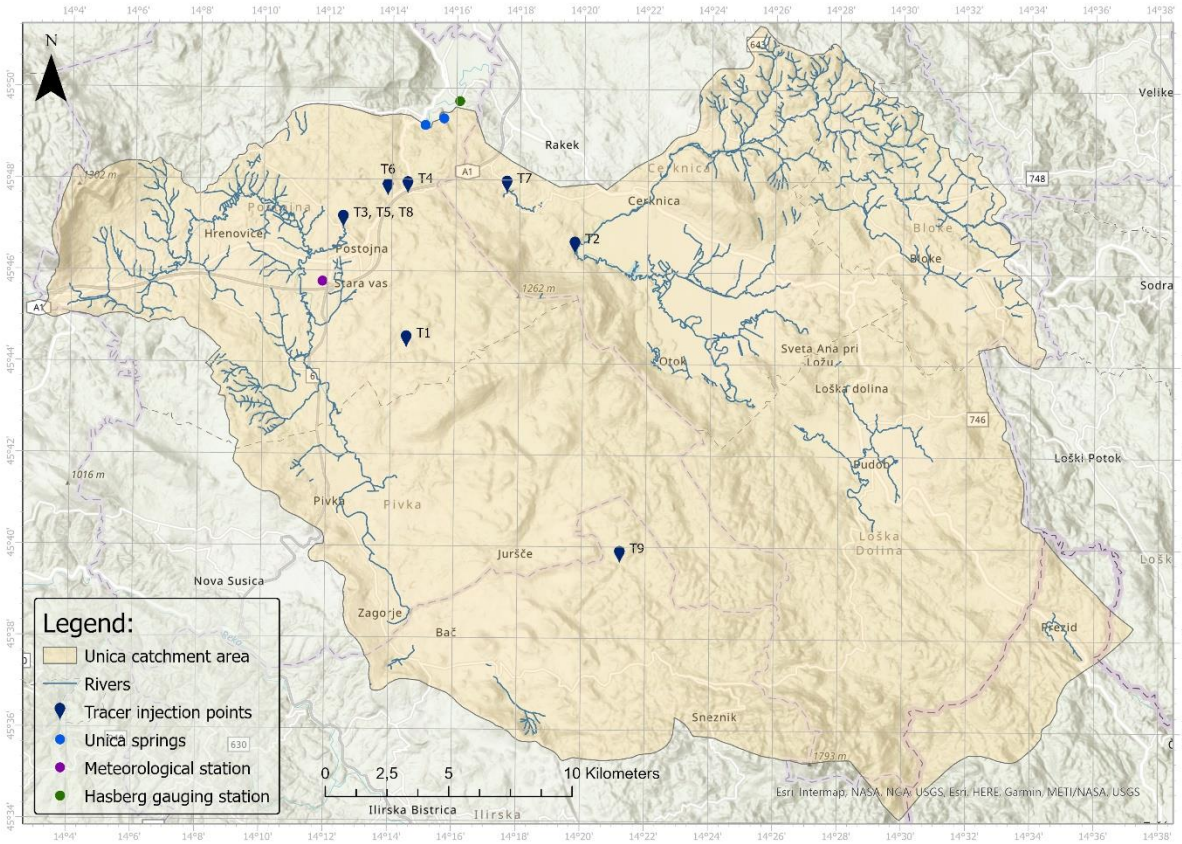

Figure 6: Locations of tracer injection points in the catchment of the Unica Springs

2.3 Tracer tests

Nine tracer tests were conducted in the study area between 1997 and 2014, where artificial tracer dyes were injected at different points located in the catchment. The tracer tests differ in their specific site and flow characteristics like their injection mode, the distance or gradient from injection point to the Unica Springs or in the respective hydrological conditions before or after tracer injection. As the preferential flow paths through the catchment of the Unica Springs are partly known through some explored cave passages an estimation of the real distance from tracer injection points to the Unica Springs was made in addition to the linear distance.

Some of the tracer tests were conducted as single tracer experiments and some as multi-tracer experiments where several tracer injections with different dyes were conducted at the same time. The individual tracer tests will further be described in more detail and a summary of their main characteristics can be found in Table 1. The necessary data are published in Kogovšek et al. (1999) for the first tracer test T1, in Gabrovšek et al. (2010) for tracer tests T2, T3, T4 and T5, in Ravbar et al. (2012) for T6, T7 and T8 and in Petrič et al. (2018) for T9.

Table 1: Overview of the tracer tests implemented in the catchment of the Unica Springs (Kogovšek et al., 1999; Gabrovšek et al., 2010; Ravbar et al., 2012; Petrič et al., 2018)

Tracer test	**T1**	**T2**	**T3**	**T4**	**T5**	**T6**	**T7**	**T8**	**T9**
Injection date	10.06.1997	20.05.2008		18.11.2008		02.06.2009			03.12.2014
Injection point	Poček military training area Doline	Mala Karlovica Ponor	Pivka River Ponor	Ravbar-komanda Oil collector	Pivka River Ponor	Avtodpad Karren	Rak River Ponor	Pivka River Ponor	Blatna Dolina Shaft
Linear distance x [m] injection point - Unica Springs	9,300	7,800	5,600	3,200	5,600	3,600	4,200	5,600	19,500
Estimation of the actual distance $guessAD$ [m] injection point - Unica Springs	13,000	13,600	11,300	4,300	11,300	4,300	7,000	11,300	25,000
Elevation of the injection point [m asl]	583	549	512	598	512	582	502	512	1014
Gradient [-] injection point - Hasberg gauging station	0.015	0.013	0.012	0.048	0.012	0.038	0.014	0.012	0.029
Injected tracer type	Uranine	Uranine	Am. G	Uranine	Am. G	Uranine	Am. G	Naphtionate	Uranine
Injected tracer mass [kg]	4	2.85	2.82	1	1	0.5	0.5	2	38
Hydrological conditions	Low-flow	Medium-flow		High/medium flow Recession			Low-flow		High-flow
Mean discharge during the tracer experiment Q_{mean_cal} [m³/s]	6.76	15.47	17.35	26.48	13.82	3.63	2.9	3.7	44.57
Discharge recorded during the tracer injection Q_{inj} [m³/s]	4.08	15.5	15.5	19.16	19.16	4.32	4.32	4.32	88.75
Peak discharge assigned to the tracer breakthrough curve Q_{peak} [m³/s]	30.59	21.61	21.61	19.16	19.16	12.81	4.29	12.81	88.98

For the first tracer test (T1) injection took place at the Poček military training area, in the middle of the Javorniki mountain, on the 10th of June 1997 (Kogovšek et al., 1999). A solution of 4 kg of Uranine was diluted in 11 m³ of water and injected "almost directly on the rock bottom of a small active doline" (Kogovšek et al., 1999). Thereby, significant absorption of tracer into the soil was tried to be avoided. Petrič et al. (2018) estimate the thickness of the vadose zone at the injection point to be around 40 m. In the following time period, regular fluorescence samples were taken at the Malenščica spring and also at other sampling points. In total, 62% of the injected tracer mass were recovered at Malenščica spring. The hydrological conditions of the tracer experiment T1 can be described as low-water conditions with pre-injection precipitation that was considerably below the average precipitation for the period of February until May of 1997. After injection heavy rain fell one time in the middle of June and another time in the middle of July, with the second rainfall event significantly impacting the water and tracer transport in the karst aquifer. In the Javorniki area significant rainfall did not occur from August until October, only in November and December (Kogovšek et al., 1999; Petrič et al., 2018). The first tracer pulse at the Malenščica spring for T1 (Figure 7) was created by the heavy rain event in the middle of June, then followed by a second large tracer pulse created by heavier rainfall in the middle of July, where even more tracer reached the spring than during the first pulse. Remaining Uranine then only reached the spring in November and December when heavier rains set in again after a dry summer, leading to one more tracer pulse (Kogovšek et al., 1999).

Tracer tests T2 and T3 were executed as a multi-tracer experiment with two different fluorescent dyes that were injected directly into sinking rivers in the catchment. The injections took place on the 20th of May 2008 (Gabrovšek et al., 2010). For T2 a solution with Uranine was injected at Cerkniško Polje into the ponor cave of Mala Karlovica and for T3 a solution with Amidorhodamine G (Am. G) was injected into the Pivka River directly before the ponor that leads to the Postojna Cave System. For the experiment, field fluorimeters were used in underground rivers to detect the tracers and at the springs, where water samples were taken and analysed to determine tracer concentrations. Before the tracer experiment spring discharge was high from Mid-March until the end of April 2008, then the springs were in recession. For the time of the tracer experiment there was medium flow at the springs. However, the day before injection discharge increased again due to some more intensive rainfalls (Gabrovšek et al., 2010). On the day of tracer injection as well as the following day more precipitation was registered. This led to an acceleration of tracer transfer through the karst system. In both cases, the resulting tracer breakthrough curves are uniformly shaped and continuous curves with a clear single main peak. Almost complete tracer recoveries could be observed (Gabrovšek et al., 2010).

Tracer tests T4 and T5 were also conducted as a multi-tracer experiment with two injections on the 18th of November in 2008 (Gabrovšek et al., 2010). As tracer tests T2 and T3 were conducted earlier in the same year, Gabrovšek et al. (2010) mention that even though the recovery rates in May 2008 were very high, it is still possible that some residual tracer could appear at the springs. For T4 a solution with Uranine was injected into an oil collector and then washed off with about 11 m³ of water. The oil collector drains polluted water from the highway into the vadose zone. As it is located at the karst surface and drains through the vadose zone, this tracer test was meant to highlight the impact of autogenic recharge in the karst system in contrast to the tracer tests that were injected into sinking streams (e.g. the Pivka River), which represent allogenic recharge. For T5 a solution with Amidorhodamine G was injected at Postojnska Jama into the ponor of the Pivka River. In the first part of November 2008 before tracer injection spring discharges were high, but at tracer injection there was a constant recession of discharges. After tracer injection, on the 25th of November there was some less intensive precipitation. On the 30th of November as well as in the beginning of December there was very intensive rainfall. This strong precipitation event led to floods with very high spring discharges during all of December. Compared to the observed breakthrough curves of T2 and T3, the observed breakthrough curves of T4

and T5 are more irregular and elongated. The tracers arrive at the Unica Springs with an "expected delay" and show secondary peaks (Gabrovšek et al., 2010).

On the 2nd of June 2009 another multi-tracer experiment was conducted in the catchment area. The experiment was deliberately conducted at low water conditions and different tracers were injected at 3 locations in the catchment that should represent different recharge pathways (Ravbar et al., 2012). The injection point for T6 was selected to represent a slower recharge pathway as a solution with Uranine was injected on the karst surface into a karren. Therefore, before reaching the water table the tracer first had to pass through the several tens of meters thick vadose zone. The injection points of T7 and T8 on the other hand represent a much more direct groundwater connection as these tracers were injected into sinking streams in the catchment. For T7 a solution with Amidorhodamine G was injected into the Rak River ponor. For T8 a solution with Naphtionate was injected into the Pivka River ponor. At the time of the tracer experiments groundwater levels and spring discharges were very low and in general there was an "extraordinary low-water period" in spring and summer of 2009, which lasted for several months (Ravbar et al., 2012). The discharges of the sinking streams were only a few tens of l/s for the Pivka River and a few l/s for the Rak River. While there was a slight increase in spring discharges due to some gentle rainfall 4 days before tracer injection, the discharges at the Unica Springs did not reach average values. Discharges then decreased again and at the beginning of the recession the tracers were injected. Only on the 20th and 21st of June, 18 days after injection, there was more intensive precipitation to which the springs reacted quickly. There was another precipitation event from the 5th until the 8th of July, followed by an increase in spring discharge and another short and intense rainfall event on the 18th and 19th of July where spring discharges reacted. For T6 Uranine was detected at the Unica spring on the 9th of July. The following rainfall events lead to secondary peaks and prolonged smooth tailings in the tracer breakthrough curve. In total, over 50% of the injected tracer was recovered. For T7, Amidorhodoamine G was first only detected in small peaks at the Malenščica spring. Starting on the 23rd of June, a more continuous tracer breakthrough curve could be measured, which however still contains some individual sharp peaks. The tracer recovery for T7 is 80%. For T8, Naphtionate was first detected at the Unica spring on the 30th of June, reaching a maximum concentration on the 11th of July. The breakthrough curve displays multiple peaks and is uniformly shaped and continuous. After 3 months almost all tracer was recovered (Ravbar et al., 2012).

The last tracer test (T9) was conducted on the 3rd of December 2014 (Petrič et al., 2018). It is the tracer test where injection took place at the longest distance from the Unica Springs. With 38 kg of Uranine also the largest quantity of tracer was used in this experiment. The injection took place in the Javorniki area. The tracer was injected into the 27 m deep shaft Brezno 1 in the Blatna Dolina and then 8.5 m³ of water were used to wash it away. At the injection point the thickness of the vadose zone was estimated to be around 400 m. From September until November 2014 there was a lot of rainfall in the Javorniki area which later also led to flooding in the area of the karst poljes, the conditions then stabilised. After injection there was periodic precipitation in small quantities and spring discharges declined again. The tracer was first detected on the 4th of January 2015 in the Unica spring at the entrance of Planinska Jama and one day later in the Malenščica spring. On the 8th and 9th of January 2015 peak concentrations of the tracer breakthrough curves were reached. After 2 more weeks there was a second, slightly smaller peak in the breakthrough curves after some additional rain event. Even after 1.5 years the tracer recovery of the injected tracer at the Unica Springs was only 26.5 % (Petrič et al., 2018).

As the two springs Malenščica and Unica are analysed as one single spring in the following, the breakthrough curves of the individual springs are combined into one common breakthrough curve. These final tracer curves were already established by Scheller (2020) by weighting the concentrations measured at the two springs according to the respective spring discharge. They are shown in Figure 7 and in Figure 8.

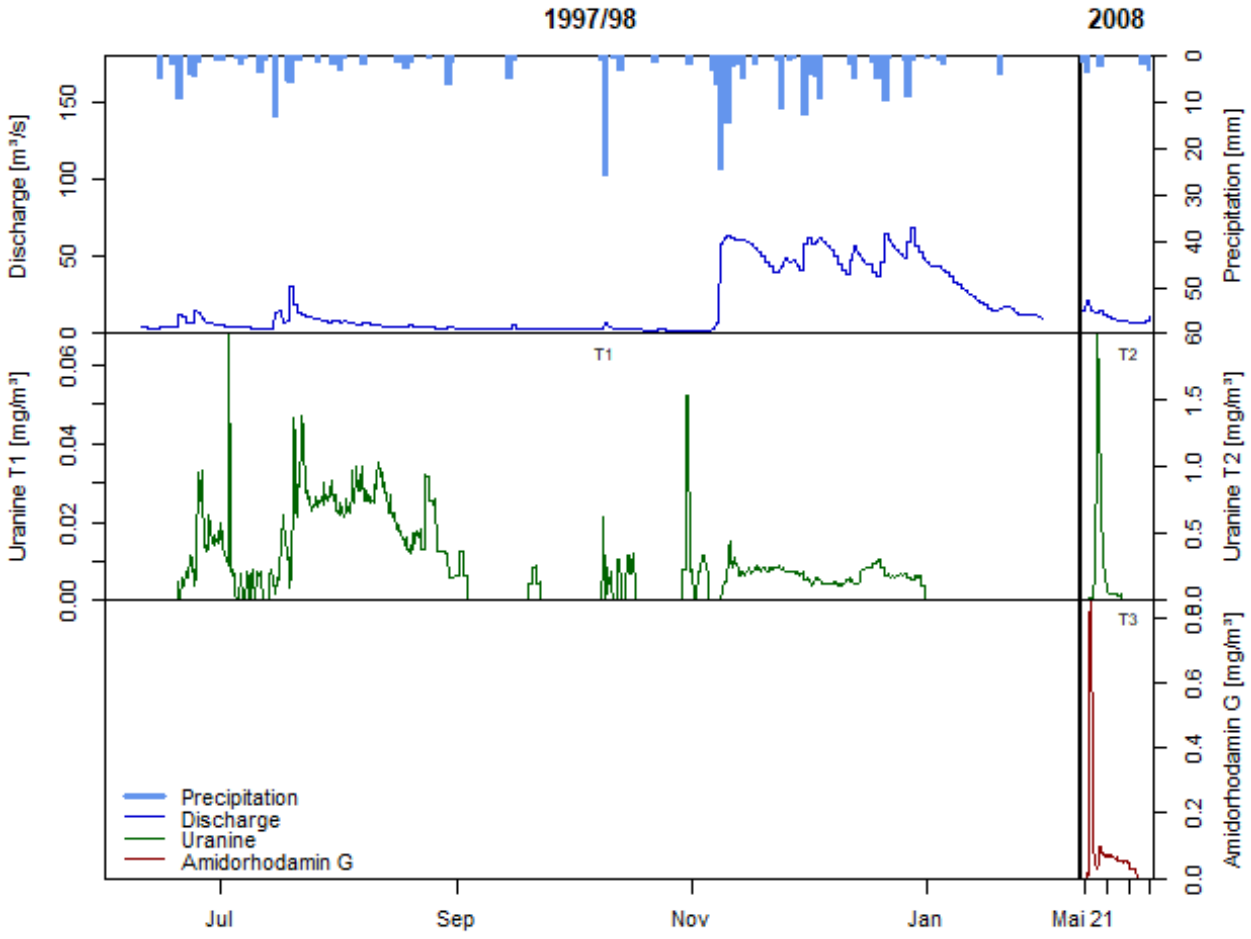

Figure 7: Observed tracer breakthrough curves of tracer tests 1,2 and 3 including discharge and precipitation time-series

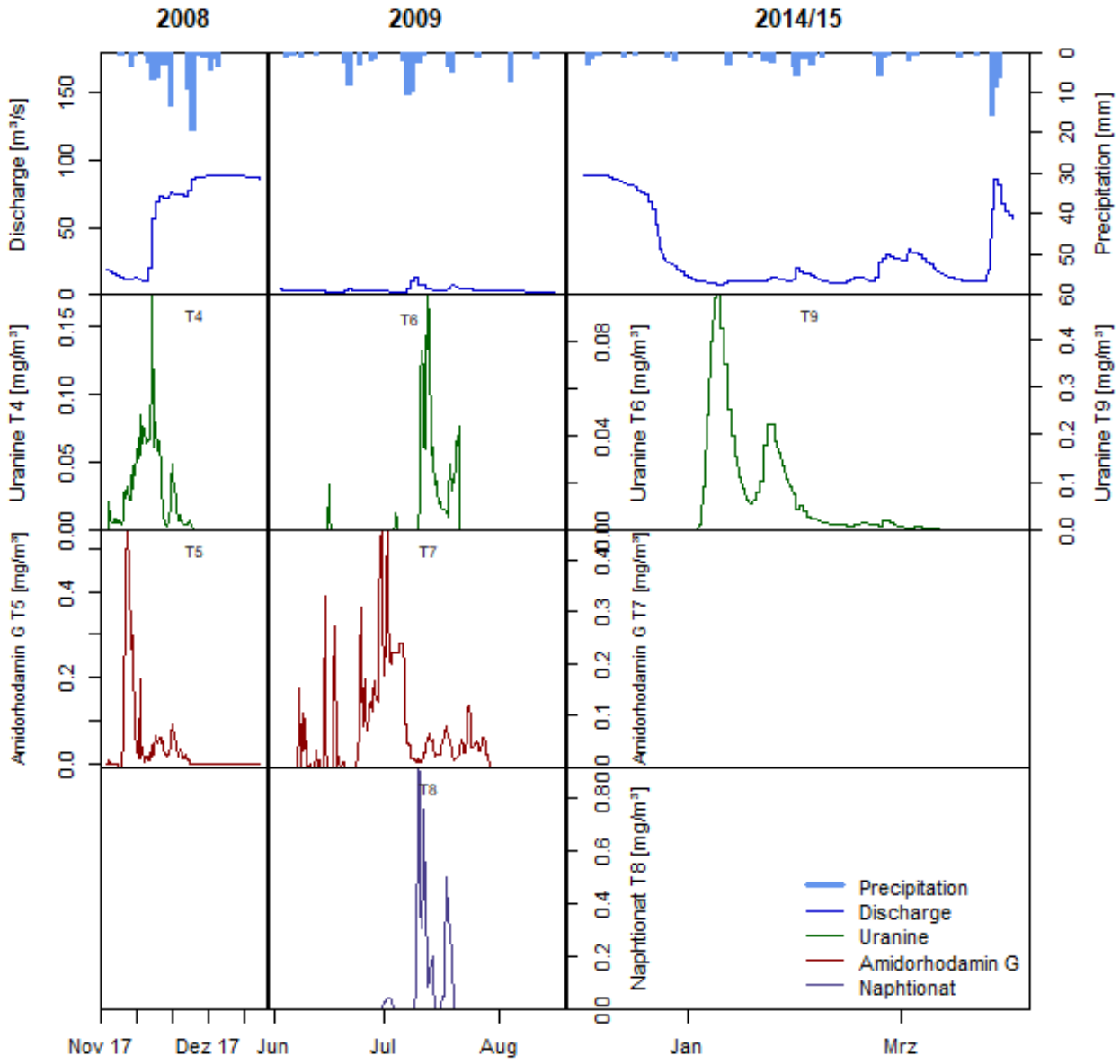

Figure 8: Observed tracer breakthrough curves of tracer tests 4 to 9 including discharge and precipitation time-series

3. Material and Methods

Figure 9 shows an overview of the entire methodology used to model the contamination risk of the Unica Springs under changing land-use and climate conditions. The approach can be subdivided into three individual parts. In the first part, different climate and land-use scenarios are defined for the region of catchment of the Unica Springs, which are the basis for later analysis. In the second part, a semi-distributed hydrological model, the VarKarst model (Hartmann et al., 2013), is used to model spring discharge. Some of the model parameters are fixed according to physical properties of the catchment area. Other model parameters are calibrated using a time-series of observed spring discharge. The climate and land-use scenarios and the calibrated VarKarst model are then jointly used to compute new discharge time-series that are based on the different scenarios. In the third part of the approach data of previously executed tracer tests are used to analyse tracer transport within the catchment area using a simple advection dispersion model. Then, transport characteristics are linked to specific flow and site characteristics for the different tracer tests. And in a last step the results of the tracer test analysis are combined with the discharge scenarios in order to evaluate the changes in contaminant transport under changing climate and land-use conditions in the catchment area. The VarKarst discharge model is executed in Matlab (versions R2020b and R2021a). All data pre- and post-processing, scenario preparations as well as the tracer modelling are performed in RStudio (version 1.1.383). Some additional geographical analysis are executed in ArcGIS. In the following chapter, the used methods will be described in more detail for every part of the modelling approach.

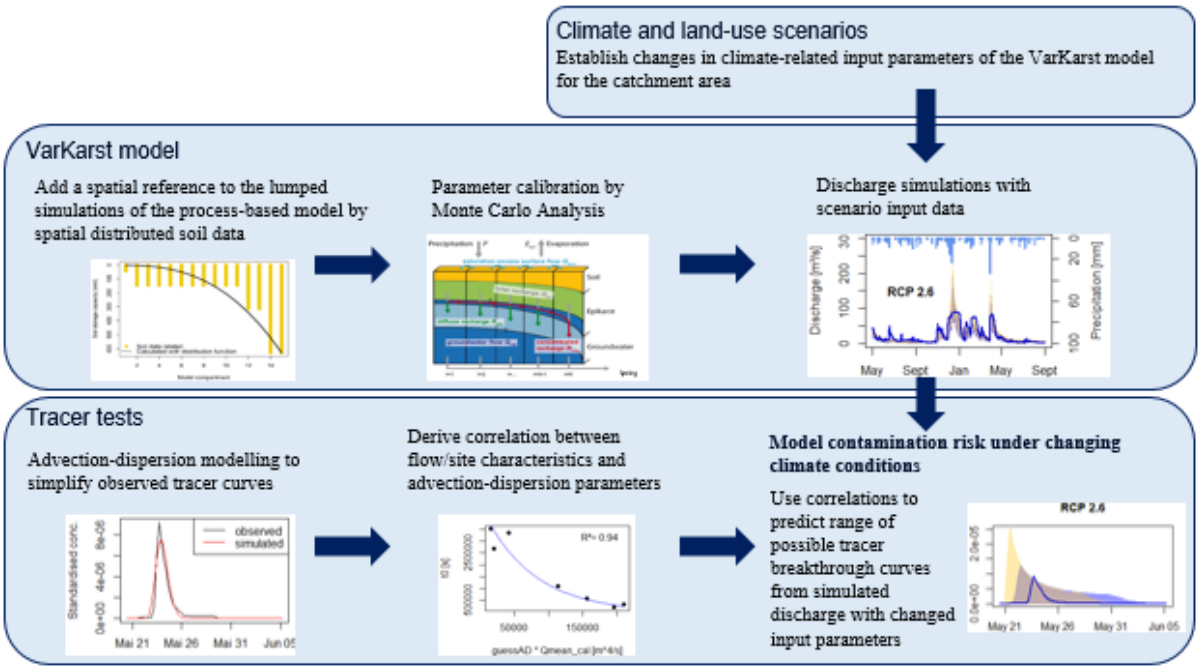

Figure 9: Flow chart of the general modelling approach

3.1 Climate and land-use scenarios

3.1.1 Climate scenarios

As previously mentioned, the extent of future climate change is unknown and depends on current and future greenhouse gas emissions. Therefore, in order to model the impacts of climate change, scenarios of the magnitude of climate change need to be defined. In this study, the RCPs 2.6 and 8.5 are chosen as a basis for climate modelling, representing one mild scenario of climate change and one more extreme scenario. The scenarios are based on climate simulations of the Slovenian Environment Agency (Bertalanič et al., 2018), which provide median changes and ranges of change in temperature and

precipitation for different regions of Slovenia, for 3 time periods and 3 RCP scenarios and for every meteorological season. The scenarios provide 30-year average deviations from the time period 1981-2010. Different regional climate models are considered in the scenarios and the model simulations are bias-corrected (Bertalanič et al., 2018). Figure 10 shows the projected changes in mean seasonal and annual air temperature for the modelling region which entails the Unica catchment. Figure 11 shows the projected changes in mean annual and seasonal precipitation for the region of the Unica catchment area.

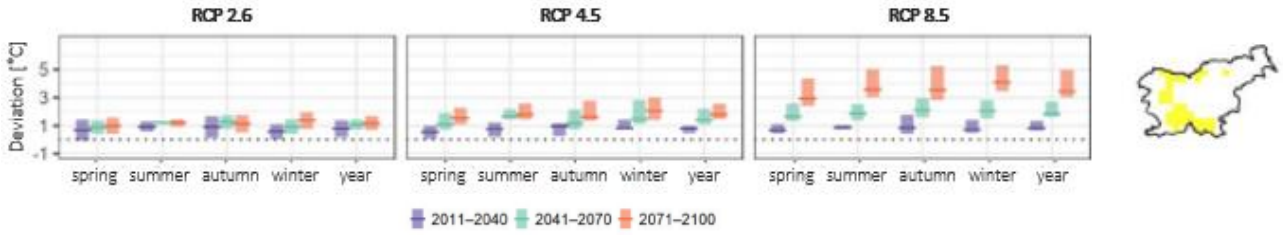

Figure 10: Climate projections of average changes in mean annual and seasonal air temperature for the region of the Unica catchment in Slovenia in different time-periods for emission scenarios RCP2.6, RCP4.5 and RCP8.5 (modified from Bertalanič et al. (2018))

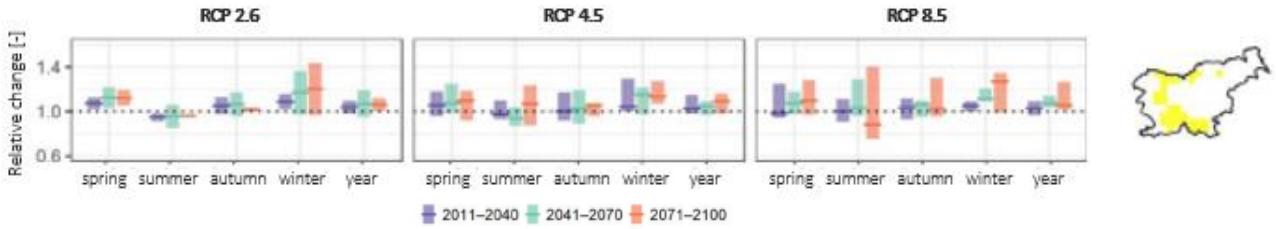

Figure 11: Climate projections of average changes in mean annual and seasonal precipitation the region of the Unica catchment in Slovenia in different time-periods for emission scenarios RCP2.6, RCP4.5 and RCP8.5 (modified from Bertalanič et al. (2018))

In this study, the two scenarios RCP2.6 and RCP8.5 are applied as climate scenarios based on their projected changes in the time period 2071-2100 compared to the reference period 1981-2010. Therefore, the observed input climate data of temperature and precipitation are modified according to the projected changes in temperature or precipitation. The projected changes are added to or subtracted from the input time series to create a manipulated time series, which represents the respective climate scenario. This is done considering the variation of changes between meteorological seasons. For the comparison of the two RCP scenarios, the median values of change are applied to the input time series. Table 2 shows the median and range of projected seasonal changes in mean air temperature for the region of the catchment area. In case of all climate scenarios temperature is increasing, with the most pronounced warming in winter and the least pronounced warming in spring. Median changes in mean air temperature are much higher in the RCP8.5 scenario compared to the RCP2.6. However, also the ranges of change are wider, which is connected to a greater uncertainty in climate simulations.

Table 2: Range and median of projected seasonal changes in mean air temperature in the region of the catchment for the different RCP scenarios in the time-period 2071-2100 compared to the reference period 1981-2010 [°C] (derived from Bertalanič et al. (2018))

	RCP2.6		**RCP4.5**		**RCP8.5**	
	Range [°C]	Median [°C]	Range [°C]	Median [°C]	Range [°C]	Median [°C]
Spring	0.4 – 1.6	1	1.1 – 2.2	1.5	2.4 – 4.3	2.9
Summer	1 – 1.4	1.2	1.5 – 2.6	1.8	3.0 – 5.0	3.6
Autumn	0.5 – 1.7	1.1	1.4 – 2.8	1.6	2.8 – 5.2	3.5
Winter	0.8 – 2.0	1.4	1.4 – 3.0	2.1	3.5 – 5.3	4.1

Table 3 shows the range and median of projected seasonal relative changes in mean precipitation. A value of 1 corresponds to no change in precipitation, whereas a value below 1 indicates a decline and a value above 1 an increase in precipitation. The projections for precipitation are not as clear as for temperature with wide ranges that mostly comprise values below and above 1.

Table 3: Range and median of projected seasonal changes in mean precipitation in the region of the catchment for the different RCP scenarios in the time-period 2071-2100 compared to the reference period 1981-2010 [-] (derived from Bertalanič et al. (2018))

	RCP2.6		**RCP4.5**		**RCP8.5**	
	Range [-]	Median [-]	Range [-]	Median [-]	Range [-]	Median [-]
Spring	1.06 – 1.19	1.13	0.92 – 1.18	1.1	0.98 – 1.28	1.1
Summer	0.97 – 0.95	0.96	0.88 – 1.23	1.07	0.76 – 1.40	0.89
Autumn	1.00 – 1.03	1.02	0.96 – 1.07	1.06	0.96 – 1.30	1.02
Winter	0.97 – 1.44	1.2	1.07 – 1.27	1.14	1.00 – 1.34	1.27

In addition to the two climate scenarios RCP2.6 and RCP8.5 a third climate scenario is analysed in order to address the uncertainty associated with the RCP scenarios. This climate uncertainty assessment is executed exemplary for the RCP8.5 scenario using a similar approach as Brenner et al. (2018). While the two RCP scenarios focus on the median of the projected changes for RCP2.6 and RCP8.5, the uncertainty scenario also considers the ranges of projected changes for RCP8.5. The upper and lower range as well as the median of the RCP8.5 projections for temperature and precipitation are combined in all possible ways. Therefore, 3x3 scenarios (3x temperature and 3x precipitation) with different compositions are produced. They are cumulatively defined as the RCP8.5 uncertainty scenario.

3.1.2 Land-use scenarios

Table 4 shows the current land-use composition according to land-use data provided by the Karst Research Institute SRC SAZU. Furthermore, the SRC SAZU provided data of historical land-use compositions. Exemplary, the land-use composition of the year 1957 is displayed in Table 4 provided by the SRC SAZU with a slight adaptation of land-use categories for better comparability. Historically, afforestation is the dominant land-use change in the Dinaric landscapes since the early nineteenth century (Perko et al., 2020). This is also reflected in the difference between current and historical land-use in Table 4, where the share of forests in the catchment area increased by 9.55%. Furthermore, an increase in urban area and a decrease of grassland and cropland from historical to current land-use can be observed. This historical land-use composition is used as one land-use scenario for model application.

For the definition of other land-use scenarios, the focus is on the development of forests and urban areas in the catchment area. The share of urban area has increased from historical to current land-use compositions and might also increase in the future due to population growth. In order to quantify the increase of urban area, the increase from historical to current data is extrapolated to the year 2100 assuming a linear relationship. As a result, the share of urban area in the catchment is assumed to increase from 2.44 % to 4.85 %. As mentioned before, the main land-use change in the Dinaric landscapes is afforestation. In analogy to the urban area, for the quantification of an afforestation scenario a linear interpolation to the year 2100 is executed based on the development from historical to current land-use. This leads to a forest share of approximately 82 % in the catchment area. On the other hand, a study by Kovačič et al. (2020) showed that due to large-scale forest disturbances in the catchment between 2014 and 2018, which could partly be caused by climate change, there was a decrease in growing stock of the forests in the catchment. For their calculations of effective precipitation, they therefore decreased the share of forests by 12.9 %. Therefore, in one deforestation scenario, the forest in the catchment is decreased from 69.75 % to approximately 57 %. To combine the development of urban area and forests, one scenario is based on a decrease in forest area and an increase in urban area (Deforestation & Urbanisation) and one scenario is based on an increase in forest area and an increase in urban area (Afforestation & Urbanisation). In order to compensate an increasing share of forest or urban area, the share of grassland is reduced.

Table 4: Land-use composition in the catchment area of the Unica Springs currently and with different scenarios

Land use type [%]	Current	Deforestation & Urbanisation	Afforestation & Urbanisation	Historical (1957)
Forest	69.75	57.00	82.00	60.20
Shrub	2.75	2.75	2.75	2.70
Grassland	23.36	33.70	8.70	28.80
Cropland	1.48	1.48	1.48	7.10
Liches and mosses	0.00	0.00	0.00	0.00
Bare area	0.02	0.02	0.02	0.00
Urban area	2.44	4.85	4.85	1.10
Snow and glaciers	0.00	0.00	0.00	0.00
Water bodies	0.20	0.20	0.20	0.10

3.1.3 Combined scenarios

In addition to the climate and land-use scenarios described so far, 3 combined scenarios are created in order to also analyse the combined effects of climate and land-use change on discharge and contaminant transport. An overview over all model scenarios is shown in Table 5.

Table 5: Climate and land-use scenarios

Climate	**RCP2.6** Median seasonal changes in temperature and precipitation projected for the period 2071-2100 (Bertalanič et al., 2018)	**RCP8.5** Median seasonal changes in temperature and precipitation projected for the period 2071-2100 (Bertalanič et al., 2018)	**Climate uncertainty consideration** Median and ranges of seasonal changes in temperature and precipitation projected for the period 2071-2100 (Bertalanič et al., 2018)
Land-use	**Deforestation & Urbanisation** Deforestation: Large-scale forest disturbances (Kovačič et al., 2020) Urbanisation: Extrapolation of historical changes in land-use until 2100	**Afforestation & Urbanisation** Afforestation: Extrapolation of historical changes in land-use until 2100 Urbanisation: Extrapolation of historical changes in land-use until 2100	**Historical land-use** Historical land-use composition of 1957: Deforestation & less Urbanisation
Combined	**RCP2.6 & Deforestation/Urbanisation**	**RCP 2.6 & Afforestation/Urbanisation**	**RCP8.5 & Afforestation/Urbanisation**

3.2 Discharge modelling

The basis for discharge modelling in the catchment of the Unica Springs is the observed discharge time-series of the Unica River at Hasberg gauging station, which records discharge of the Unica River downstream of the confluence of both main springs. Therefore, the Unica Springs are not distinguished but they are modelled collectively as one main spring.

3.2.1 Consideration of land-use types

In order to being able to model the impact of changes in land-use on spring discharge, the potential evapotranspiration, which is used as an input to the discharge model, is calculated similar to (Sarrazin et al., 2018). The calculation is based on the Penman Monteith method (Monteith, 1965; Penman, 1948), as this potential evapotranspiration equation can separately consider the impacts of climate or land-use changes. The Penman-Monteith method is recommended by the FAO (1998) for the calculation of potential evapotranspiration in scientific studies. Sarrazin et al. (2018) calculate the potential evapotranspiration depending on land-use as the sum of three main components: the potential transpiration rate over the vegetated fraction of the area $T_{\mathrm{pot}}(\mathrm{t})$, the evaporation from interception over the vegetated fraction of the area $Ec_{\mathrm{pot}}(\mathrm{t})$ and the potential bare soil evaporation rate over the bare soil fraction of the area $Es_{\mathrm{pot}}(\mathrm{t})$. The components can be calculated according to equations (2)-(4) (Sarrazin et al., 2018).

$$T_{\mathrm{pot}}(\mathrm{t}) = \frac{\Delta(\mathrm{t})\big(R_n(\mathrm{t}) - G(t)\big) + K_t \rho_a(t) c_p \frac{e_s(\mathrm{t}) - e_a(\mathrm{t})}{r_{a,can}(t)}}{\lambda(\mathrm{t})\left(\Delta(\mathrm{t}) + \gamma(t)\left(1 + \frac{r_{s,can}(t)}{r_{a,can}(t)}\right)\right)} \tag{2}$$

$$Ec_{\mathrm{pot}}(\mathrm{t}) = \frac{\Delta(\mathrm{t})\big(R_n(\mathrm{t}) - G(t)\big) + K_t \rho_a(t) c_p \frac{e_s(\mathrm{t}) - e_a(\mathrm{t})}{r_{a,can}(t)}}{\lambda(\mathrm{t})\big(\Delta(\mathrm{t}) + \gamma(t)\big)} \tag{3}$$

$$Es_{\mathrm{pot}}(\mathrm{t}) = \frac{\Delta(\mathrm{t})\big(R_n(\mathrm{t}) - G(t)\big) + K_t \rho_a(t) c_p \frac{e_s(\mathrm{t}) - e_a(\mathrm{t})}{r_{a,soil}(t)}}{\lambda(\mathrm{t})\left(\Delta(\mathrm{t}) + \gamma(t)\left(1 + \frac{r_{s,soil}(t)}{r_{a,soil}(t)}\right)\right)} \tag{4}$$

With

T_{pot}	Potential transpiration rate over the vegetated fraction of the area [mm day^{-1}]
Ec_{pot}	Potential evaporation from interception over the vegetated fraction of the area [mm day^{-1}]
Es_{pot}	Potential bare soil evaporation rate over the bare soil fraction of the area [mm day^{-1}]
R_n	Net radiation at the crop surface [MJm^{-2} day^{-1}]
G	Soil heat flux density [MJm^{-2} day^{-1}]
K_t	Time conversion factor [86400 sday^{-1}]
ρ_a	Air density [kgm^{-3}]
c_p	Specific heat of the air [1.013x10^{-3} MJkg^{-1}°C^{-1}]
$r_{a,can}$	Canopy aerodynamic resistance [sm^{-1}]
$r_{s,can}$	Canopy surface resistance [sm^{-1}]
$r_{a,soil}$	Soil aerodynamic resistance [sm^{-1}]
$r_{s,soil}$	Soil surface resistance [sm^{-1}]
e_s	Saturation vapour pressure [kPa]
e_a	Actual vapour pressure [kPa]
$(e_s - e_a)$	Saturation vapour pressure deficit [kPa]
Δ	Slope vapour pressure curve [kPa °C^{-1}]
λ	Latent heat of the vaporisation of water [MJkg^{-1}]
γ	Psychrometric constant [kPa °C^{-1}]

For the calculation of the potential evapotranspiration components, many variables are necessary that are not directly measured at the Postojna meteorological station. Their estimation will further be described in more detail. All equations and descriptions are based on the guidelines provided by the FAO (1998) and the study of Sarrazin et al. (2018).

The aerodynamic resistance of the canopy $r_{a,can}$ and the aerodynamic resistance of the soil $r_{a,soil}$ depend on the land cover and the soil. Their basic calculation is shown in equation (5). For the calculation of the canopy aerodynamic resistance $r_{a,can}$ the necessary parameters can be estimated from the crop height as shown in equations (6)-(8). For the calculation of the soil aerodynamic resistance $r_{a,soil}$ the zero plant displacement height is set to zero. Like in the study of Sarrazin et al. (2018), the roughness length for momentum and for heat and vapour transfer are assumed to be equal for the soil aerodynamic resistance.

$$\mathrm{r}_a = \frac{\ln\left(\frac{z_m - d}{z_{0m}}\right)\ln\left(\frac{z_h - d}{z_{0h}}\right)}{\mathrm{k}^2 \mathrm{u}_z} \tag{5}$$

$$d = 2/3h \tag{6}$$

$$z_{0m} = 0.123h \quad (7)$$

$$z_{0h} = 0.1z_{0m} \quad (8)$$

With

r_a	Aerodynamic resistance [sm^{-1}]
z_m	Height of wind measurements [m]
z_h	Height of humidity measurements [m]
d	Zero plant displacement height [m]
z_{0m}	Roughness length governing momentum transfer [m]
z_{0h}	Roughness length governing transfer of heat and vapour [m]
k	Von Karman's constant, 0.41 [-]
u_z	Wind speed at height z [ms^{-1}]
h	Crop height [m]

The canopy surface resistance $r_{s,can}$ can be estimated according to equation (10) considering the stomatal resistance r_{st} and the leaf area index LAI over the vegetated fraction f_c of the area. These parameters can in tern be calculated according to equations (10)-(14). The equations show that the LAI, and therefore also the other parameters, vary according to the month of the year m (Sarrazin et al., 2018).

$$r_{s,can}(t) = \frac{r_{st}}{\left(\frac{LAI(t)}{f_c(t)}\right)} \quad (9)$$

$$f_c(t) = 1 - e^{-kLAI(t)} \quad (10)$$

$$LAI_m = \frac{LAI_{min}}{100} LAI_{max} \qquad when\ m = 1,2,12 \quad (11)$$

$$LAI_m = \frac{LAI_{min}}{100}\frac{LAI_{max}}{4}\ (6 - m) + \frac{LAI_{max}}{4}\ (m - 2) \quad when\ m = 3,4,5 \quad (12)$$

$$LAI_m = LAI_{max} \qquad when\ m = 6,7,8 \quad (13)$$

$$LAI_m = \frac{LAI_{min}}{100}\frac{LAI_{max}}{4}\ (m - 8) + \frac{LAI_{max}}{4}\ (12 - m) \quad when\ m = 9,10,11 \quad (14)$$

With

r_{st}	Stomatal resistance [sm^{-1}]
f_c	Vegetated fraction of the area [-]
k	Extinction coefficient [-]
LAI	Leaf area index [-]
LAI_m	Leaf area index during month m [-]
LAI_{min}	Percentage reduction in the LAI during dormant season [%]
LAI_{max}	Annual maximum value of the LAI during growing season [-]

The daily saturation vapour pressure e_s can be calculated according to equation (15), considering the saturation vapour pressure (equation (16)) of the daily minimum and maximum temperature. The actual vapour pressure e_a is calculated according to equation (17), also considering the daily minimum and

maximum relative humidity. Equation (18) shows the calculation of the slope vapour pressure curve Δ. Time-series of daily maximum and minimum temperature as well as of relative humidity are available at the Postojna meteorological station and are derived from ARSO METEO (ARSO, 2021a). The location of the meteorological station is shown in Figure 6.

$$e_s = \frac{e^0_{(T_{\max})} + e^0_{(T_{\min})}}{2} \tag{15}$$

$$e^0_{(T)} = 0.6108 * \exp\left(\frac{17.27T}{T + 237.3}\right) \tag{16}$$

$$e_a = \frac{e^0_{(T_{min})} \frac{RH_{max}}{100} + e^0_{(T_{max})} \frac{RH_{min}}{100}}{2} \tag{17}$$

$$\Delta = \frac{4098\left[0.6108 * \exp\left(\frac{17.27T}{T + 237.3}\right)\right]}{(T + 273.3)^2} \tag{18}$$

With

$e^0_{(T_{min})}$	Saturation vapour pressure at daily minimum temperature [kPa]
$e^0_{(T_{max})}$	Saturation vapour pressure at daily maximum temperature [kPa]
$e^0_{(T)}$	Saturation vapour pressure at the air temperature T [kPa]
T	Air temperature [°C]
RH_{max}	Maximum relative humidity [%]
RH_{min}	Minimum relative humidity [%]

The psychrometric constant γ can be estimated from the atmospheric pressure P at the location (equation (19)), which can in turn be estimated from the elevation of the site above sea level z (equation (20)). The mean elevation of the catchment area is derived from a digital elevation model of the catchment.

$$\gamma \approx 0.665 * 10^{-3} P \tag{19}$$

$$P = 101.3\left(\frac{293 - 0.0065z}{293}\right)^{5.26} \tag{20}$$

With

P	Atmospheric pressure [kPa]
z	Elevation above sea level [m]

Radiation data is not available for a sufficiently long time period for the Postojna meteorological station, therefore it also has to be approximated. Net radiation is composed of incoming shortwave radiation and outgoing longwave radiation (equation (21)). These radiations can in turn be calculated according to equation (22) and equation (23), considering previously defined variables as well as the Stefan-Boltzmann constant σ, the albedo α of the reference crop and the solar radiation R_s and the clear-sky radiation R_{so}.

$$R_n = R_{ns} - R_{nl} \tag{21}$$

$$R_{nl} = \sigma \left[\frac{T_{max,K} + T_{min,K}}{2}\right] \left(0.34 - 0.14\sqrt{e_a}\right) \left(1.35\frac{R_s}{R_{so}} - 0.35\right) \tag{22}$$

$$R_{ns} = (1 - \alpha)R_s \tag{23}$$

With

R_n	Net radiation [MJm^{-2}day^{-1}]
R_{ns}	Incoming net shortwave/solar radiation [MJm^{-2}day^{-1}]
R_{nl}	Outgoing net longwave radiation [MJm^{-2}day^{-1}]
σ	Stefan-Boltzmann constant [4.903*10^{-9} MJK^{-4}m^{-2}day^{-1}]
$T_{max,K}$	Maximum absolute temperature during the 24h-period [K]
$T_{min,K}$	Minimum absolute temperature during the 24h-period [K]
e_a	Actual vapour pressure [kPa]
R_s/R_{so}	Relative shortwave radiation [-]
R_s	Solar radiation [MJm^{-2}day^{-1}]
R_{so}	Clear-sky radiation [MJm^{-2}day^{-1}]
α	Albedo [-]

The solar radiation R_s and the clear-sky radiation R_{so} can be estimated according to equation (26) and equation (24). The Angstrom parameters $(a_s + b_s)$ describe the fraction of extra-terrestrial radiation reaching the earth on clear-sky days. These parameters can be calibrated for meteorological stations. They are not available for the Postojna meteorological station. However, the FAO (1998) also provides alternative estimations. For the calculation of clear-sky radiation R_{so} with no available parameters a_s or b_s, equation (25) can be used instead. For the calculation of solar radiation R_s without calibrated Angstrom parameters, the FAO (1998) recommends the values $a_s = 0.25$ and $b_s = 0.5$. Therefore, these values are used in the calculation. In both calculations, the extra-terrestrial radiation R_a is used. Extra-terrestrial radiation R_a can be calculated according to equation (28). For the calculation of the solar radiation R_s, the observed actual duration of sunshine hours n and the maximum possible duration of sunshine hours N are compared. Data for daily actual duration of sunshine hours n are available for the Postojna meteorological station and the daily maximum possible duration of sunshine N can be estimated based on the sunset hour angle ω_s with equation (27).

$$R_{so} = (a_s + b_s)R_a \tag{24}$$

$$R_{so} = (0.75 + 2 * 10^{-5}z)R_a \tag{25}$$

$$R_s = \left(a_s + b_s\frac{n}{N}\right)R_a \tag{26}$$

$$N = \frac{24}{\pi}\omega_s \tag{27}$$

$$R_a = \frac{24(60)}{\pi} G_{so} d_r [\omega_s \sin(\varphi) \sin(\delta) + \cos(\varphi) \cos(\delta) \sin(\omega_s)] \quad (28)$$

With

$(a_s + b_s)$	Fraction of extra-terrestrial radiation reaching the earth on clear-sky days (n=N)
z	Station elevation above sea level [m]
n	Actual duration of sunshine [h]
N	Maximum possible duration of sunshine [h]
R_a	Extra-terrestrial radiation [MJm^{-2}day^{-1}]
ω_s	Sunset hour angle [rad]
G_{so}	Solar constant [0.0820 MJm^{-2}day^{-1}]
d_r	Inverse relative distance Earth-Sun
φ	Latitude [rad]
δ	Solar decimation [rad]

The sunset hour angle ω_s can be calculated using equation (29). The inverse relative distance from Earth to the Sun d_r and the solar decimation δ, which are used in the calculation of extra-terrestrial radiation are derived from equations (30) and (31), based on the number of the day in the year J. The latitude φ of the centre of the catchment area is approximately 45.7 °N.

Furthermore, for the calculation of reference evapotranspiration in daily time-steps, the ground heat flux G can be neglected according to the FAO (1998).

$$\omega_S = \arccos[-tan(\varphi)\, tan(\delta)] \quad (29)$$

$$d_r = 1 + 0.033 \cos\left(\frac{2\pi}{365} J\right) \quad (30)$$

$$\delta = 0.409 \sin\left(\frac{2\pi}{365} J - 1.39\right) \quad (31)$$

$$G_{day} \approx 0 \quad (32)$$

With

J	Number of the day in the year [-]

In this way, potential evapotranspiration is estimated based on daily data of minimum and maximum temperature and humidity, daily data of sunshine duration and wind speed and the mean elevation and latitude of the catchment area. Missing values in the time-series used for this calculations are filled in using linear interpolation.

For the calculation of potential evapotranspiration of different land-uses, the meteorological parameters in the calculations are the same for every land-use type. However, several parameters change between the different land-use types and need to be parametrised depending on the land-use. The parameters that vary with land-use are: the vegetation height, the stomatal resistance, the soil roughness length, the annual maximum leaf area index during growing season, the reduction in leaf area index in the dormant season compared to the growing season, the vegetation albedo and the soil albedo. They are parametrised according to Niu et al. (2011) and Yang et al. (2011).

For the creation of the evapotranspiration input data to the discharge model, the potential evapotranspiration for every single occurring land-use type in the catchment is calculated. The evapotranspiration time-series calculated for the different land-use types are then combined to one input evapotranspiration time-series weighted according to their percental occurrence in the catchment area.

When climate or land-use scenarios are applied, either the input temperature time-series for evapotranspiration calculation changes or the land-use composition and therefore the weights of the respective evapotranspiration time-series change or a combination of both. This leads to a changed evapotranspiration input to the discharge model.

3.2.2 VarKarst model

Due to the location of the Unica catchment in the Dinaric karst area and the strong karst characteristics within the catchment area leading to a large heterogeneity also in discharge and flow characteristics, the VarKarst model is used for discharge modelling. This semi-distributed, process-based model was first introduced by Hartmann et al. (2013) and is specifically developed to model karst systems with their special characteristics. It namely uses distribution functions in order to consider the spatial variability of karst system properties, like the soil and epikarst depths, the ratios of concentrated and diffuse groundwater recharge or the epikarst and groundwater hydrodynamics. Modelling this variability is achieved by a model setup with N model compartments. The soil, epikarst and groundwater systems are divided into these N compartments. The properties of the compartments vary according to Pareto functions, which need one distribution parameter (Hartmann et al., 2013). In this study, the number of model compartments N is 15. The model has already been successfully applied for different research purposes and at different karst regions (Hartmann et al., 2013; Hartmann et al., 2014b; Hartmann et al., 2016; Mudarra et al., 2019). Figure 12 shows a schema of the general model structure and in the following paragraph the model will be described in more detail. The mathematical description is based on Hartmann et al. (2013), Hartmann et al. (2014) as well as on Mudarra et al. (2019). The VarKarst model was modified by Scheller (2020) to operate in 6-hourly time-steps instead of daily time-steps in order to being able to also model narrow tracer breakthrough curves.

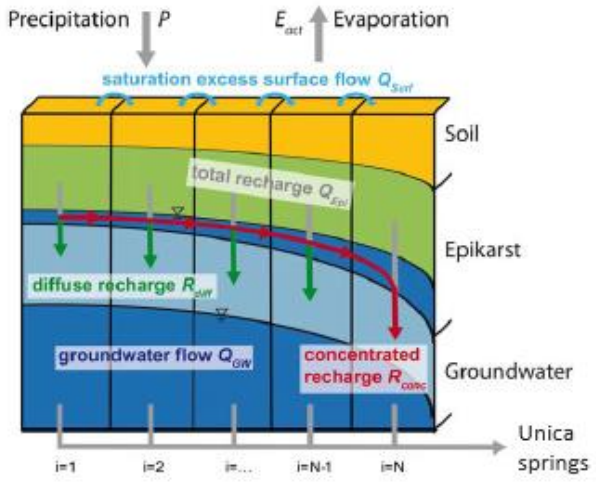

Figure 12: VarKarst general model structure (modified from Hartmann et al. (2014b))

The VarKarst model inputs are time-series of precipitation $P(t)$ and potential evapotranspiration data $E_{pot}(t)$. Starting at the top of the system, the variability of soil depths is modelled using the two parameters mean soil storage capacity V_S [mm] and the soil and epikarst distribution coefficient α_{SE} [-]. Based on those parameters, the soil storage capacity of every single compartment i $V_{S,i}$ [mm] of all N model compartments is calculated according to equation (33).

$$V_{S,i} = V_{max,S}\left(\frac{i}{N}\right)^{\alpha_{SE}} \tag{33}$$

$V_{max,S}$ [mm] in equation (33) describes the maximum soil storage capacity and is derived from the mean soil storage capacity V_s [mm] as described in equation (34), where $i_{1/2}$ describes the compartment where $V_{S,i}$ on the left equals $V_{S,i}$ on the right.

$$\int_0^{i_{1/2}} V_{max,S}\left(\frac{x}{N}\right)^{\alpha_{SE}} dx = \frac{\int_0^N V_{max,S}\left(\frac{x}{N}\right)^{\alpha_{SE}} dx}{2};\ V_S = V_{max,S}\left(\frac{i_{1/2}}{N}\right)^{\alpha_{SE}} \Leftrightarrow V_{max,S} = V_S * 2^{\left(\frac{\alpha_{SE}}{1+\alpha_{SE}}\right)} \tag{34}$$

In every soil compartment at every time-step, actual evapotranspiration is calculated from potential evapotranspiration $E_{pot}(t)$ [mm] as well as from the amount of water currently stored in the soil layer of the respective compartment $V_{soil,i}(t)$[mm], the excess water from compartment $i-1$ $Q_{surf,i}(t)$ [mm] (equation (40)) and the soil storage capacity $V_{s,i}$ [mm] of the compartment. Equation (35) displays the calculation.

$$E_{act,i}(t) = E_{pot}(t)\frac{min\left[V_{soil,i}(t) + P(t) + Q_{surf,i}(t), V_{S,i}\right]}{V_{S,i}} \tag{35}$$

From the soil layer of each compartment, recharge to the epikarst layer of the respective compartment $R_{epi,i}$ [mm] is generated according to equation (36).

$$R_{epi,i}(t) = max\left[V_{soil,i}(t) + P(t) + Q_{surf,i}(t) - E_{act,i}(t) - V_{S,i}, 0\right] \tag{36}$$

In the same way as for the soil layer, the variability of the epikarst storage is modelled using the distribution coefficient α_{SE} as shown in equation (37). Also the maximum epikarst storage capacity $V_{max,e}$ [mm] is derived from the mean epikarst storage capacity V_e [mm] in the same way as the maximum soil storage capacity is derived from the mean soil storage capacity in equation (34).

$$V_{e,i} = V_{max,e}\left(\frac{i}{N}\right)^{\alpha_{SE}} \tag{37}$$

The distribution coefficient α_{SE} is also used to describe the variability of the epikarst storage coefficient $K_{epi,i}$[d] throughout the model compartments as shown in equation (38).

$$K_{epi,i} = K_{max,epi} * \left(\frac{N-i+1}{N}\right)^{\alpha_{SE}} \tag{38}$$

The maximum epikarst storage coefficient $K_{max,epi}$ [d] in equation (38) can be calculated using the mean epikarst storage coefficient K_{epi}[d] and the distribution coefficient α_{SE} as shown in equation (39).

$$N * K_{epi} = \int_0^N K_{max,epi}\left(\frac{x}{N}\right)^{\alpha_{SE}} dx \Leftrightarrow K_{max,epi} = K_{epi} * (\alpha_{SE} + 1) \tag{39}$$

If the maximum soil and epikarst storage capacities are reached, lateral surface runoff is generated by the model, flowing towards the next model compartment $Q_{surf,i+1}$ [mm] (equation (40)).

$$Q_{surf,i+1}(t) = max\left[V_{epi,i}(t) + R_{Epi,i}(t) - V_{e,i}, 0\right] \tag{40}$$

The outflow from each epikarst compartment $Q_{epi,i}$ [mm] is computed according to equation (41), where $V_{epi,i}$ [mm] is the amount of water stored in the epikarst layer of each compartment.

$$Q_{epi,i} = \frac{min\left[V_{epi,i}(t) + R_{epi,i}(t), V_{e,i}\right]}{K_{epi,i}} \tag{41}$$

The outflow from each epikarst compartment is then separated into concentrated groundwater recharge $R_{conc,i}$ [mm] and diffuse groundwater recharge $R_{diff,i}$ [mm]. In this way, the model accounts for the heterogeneity of fast and diffuse recharge processes in karst systems. The separation is quantified for each compartment depending on a variable groundwater separation factor $f_{C,i}$ [-]. This separation factor is determined based the distribution coefficient α_{fsep} [-]. Equations (42) to (44) show how the concentrated and diffuse recharge as well as the groundwater separation factor are calculated for each compartment within the model.

$$R_{conc,i}(t) = f_{C,i} * Q_{epi,i}(t) \tag{42}$$

$$R_{diff,i}(t) = \left(1 - f_{C,i}\right) * Q_{epi,i}(t) \tag{43}$$

$$f_{C,i} = \left(\frac{i}{N}\right)^{\alpha_{fsep}} \tag{44}$$

Diffuse recharge then flows to the matrix system, which is represented in the model by the groundwater compartments $i = 1$ until $i = N - 1$. Concentrated recharge flows laterally to the conduit system, which is represented by the groundwater compartment $i = N$. Again, the groundwater storage coefficients $K_{GW,i}$ [d] vary across the compartments and are defined using a distribution coefficient α_{GW} [-] (equation(45)), where K_C [d] represents the conduit storage coefficient.

$$K_{GW,i} = K_C * \left(\frac{i}{N}\right)^{-\alpha_{GW}} \tag{45}$$

The discharge from the matrix system (groundwater compartments $i = 1$ until $i = N - 1$) $Q_{GW,i}$ [mm] is computed according to equation (46), with $V_{GW,i}$ [mm] being the amount of water stored in the groundwater layer of each compartment.

$$Q_{GW,i}(t) = \frac{V_{GW,i}(t) + R_{diff,i}(t)}{K_{GW,i}}; \qquad i = 1 \ldots N - 1 \tag{46}$$

From the conduit system, which is represented by the model compartment with $i = N$, discharge is generated according to equation (47).

$$Q_{GW,i}(t) = \frac{V_{GW,N}(t) + \sum_{i=1}^{N} R_{conc,i}\,(t)}{K_C}; \quad i = N \tag{47}$$

Finally, the discharge of the main spring Q_{main} [l/s] is composed of the discharges of all model compartment including matrix as well as conduit discharge. It is rescaled to [l/s] by the recharge area A [km²]. Equation (48) shows this final equation.

$$Q_{main}(t) = \frac{A}{N} * \sum_{i=1}^{N} Q_{GW,i}(t) \tag{48}$$

3.2.3 Parameter estimation and evaluation of prediction performance

In total, 8 model parameters are used in the VarKarst model. Table 6 lists all parameters and shows a brief description of each parameter. Three of the parameters are determined based on physical properties of the Unica catchment. Thus, over-parameterisation of the model, which can lead to equifinality of the model parameters, can be avoided. The recharge area A of the system is set to a fixed value of 820 km² according to researchers of the Karst Research Institute ZRC SAZU. The values for the soil and epikarst distribution coefficient α_{SE} as well as the mean soil storage capacity V_s were fixed by Scheller (2020) using spatial information on estimated soil depths in the catchment area, provided by the Karst Research Institute ZRC SAZU. Four different soil depths were distinguished and were assigned to the 15 model compartments depending on their percental occurrence within the catchment area, with the smallest soil depth being assigned to the first model compartment. Based on the soil depths and the mean effective porosity of the catchment, which was calculated according to the relative coverage of different soil types in the catchment, the soil storage capacity for each model compartment was set to a fixed value by Scheller (2020). Therefore, the parameter V_s could be omitted by setting a fixed value of soil storage capacity for every model compartment. The resulting fixed soil storage capacities of the model compartments are shown in Figure 13. The parameter α_{SE} was then determined by Scheller (2020) by fitting the distribution function to the soil storage capacities using the root mean square error, resulting in a α_{SE} of 2.756. The resulting distribution function is also displayed in Figure 13. This combination of spatially distributed information with the semi-distributed VarKarst model to create a linkage between spatial and temporal information was based on a successful study on providing spatiotemporal information by Hartmann et al. (2014).

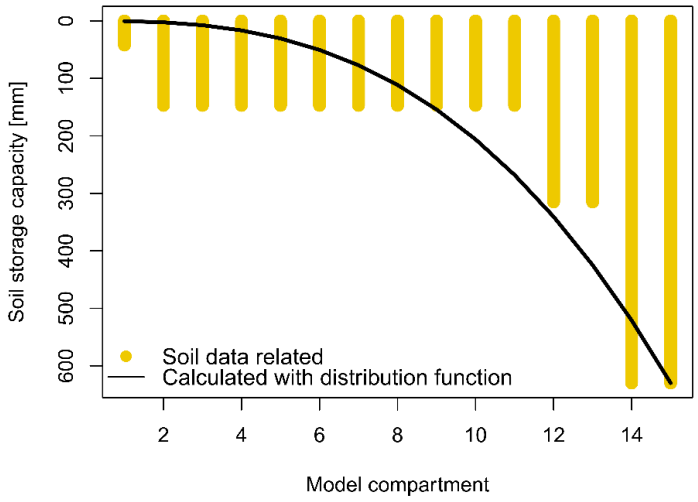

Figure 13: Soil storage capacity of the 15 model compartments with the fitted distribution function (Scheller, 2020)

The VarKarst parameters that are not set to fixed values according to physical properties of the catchment area are estimated by calibration. A split sample test is performed, where one portion of the available data is used for calibration and therefore for model development and one portion of data is used for validation to evaluate the model (Picard & Berk, 1990). With the time-series used in this study with observations from the years 1992 until 2018, the first 5 years of data are used as a warm-up period. In the warm-up period the modelled reservoirs can fill up and the model can reach a stable state in order to minimize the influence of starting values. The remaining time-series is separated into two parts for calibration and validation. Approximately two thirds of the data, from the year 1997 until 2010, are used for calibration and approximately one third of the data, from the year 2010 until 2018, is used for validation.

The calibration itself is performed by executing a Monte Carlo analysis with 250000 runs (Beven, 2008). In each run, the five calibration parameters are randomly picked from a uniform distribution between defined parameter ranges. The calibration ranges are adopted from Scheller (2020) and displayed in Table 6. For each run, the VarKarst model produces a discharge time-series based on the random parameterset of the respective run. The performance of the discharge simulation of each run is then quantified using the Kling-Gupta efficiency KGE as an objective function (equation (49)). The KGE compares the observed discharge values with the simulated discharge values of the VarKarst model for the calibration period. The KGE values can range from minus infinity until 1, where 1 represents the best fit.

$$KGE = 1 - \sqrt{(r-1)^2 + (\propto -1)^2 + (\beta - 1)^2} \quad (49)$$

$$with\ \alpha = \frac{\sigma_S}{\sigma_O}\ and\ \beta = \frac{\mu_S}{\mu_O}$$

The KGE is computed using the linear correlation coefficient between simulations and observations *r*, the variability α, which is the ratio between the standard deviation of the simulations σ_S and the standard deviation of the observations σ_O, and the bias β, which is the ratio between the mean of the simulations μ_S and the mean of the observations μ_O (Gupta et al., 2009).

The calibration is executed using the basic climate data as input data, without any scenario manipulations. The land-use for calibration is set to the current land use in the catchment area (Table 4). The parameter sets that yield the best objective functions for the calibration period are selected for simulation of the validation period and for later scenario analysis. Not one single parameter set is used for prediction, but several parameter sets are used collectively in order to also consider model uncertainty. The threshold value of the objective function to distinguish which runs are used for prediction is determined on the one hand by setting the threshold high enough so not too many parameter sets are used. On the other hand over-calibration is tried to be avoided by assuring that the gap between mean objective function of the validation period and mean objective function of the calibration period does not become disproportionately large. In this case, parameter sets with a KGE > 0.8 are used for prediction.

Table 6: VarKarst parameter descriptions and calibration ranges

Parameter	Unit	Description	Calibration range	
			Lower	Upper
α_{SE}	-	soil and epikarst distribution coefficient	-	
V_S	mm	mean soil storage capacity	-	
V_e	mm	mean epikarst storage capacity	0.1	300
K_{epi}	d	mean epikarst storage coefficient	0.1	50
α_{fsep}	-	recharge separation distribution coefficient	0.1	10
α_{GW}	-	groundwater distribution coefficient	0.1	10
K_C	d	conduit storage coefficient	1	30
A	km²	recharge area	-	

After calibration, the sensitivity of the calibrated VarKarst model parameters is analysed in order to evaluate the influence of the parameters on the *model output* and the model performance. This is done using the results of the Monte Carlo calibration. For a visual evaluation dotty plots are computed. For

each parameter they show the value of the parameter plotted against the respective model performance of each Monte Carlo run. A visible pattern in the distribution of high model performance value indicates a sensitive parameter. Furthermore, the sensitivity is analysed according to the approach of Hornberger, Spear & Young (Hornberger and Spear, 1981). The Monte Carlo runs are divided into a behavioral and a non-behavioral group according to their model performance for the calibration period. Behavioral parameter sets are the parameter sets that are also used for prediction with a KGE > 0.8. The cumulative probability density function of the behavioral group is then plotted over the respective parameter calibration range, indicating whether the model parameters can be considered to be sensitive (Beven, 2008). A distribution of the behavioral group that deviates a lot from the 1:1 line, which corresponds to a uniform distribution, indicates a very sensitive parameter as this distribution shows that the parameter value has a large influence on the overall model performance.

3.3 Tracer modelling

In this thesis tracer transport is modelled based on the combination of the VarKarst model with a simple separate approach for tracer modelling. The goal is not to model the exact observed tracer breakthrough curves, but to derive flow characteristics from VarKarst discharge simulations as well as site characteristics for each tracer test and to generate simplified tracer breakthrough curves using this information.

First, the breakthrough curves of the nine tracer tests executed in the catchment area are standardised in order to enable a consistent analysis and a better comparability between the different tracer tests. In this way, the different tracer breakthrough curves can be compared independent of the respective mass of tracer that was injected or the current level of discharge at the springs. The standardisation is performed by dividing the observed tracer concentrations of each breakthrough curve through the integral of the respective breakthrough curve. In this way, the integral of all resulting standardised tracer breakthrough is 1.

Some of the observed tracer breakthrough curves show very complex shapes with two or even more peaks (Figure 7 and Figure 8). These curves are considered to be too complex to be predicted in their exact shape. Therefore, the observed tracer breakthrough curves are simplified by fitting a simple 1D advection-dispersion model (equation (50)), similar as in Leibundgut (2009), to the curves. This simple model is the solution to the 1D transport equation (Leibundgut, 2009). An initial concentration of zero and an input of all tracer at once are assumed. Tracer loss from injection point to spring is not considered in this approach, therefore full tracer recovery is assumed.

$$c(x,t) = \frac{x}{\sqrt{4\pi D_L t^3}} e^{-\frac{(x-\frac{x}{t_0}t)^2}{4D_L t}} \tag{50}$$

With
- c Standardised concentration [-]
- x Linear distance from tracer injection point to spring [m]
- t Time after injection [s]
- D_L Longitudinal dispersion coefficient [m^2*s^{-1}]
- t_0 Advection time [s]

In order to simplify the breakthrough curves, the advection-dispersion model is only fit to the main peak of each tracer test. The selection of the main peaks is carried out in consultation with experts from the Karst Research Institute SRC SAZU. Through fitting the advection-dispersion model to the breakthrough curves, each simplified breakthrough curve can be described by two transport parameters,

the longitudinal dispersion coefficient D_L and the advection time t_0. The KGE (equation (49)) is used as an objective function for the fit of the simplified model to the observed breakthrough curves. In some cases the fit that is achieved by the maximisation of the KGE is altered manually to achieve a better visual fit.

Each observed tracer breakthrough curve can now be described in a simplified form by only two transport parameters, D_L and t_0. These two parameters are analysed for correlations with flow conditions and site characteristics of the respective tracer experiments, not considering the tracer experiments T1 and T9. In case of T9, the distance of the injection point from the spring is considered too large for the tracer test to still be comparable with other tracer tests conducted in a much closer location to the Unica Springs. Furthermore, the thickness of the vadose zone at the injection point of T9 is much larger compared to other injection points. For T1, the very complex and elongated observed tracer breakthrough curve is considered to be unrepresentative and not suitable for the establishment of correlations. For the purpose of finding correlations with transport parameters, different flow and site characteristics of the tracer tests are identified or computed and combined. Some of them are displayed in Table 1. As previously described, the hydrological condition is perceived to have a strong impact on transport processes in karst systems. In order to correlate different hydrological conditions with transport parameters, they need to be quantified. This is done by computing several discharge parameters to describe the hydrological conditions of each tracer test. For each tracer test the mean discharge during the duration of the tracer experiment Q_{mean_cal}, from tracer injection until the end of the main peak of the observed breakthrough curve, is calculated. Furthermore, the peak discharge Q_{peak} associated with the respective main concentration peak of each tracer test is calculated and the recorded discharge during tracer injection Q_{inj} is gathered. In addition, parameters that describe the site characteristics specific to the each injection point, like the distance from the Unica Springs, are gathered. They are listed in Table 1 for the different tracer tests.

The obtained quantified flow and site parameters and different combinations between the parameters are analysed in combination with the transport parameters in order to find correlations between them. The correlations are quantified using the squared correlation coefficient R^2, based on the Pearson correlation coefficient r (equation (51)) (Dormann, 2017).

$$r = \frac{\sum_{i=1}^{n}(x_{i1} - \overline{x_1})(x_{i2} - \overline{x_2})}{\sqrt{\sum_{i=1}^{n}(x_{i1} - \overline{x_1})^2 \sum_{i=1}^{n}(x_{i2} - \overline{x_2})^2}} \tag{51}$$

With x_{i1} and x_{i2} being the simulated and observed values and $\overline{x_1}$ and $\overline{x_2}$ being their mean values, a correlation coefficient near 0 indicates no correlation, whereas a value near 1 indicates a strong correlation between the two variables.

In the last step, the best correlations are used to predict the transport parameters of the tracer tests and therefore their simplified tracer breakthrough curves from only the flow and site characteristics of the respective tracer tests. The chosen correlations that determine the transport parameters from flow and site characteristics are the correlation of t_0 and D_L with the guessed actual distance between injection point and Unica Springs ($guessAD$) in combination with the mean discharge from tracer injection until the end of the main tracer peak (Q_{mean_cal}). When the simplified breakthrough curves are predicted from modelled spring discharge, Q_{mean_cal} is estimated based on the modelled discharge time-series. The estimated actual distance only varies with the study site, not with spring discharge.

As in the calibration of the VarKarst model not one parameter set is selected for prediction but several parameter sets with a high performance are selected, this also leads to several Q_{mean_cal} parameters that are derived from the respective discharge simulations of all selected parameter sets. In turn, this

leads to a variety of predicted values of t_0 and D_L and therefore to a variety of simulated tracer breakthrough curves. In this way, a range of breakthrough curves is modelled and the uncertainty in discharge modelling is also reflected in the prediction of tracer breakthrough curves. However, for the visualisation of the simulated tracer breakthrough curves only a random set of 100 parameter sets out of all behavioural parameter sets is used.

For the application of climate or land-use scenarios, the scenarios are applied to the VarKarst model, which then simulates spring discharge based on the different scenarios. This can lead to changes in Q_{mean_cal}, which is derived from the modelled discharge time-series. The changes in Q_{mean_cal} can then lead to changes in the predicted transport parameters t_0 and D_L and therefore to changes in the predicted simplified tracer breakthrough curves.

4. Results

4.1 Discharge modelling

In the calibration of the VarKarst model with the Monte Carlo analysis, parameter sets that lead to a $KGE > 0.8$ between observed and simulated discharge for the calibration period are selected for prediction. Out of the 250,000 Monte Carlo runs, 5,755 runs lead to a $KGE > 0.8$, which equals 2.3% of all Monte Carlo runs. These runs are considered as behavioural runs. The mean KGE of all selected runs is then 0.82 for the calibration period and 0.71 for the validation period. As not one single parameter set is selected by calibration but 5,755, there is not one resulting discharge simulation, but a range of possible simulations, which takes model uncertainty into consideration when discharge is simulated. This is visible in Figure 14, which shows the simulated discharge exemplary for the calibration period in the time period of May 2008 until September 2009. The simulated discharge is displayed as a range. Tracer tests T2 – T8 took place in this period between May 2008 and September 2009. The tracer injection times are marked in red. Chronologically, at the first injection mark T2 and T3 were injected. At the second injection mark T4 and T5 were injected and the third injection mark shows the injection date of T6, T7 and T8. The figure shows that the general course of observed discharge is well reproduced by the model. In the beginning of the time period some observed discharge peaks are not simulated by the model. For high discharge peaks, the model uncertainty becomes very large and the highest discharge values of the uncertainty band become very high. The observed discharge in Figure 14 is never higher than approximately 80 m³/s. This is due to the inability of the Hasberg gauging station to record higher discharges of the Unica River. In Figure 14 periods where the discharge could potentially be higher than 80 m³/s appear as plateaus. The simulated discharge peaks often exceed these plateaus. In general, the extent of steep discharge peaks tends to be underestimated by the model.

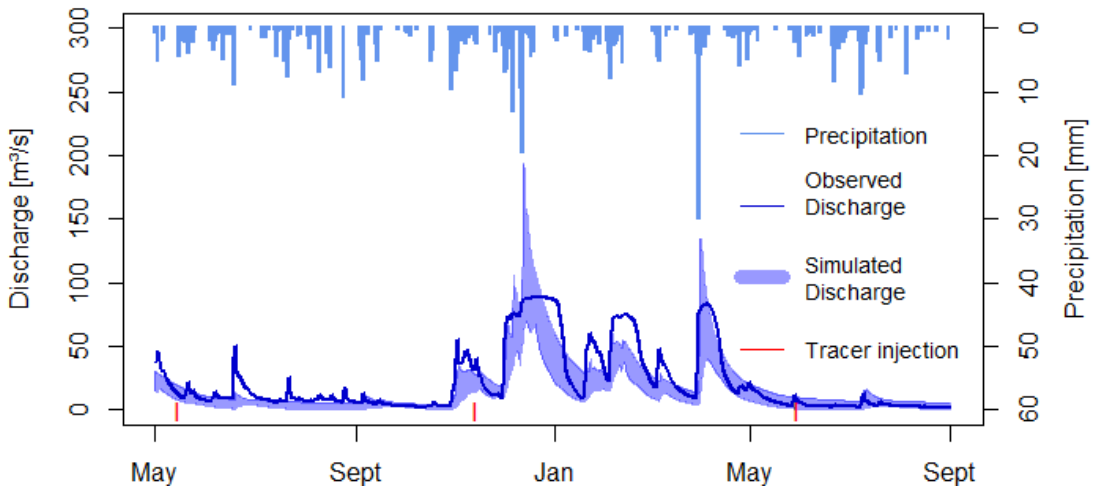

Figure 14: Simulated discharge for the time period May 2008 until September 2009 in the calibration period

Figure 15 shows the simulated discharge exemplary for the validation period for the hydrological year 2014. This time period is chosen for visualisation as tracer test T9 takes place in this hydrological year. Its injection date is marked in red. Similar to the discharge simulations for the calibration period, the general course is well captured by the model. Also, some discharge peaks in June and July are not simulated by the model. For the big discharge peak in December, model uncertainty becomes very large and two discharge peaks are simulated instead of one observed peak.

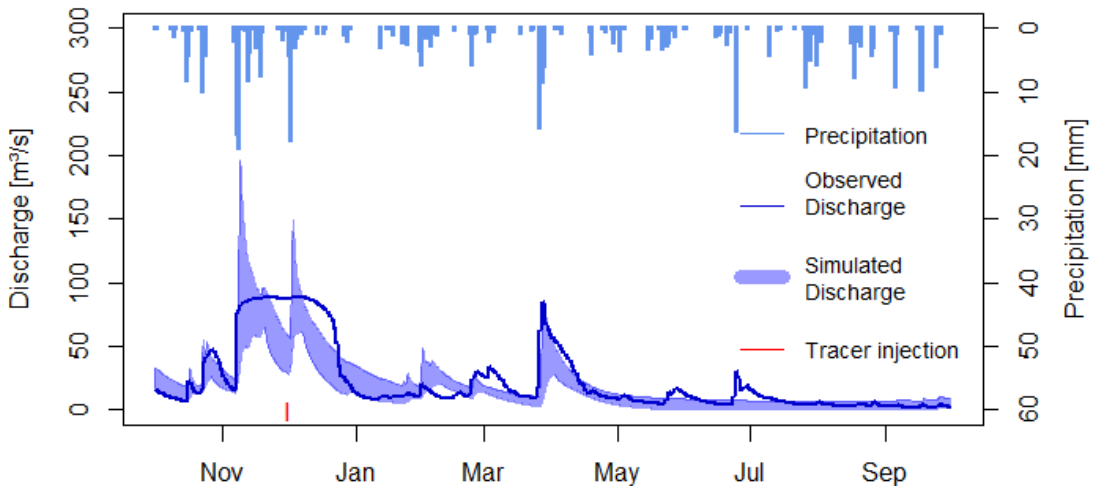

Figure 15: Simulated discharge for the hydrological year 2014 in the validation period

Figure 16 until Figure 20 show the sensitivity analysis of the calibrated VarKarst model parameters. Parameter sets that achieve a KGE of over 0.8 are considered as behavioural. In the dotty plot on the left side of the figures, the KGE achieved by the parameters sets for the calibration period is plotted over the parameter value of the respective parameter set. Behavioral runs are displayed in light blue with the parameter reaching the best model performance highlighted in darker blue. On the right side of the figure, the HSY analysis is displayed with the cumulative distribution of behavioural runs plotted over the parameter calibration range. The most sensitive parameter according to the sensitivity analysis is K_{epi} (Figure 16). For this parameter, a clear pattern is visible in the dotty plot and the cumulative distribution of the behavioural runs deviates strongly from the 1:1 line, which represents a uniform distribution, indicating that the value of parameter K_{epi} has a strong influence on the performance of the model output.

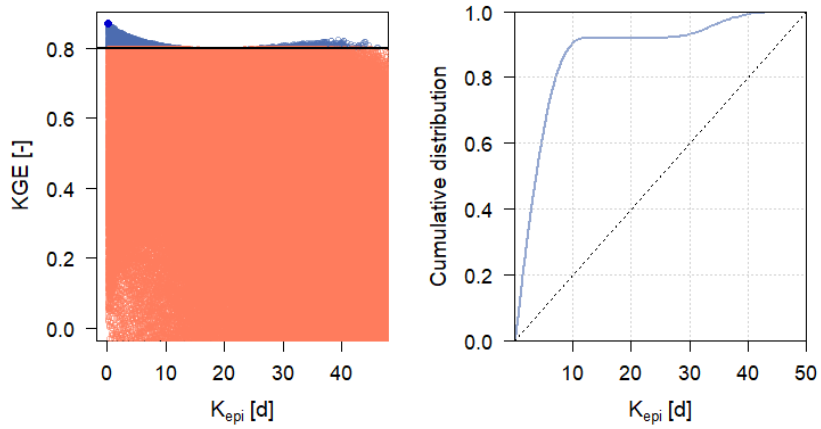

Figure 16: Sensitivity analysis for VarKarst model parameter K_{epi}

For the parameters V_{epi} and α_{fsep} in Figure 17 and Figure 18 there is no such clear pattern in the distribution of behavioural runs in the dotty plots. Their cumulative distributions deviate from the 1:1 line, but not as strong as for K_{epi}.

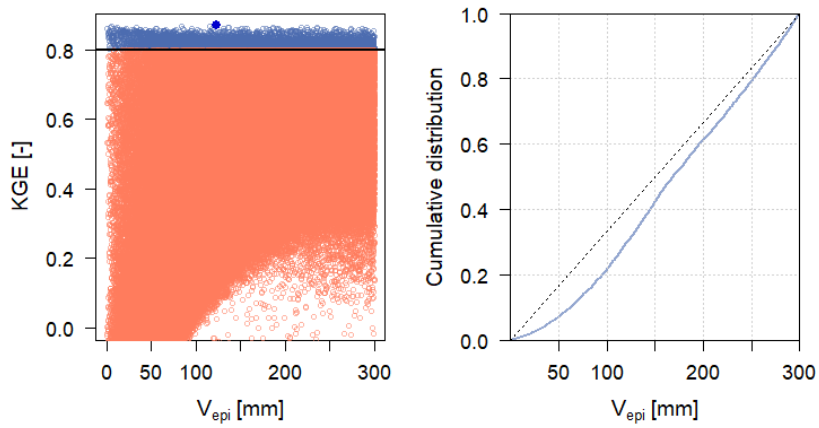

Figure 17: Sensitivity analysis for VarKarst model parameter V_{epi}

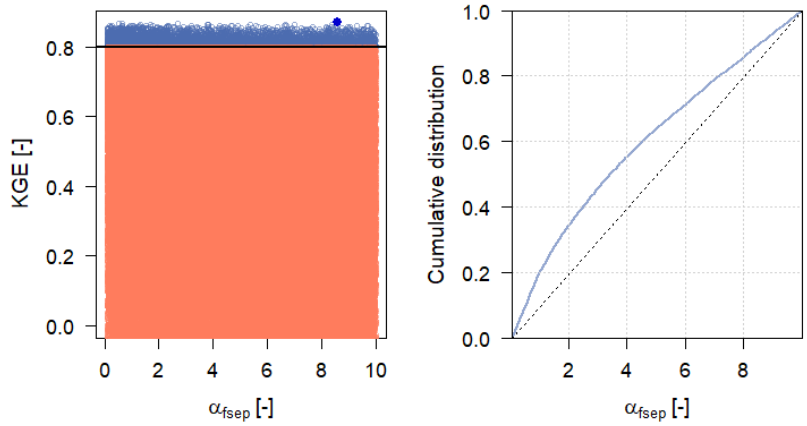

Figure 18: Sensitivity analysis for VarKarst model parameter α_{fsep}

For the parameters α_{gw} and K_C in Figure 19 and Figure 20, there is a distinct deviation of the cumulative distribution from the 1:1 line and a visible pattern in the distribution of behavioural runs is visible in the dotty plots.

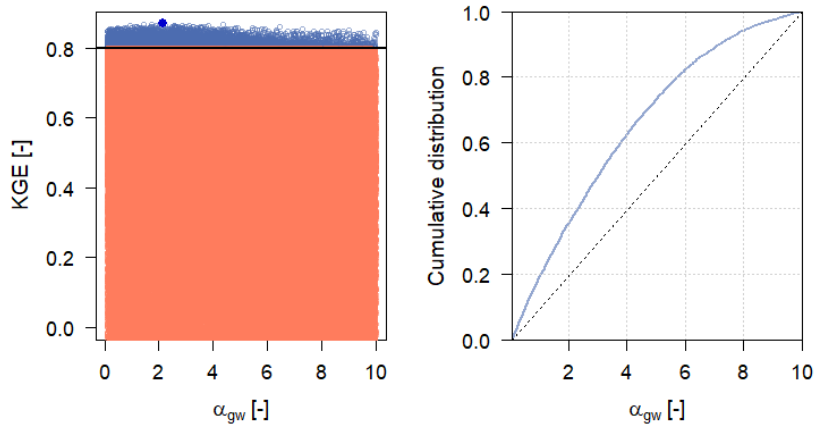

Figure 19: Sensitivity analysis for VarKarst model parameter α_{gw}

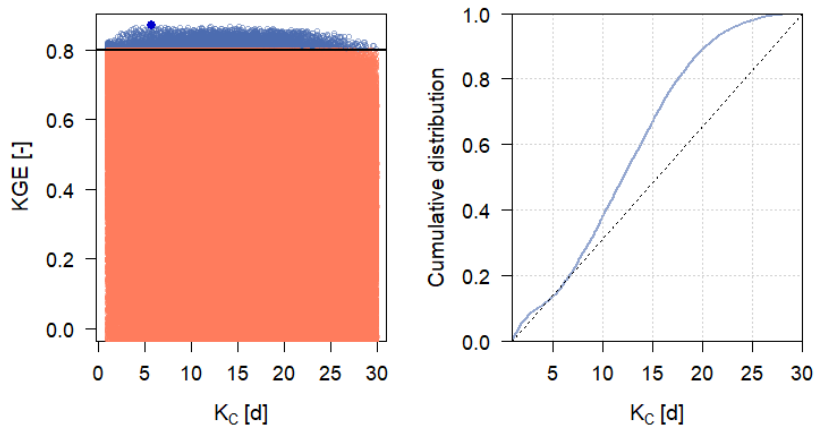

Figure 20: Sensitivity analysis for VarKarst model parameter K_C

Figure 22 until Figure 24 show the simulated discharge of the period from May 2008 until September 2009 with initial climate and land-use conditions compared to different applied scenarios. The discharge simulations are again displayed as an uncertainty band. The discharge simulations with initial climate and land-use conditions are plotted in blue, the discharge simulations with applied scenarios are plotted in yellow. If both bands overlap, the area is coloured in grey. In scenarios where changes in climate are considered, the visualised precipitation is the precipitation of the climate scenarios. For the climate uncertainty scenario, the variation in precipitation input is visualised. The lowest precipitation input is displayed in grey and the largest precipitation input in blue. In Figure 21 the mean changes of the water balance components discharge, potential evapotranspiration and precipitation for the visualised time-series are displayed for all scenarios.

For the RCP2.6 and RCP8.5 climate scenarios in the changes in water balance components for the scenarios compared to initial conditions show a mean increase of all components for the time-series. For the input parameters, the increase in precipitation is higher for RCP2.6 and the increase in potential evapotranspiration is higher for RC8.5. The resulting increase in discharge is higher for the RCP2.6 scenario. For the climate uncertainty scenario, the highest changes in water balance components are visualised in the colours blue and orange and the lowest changes are visualised in grey. The figure shows that the mean of the simulated scenario discharge ranges from a decrease of almost 20 % up to a very high increase of almost 60 %. Regarding the simulated time-series with the climate scenarios RCP2.6 and RCP8.5 in Figure 22, for high discharge values there is a slight tendency to even higher scenario discharges. The top and the bottom of the uncertainty band of the climate scenario discharge here are higher than the top and the bottom of the uncertainty band of the initial discharge simulation. In some parts of the time-series however also the opposite can be observed where the simulated scenario discharges are slightly higher than the initially simulated discharges. For the climate uncertainty scenario, the uncertainty band of the discharge simulations becomes even wider and completely contains the initial discharge simulation ranges.

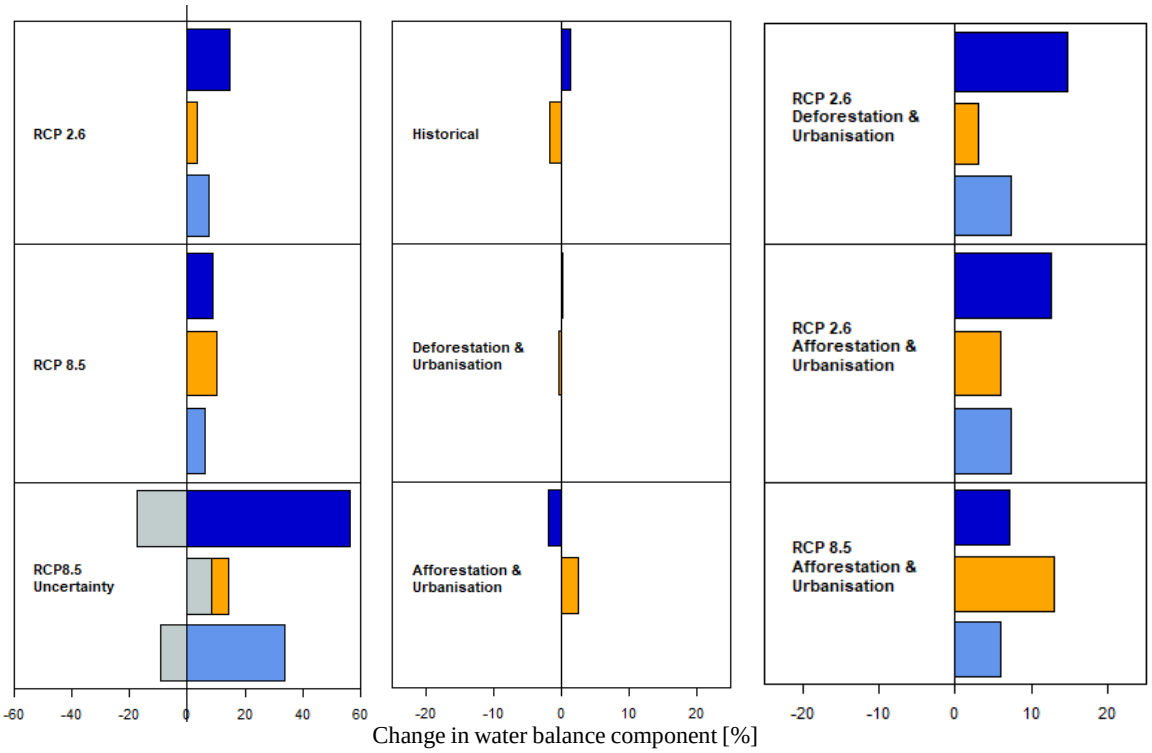

Figure 21: Proportional changes in the water balance components discharge (dark blue), potential evapotranspiration (orange) and precipitation (light blue) for the climate-, land-use- and combined scenarios relative to the initial conditions for the time-series of May 2008 until September 2009

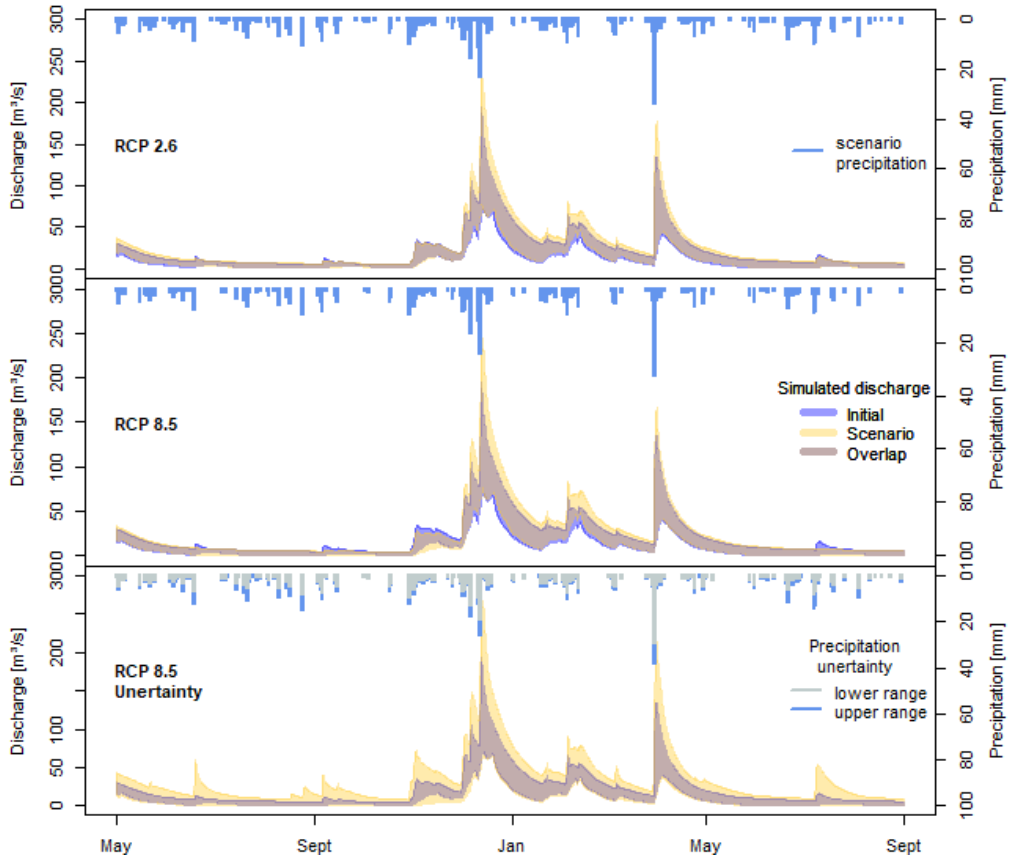

Figure 22: Simulated discharge for the time period May 2008 until September 2009 for the climate scenarios in comparison to initial conditions

In Figure 23 for all land-use scenarios, the deviation of simulated scenario discharge from initially simulated discharge in the simulated time-series is very small. In the historical land-use scenario and

the deforestation & urbanisation scenario only the highest discharge simulations, which are represented by the top of the uncertainty band, are simulated a little higher for the biggest peaks by the scenarios compared to the initial simulation. In the afforestation & urbanisation scenario, the top of the uncertainty band is very slightly less high than in the initial simulations. For the very most part however, simulated discharge ranges based on land-use change scenarios and initially simulated discharge ranges completely overlap. The mean changes in the water balance components over the time-series (Figure 21) are also much smaller compared to the changes caused by the climate scenarios. For the historical as well as the Deforestation & Urbanisation scenario, there is a slight decrease of potential evapotranspiration leading to a slight increase of discharge. In the Afforestation & Urbanisation scenario the changes occur in the opposite way with an increase in potential evapotranspiration and therefore a decrease of discharge.

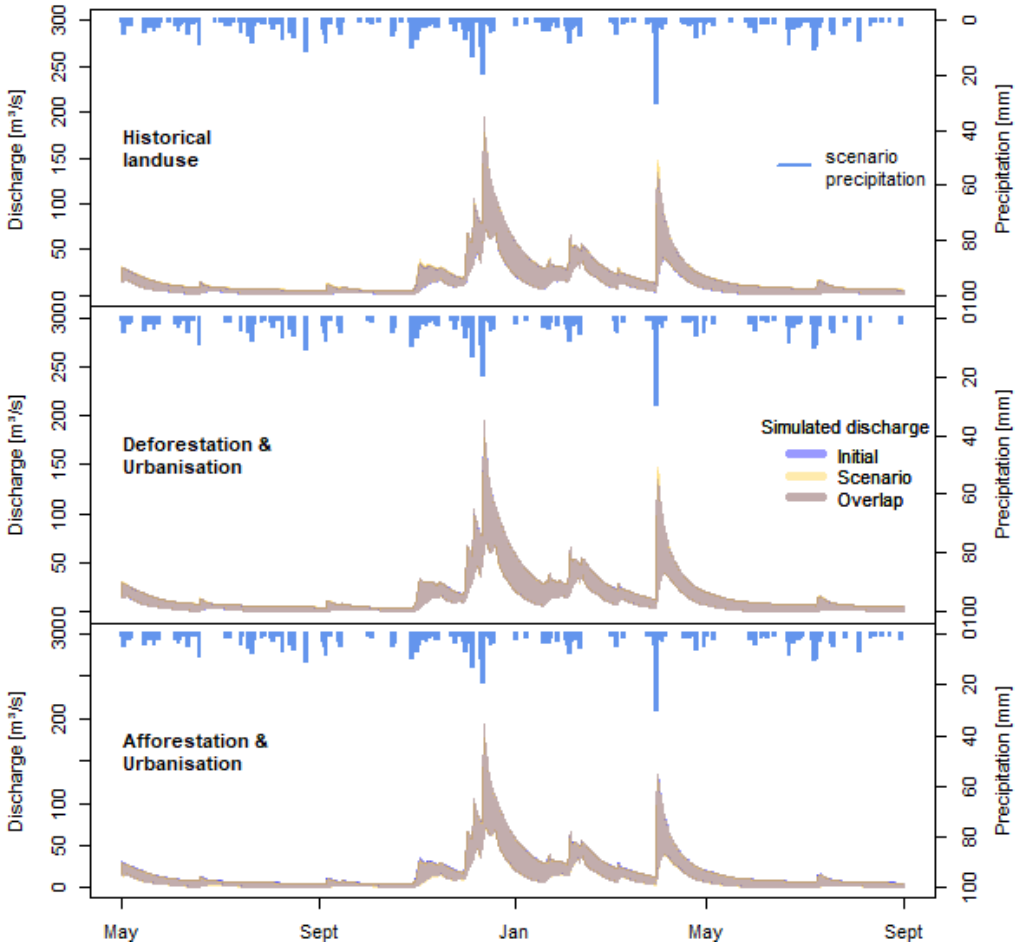

Figure 23: Simulated discharge for the time period May 2008 until September 2009 (left) for the land-use scenarios in comparison to initial conditions

For the changes in water balance components for the combined scenarios in Figure 24 the patterns are dominated by the impacts of the climate scenarios with an increase in all components. The combination of RCP2.6 and Deforestation & Urbanisation scenarios is very close to the climate scenario RCP2.6 in both the changes water balance components and the simulated scenario discharge time-series. For the RCP 2.6 and Afforestation & Urbanisation scenario the increase of potential evapotranspiration is larger than the increase of potential evapotranspiration of the single scenarios and results from their combination. The increase in discharge is slightly lower in this combined scenario compared to the RCP2.6 scenario. For the combination of RCP8.5 with Afforestation & Urbanisation, the increase in potential evapotranspiration is the highest of all analysed scenarios. The mean discharge still increases but to a lesser extent than in the RCP8.5 scenario. The time-series of the combined scenarios in Figure 24 resemble the time-series of the climate scenarios very much.

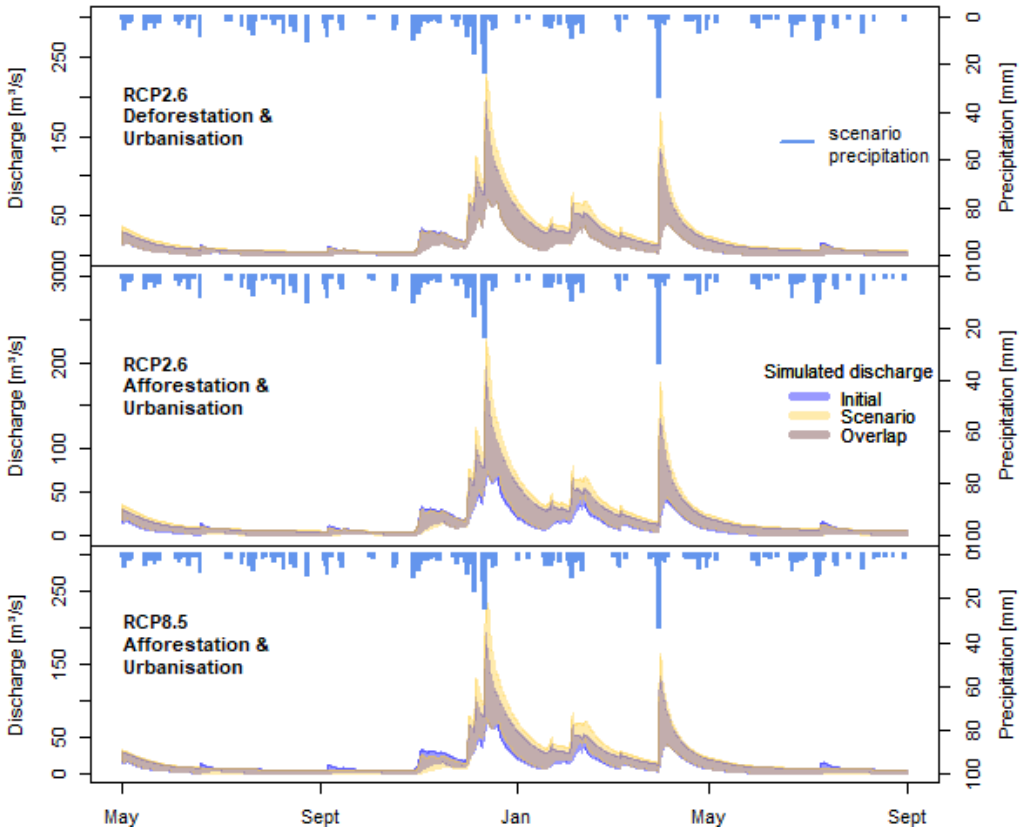

Figure 24: Simulated discharge for the time period May 2008 until September 2009 (left) for the combined climate and land-use scenarios in comparison to initial conditions

For all applied scenarios, the simulated initial discharge and the simulated scenario discharge are never not overlapping, indicating that the simulated changes are always smaller than the model uncertainty.

4.2 Tracer modelling

The fit of the advection-dispersion model to the observed tracer breakthrough curves of all tracer tests is shown in Figure 25. The modelled tracer breakthrough curves, which are displayed in red or blue, are therefore the basis for all further transport analysis. For all 9 tracer tests, the observed breakthrough curves are plotted in black. The simplified breakthrough curves that were fit according to the maximisation of the KGE between simplified and observed breakthrough curves are plotted in red. For tracer test T1 and T9, in addition to the automatic fit according to the KGE a manual fit is displayed, which should achieve a better visual fit of the simplified breakthrough curve with the observed breakthrough curve. All observed tracer breakthrough curves are therefore simplified to one single main peak and can be described by the two transport parameters t_0 and D_L. The respective transport parameters for all tracer tests are displayed in Table 7.

Table 7: Estimated transport parameters for the tracer tests

Tracer test	t_0 [s]	D_L [m^2*s^{-1}]
T1	6.1.E+06	1.18
T2	3.3.E+05	2.38
T3	2.1.E+05	8.24
T4	1.1.E+06	4.49E-01
T5	5.8.E+05	1.47
T6	3.5.E+06	4.22E-03
T7	2.7.E+06	8.09E-02
T8	3.3.E+06	6.92E-03
T9	3.5.E+06	1.31

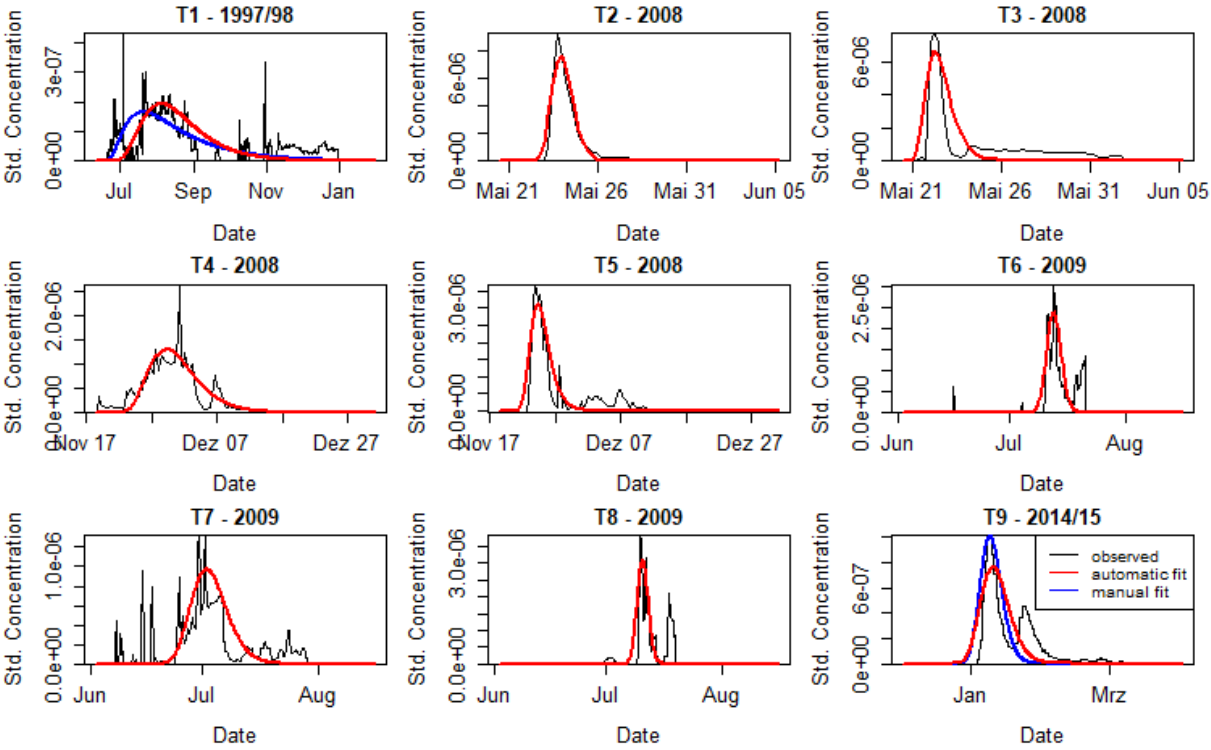

Figure 25: Fit of simplified advection-dispersion models to the observed tracer breakthrough curves

The best correlation of a combination of flow and site characteristics with the transport parameter t_0 that was found is shown in Figure 26. The best correlation with t_0 could be achieved with the combination of estimated actual distance of the tracer injection point from the Unica Springs ($guessAD$) with the mean discharge during the tracer experiment (Q_{mean_cal}). A linear regression model is fit to the correlation on a half-logarithmic scale as shown on the left side in Figure 26. The transition of the correlation to linear scale is shown on the right side. The equation of the linear regression model as well as the R^2 value of the correlation are also displayed in Figure 26. The correlation indicates that higher discharge during the tracer experiment and a larger distance between injection point and Unica Springs lead to lower values of t_0 and therefore to shorter advection times.

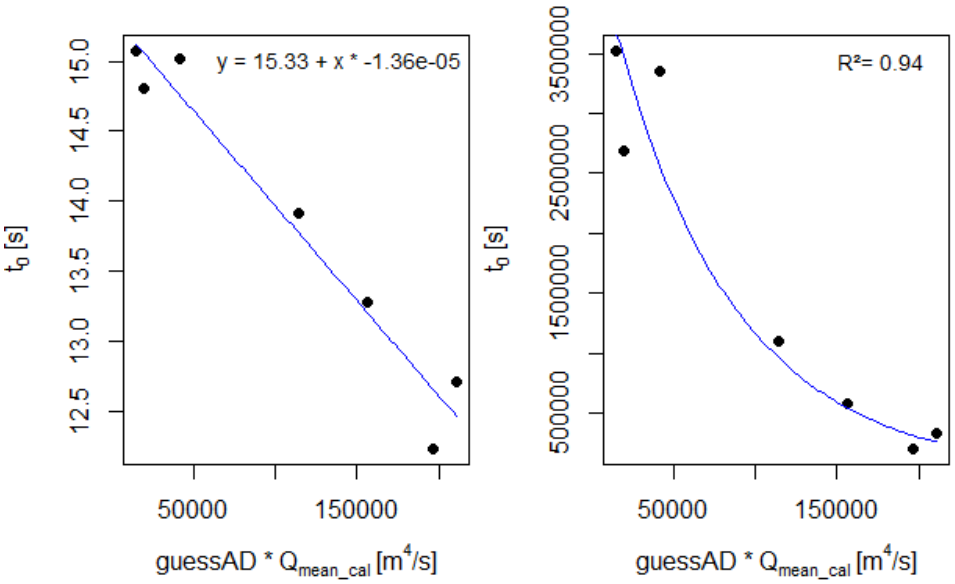

Figure 26: Correleation between estimated actual distance between injection point and Unica Springs (guessAD) and the mean spring discharge during the calibration period (Qmean_cal) with the advection parameter t_0, including tracer tests T2 until T8, left: logarithmic y-axis

For the transport parameter D_L, the best correlation was found on the half-logarithmic scale with the same set of flow and site parameters, a combination of estimated actual distance of the tracer injection point from the Unica Springs ($guessAD$) with the mean discharge during the tracer experiment (Q_{mean_cal}). The fit of a linear regression model in the double-logarithmic scale is shown on the left in Figure 27 and the correlation is shown on a linear scale on the right side. The equation of the linear regression model as well as the R² value of the correlation are also displayed in Figure 27. The figure shows that for larger mean discharge values and longer distances between injection point and Unica Springs, the parameter D_L becomes larger.

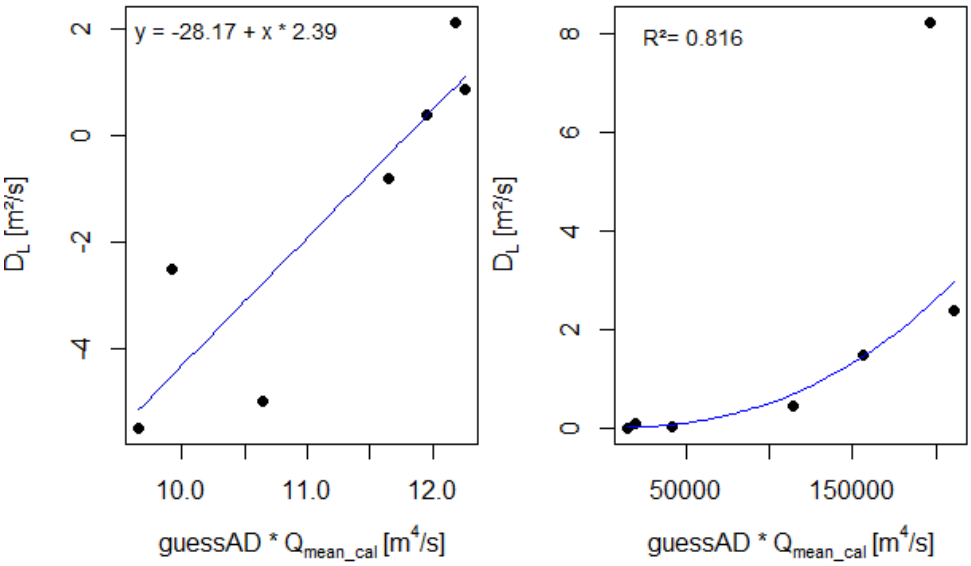

Figure 27: Correleation between estimated actual distance between injection point and Unica Springs ($guessAD$) and the mean spring discharge during the calibration period (Q_{mean_cal}) with the advection parameter D_L, including tracer tests T2 until T8, left: logarithmic y-axis and x-axis

Furthermore, a strong correlation between the two transport parameters t_0 and D_L has been observed as shown in Figure 28. The equation of the linear regression as well as the R² value of the correlation are also included in the figure.

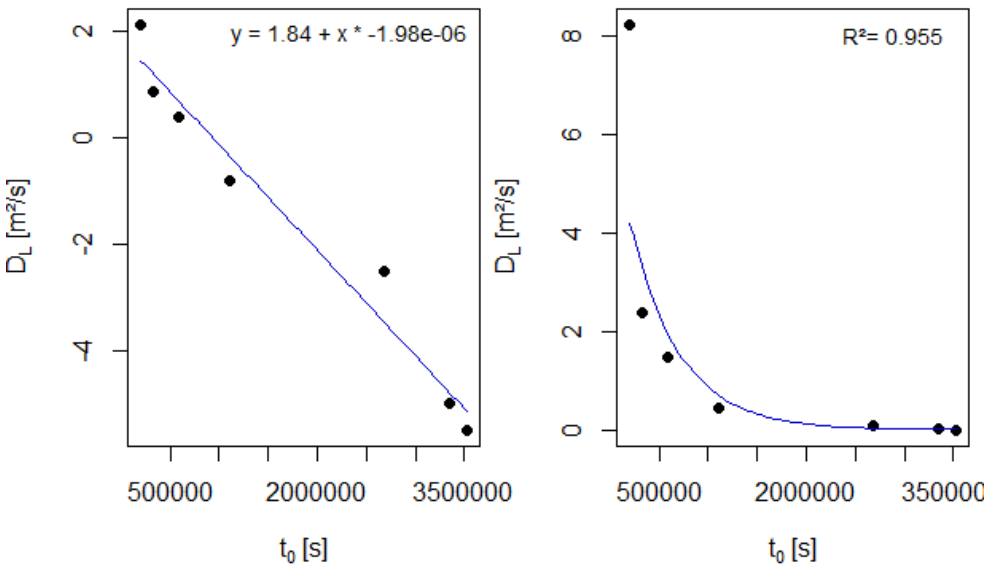

Figure 28: Correlation between the two transport parameters t_0 and D_L

Figure 29 shows the simulated tracer breakthrough curves, which are derived from the correlations shown in Figure 26 and Figure 27. The mean discharge during the tracer experiment, which is used for the calculation of the transport parameters, is derived from the discharge runs simulated by the VarKarst model. For visualisation, 100 random discharge runs are picked for the calculation of the transport parameters. The range of these 100 exemplary simulated breakthrough curves is displayed in grey and the observed breakthrough curves in blue. For each tracer test one of the 100 exemplary simulated breakthrough curves, which provides the best fit to the observed curve, is indicated in a slightly darker grey to illustrate that the range is composed of several single curves. For T1, the simulated tracer breakthrough curves are much shorter than the observed breakthrough curve with much higher concentrations. The simulation predicts that all tracer arrives at the springs during the first, small concentration peak of the observed curve. The simulated breakthrough curve is therefore much shorter and reaches much higher concentrations than the observed breakthrough curve. For T2, the simulated and observed breakthrough curves overlap. In case of T3, the observed breakthrough curve occurs earlier after injection and reaches higher concentrations than all simulated breakthrough curves. For T4, the observed breakthrough curve mostly overlaps with the range of simulated breakthrough curves. In case of T5, the range of simulated breakthrough curves predicts a much earlier breakthrough curve with higher concentrations than the observed curve. For T6, T7 and T8, the main tracer peaks lie within the simulated range of breakthrough curves. The simulated curves range over more than one month. For T9, the simulation of breakthrough curves based on VarKarst simulations and correlations does not produce reasonable results.

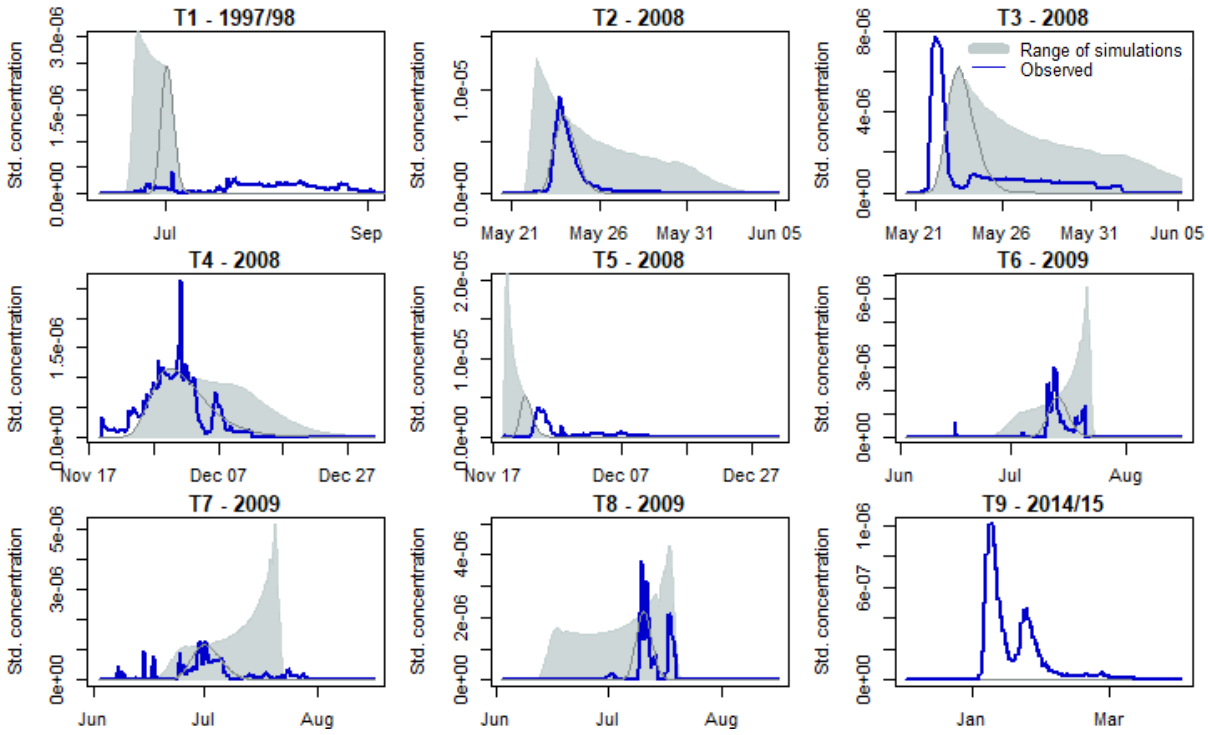

Figure 29: Simulated tracer breakthrough curves using flow parameters from the calibrated VarKarst model and the tracer correlations

The simulated ranges of possible tracer breakthrough curves with initial conditions compared to different applied climate and land-use scenarios are displayed for T1 until T8 in Figure 30 until Figure 39. For T9, the calculation of the transport parameters from the correlations does not lead to reasonable values for the transport parameters. Therefore, no scenario analysis is possible. The range of initial breakthrough curve simulations is displayed in blue. The range of scenario breakthrough curve simulations is displayed in yellow. Overlapping scenarios are plotted in grey. In Figure 30 the different scenarios are displayed for tracer test T1. Regarding the basic scenarios, the largest change in simulated breakthrough curve range compared to the initial conditions is computed by the climate scenario RCP8.5. The simulated curves shift towards a later arrival time with higher maximum concentrations. For the RCP2.6 and the Afforestation & Urbanisation scenario, a slight shift towards later tracer arrival can be observed. For the remaining two land-use scenarios, the initial and scenario ranges change even less, but in the other way, and mostly overlap. For the combined scenarios, the combination of both climate scenarios with the Afforestation & Urbanisation scenario enhances the changes so that the largest changes can be observed for the combined scenario RCP8.5 with Afforestation & Urbanisation. The climate uncertainty scenario shows that the consideration of climate projection uncertainty leads to even larger uncertainties in transport simulations. The resulting range of simulated breakthrough curves becomes very wide and completely entails the initial range of simulated curves.

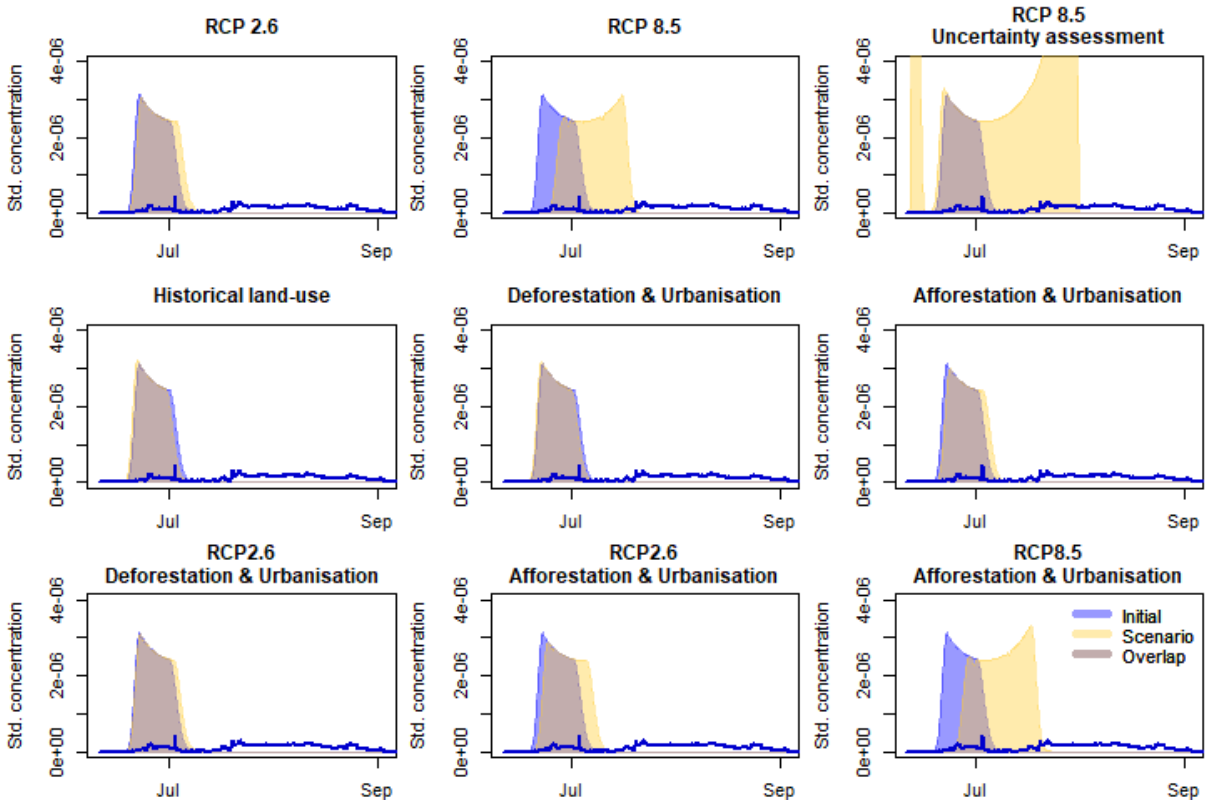

Figure 30: Tracer breakthrough curve simulations with climate and land-use scenarios including tracer breakthrough curve simulations with initial conditions for T1

For T2 in Figure 31 and T3 in Figure 36 in the appendix both climate scenarios RCP2.6 and RCP8.5 lead to a shift of the simulation ranges forward in time and to higher maximum concentrations. For RCP2.6 this shift is more pronounced. The climate uncertainty simulation range again completely contains the initial range with maximum simulated concentrations that become several times higher than the initial maximum simulated concentration. For the Afforestation & Urbanisation scenario, there is a slight shift of the simulation range back in time and a very slight decrease of maximum concentration. For the remaining two land-use scenarios no change of simulation range can be observed. The combined scenarios show very similar scenario ranges as the climate scenarios.

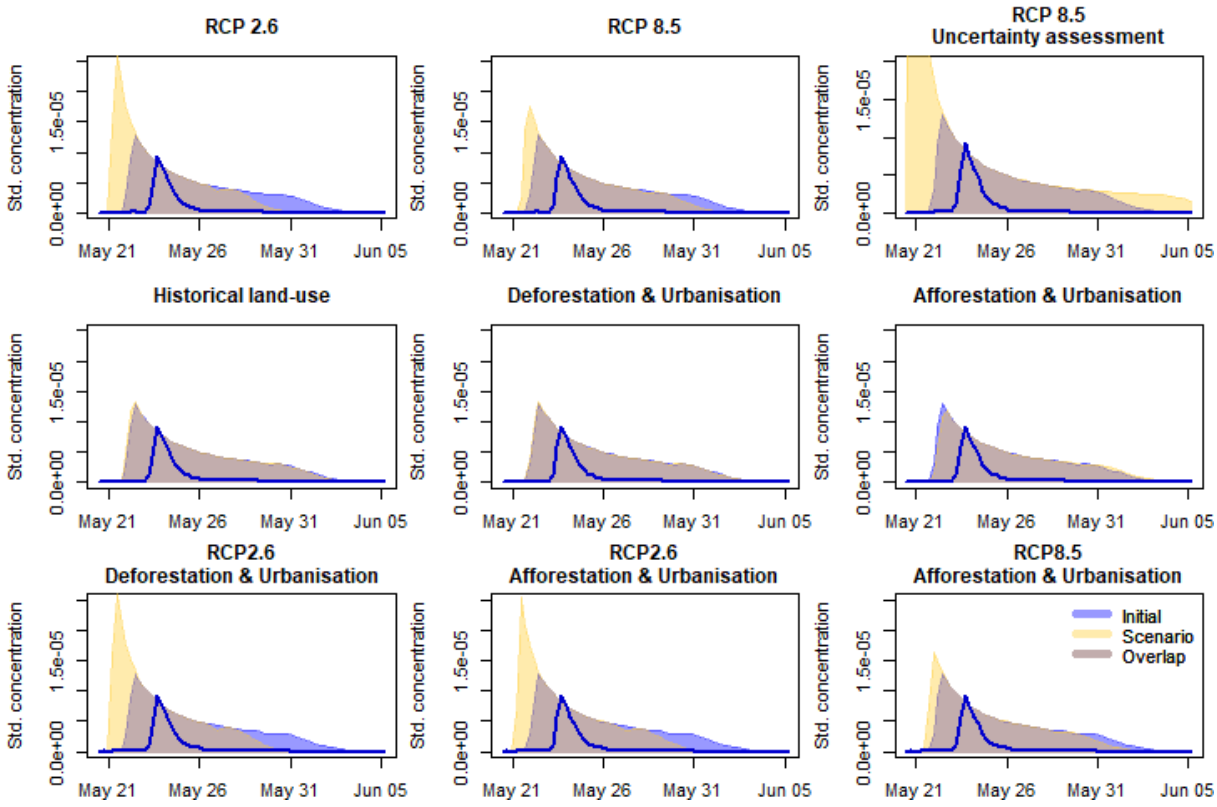

Figure 31: Tracer breakthrough curve simulations with climate and land-use scenarios including tracer breakthrough curve simulations with initial conditions for T2

In case of T4 in Figure 32, the RCP8.5 scenario leads to a shift of the simulated breakthrough range towards later tracer arrival with slightly smaller maximum concentrations. The same shift but only to a very small extent can be observed for the Afforestation & Urbanisation scenario. For the other climate and land-use scenarios, the initial and scenario breakthrough curve ranges mostly overlap. Also for the combined scenarios, the largest change in simulated breakthrough curve ranges can be observed for the combination of RCP8.5 and Afforestation & Urbanisation scenario. Both other combinations mostly overlap with the initial simulations. The climate uncertainty consideration again shows that the resulting breakthrough curve ranges become very wide with changes towards both directions, faster arrival times with higher maximum concentrations as well as slower arrival times with lower maximum concentrations. For T5, the scenarios lead to similar results as for T4 with a shift of the simulated range towards later arrival times with lower maximum concentrations for RCP8.5 and the same change for the Afforestation & Urbanisation scenario, but to a lesser extent. The two scenarios again lead to the largest observable changes for T5 in the combined scenario with RCP8.5 and Afforestation & Urbanisation. For the other scenarios, most of the simulated ranges overlap with the initial simulated ranges. Except for the climate uncertainty scenario, where the simulated breakthrough curve range becomes again very wide so that it completely entails the initial simulations. The simulated transport scenarios for T5 can be found in Figure 37 in the appendix.

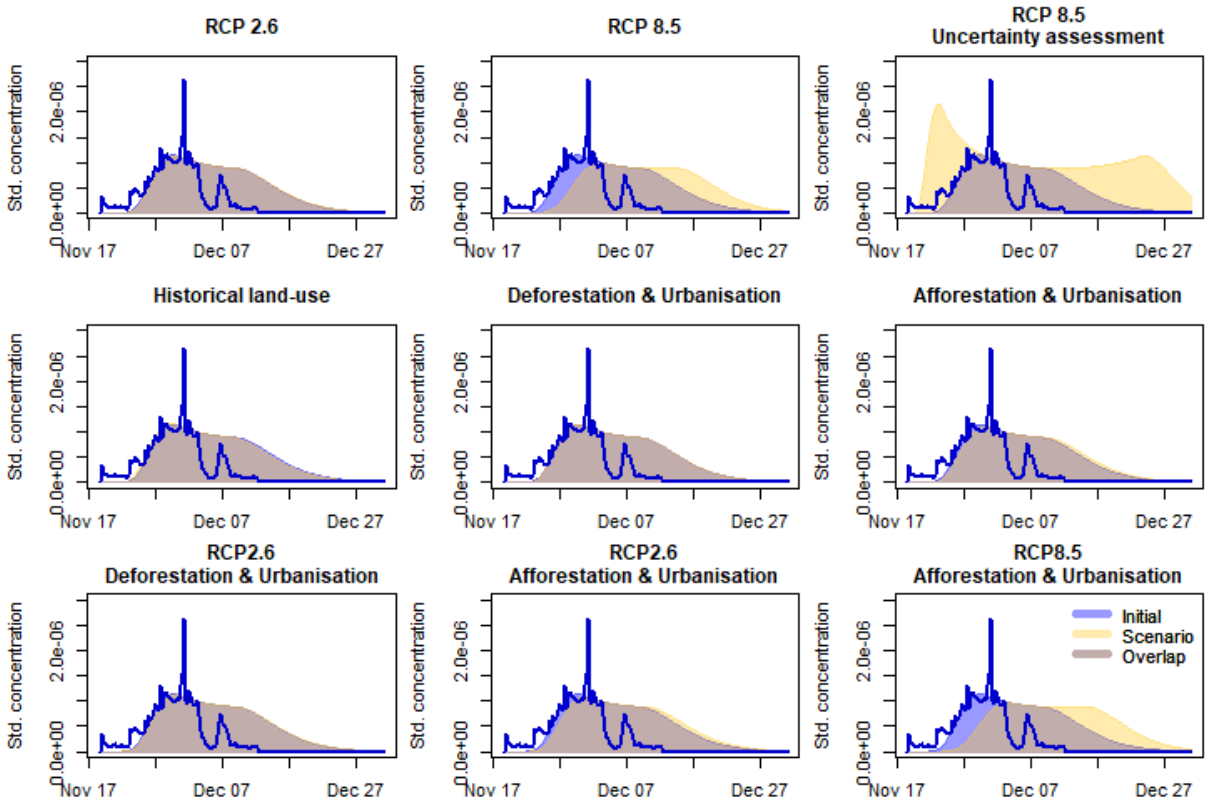

Figure 32: Tracer breakthrough curve simulations with climate and land-use scenarios including tracer breakthrough curve simulations with initial conditions for T4

For all three tracer tests T6, T7 and T8, similar changes in simulated scenario ranges can be observed. For the RCP2.6 climate scenario, a small shift towards earlier arrival times can be observed with slightly lower maximum concentrations. The initially simulated ranges of breakthrough curves mostly overlap with the simulated scenario ranges for all land-use scenarios. In the RCP8.5 climate scenarios, the simulated scenario ranges slightly shift towards later arrival times with higher concentrations for T6, for T7 and T8 they shift towards slightly earlier arrival times with lower concentrations. The climate uncertainty scenarios again show very wider ranges that completely entail the initial simulation ranges. Exemplary, the simulated transport scenarios for T6 can be found in Figure 33. The simulations for T7 and T8 can be found in Figure 38 and Figure 39 in the appendix.

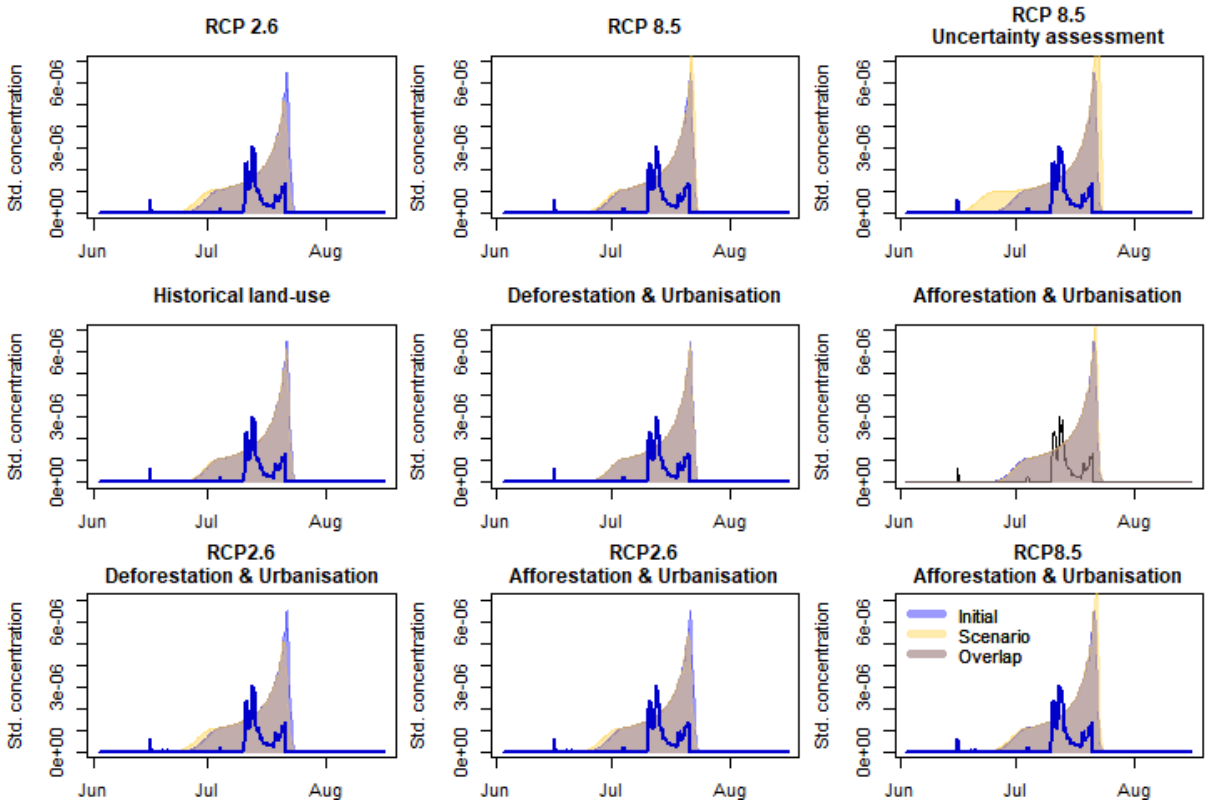

Figure 33: Tracer breakthrough curve simulations with climate and land-use scenarios including tracer breakthrough curve simulations with initial conditions for T6

For all tracer tests, there is no scenario where the initial simulation range and the scenario simulation range do not overlap indicating that the simulated changes in breakthrough curves are never as big as the simulation uncertainties.

Figure 34 and Figure 35 show exemplary for tracer tests T2 and T4 the changes of the water balance components during the tracer experiments for the different scenarios, except the climate uncertainty scenario. The two tracer tests differ in the changes caused by the climate scenarios. For T2 there is an increase of precipitation and a smaller increase of potential evapotranspiration leading to an overall increase in discharge. For T4 the increase in precipitation is smaller than for T2 while the increase in potential evapotranspiration is larger than for T2. Overall, for T4 this leads to a decrease of mean discharge for the duration of the tracer experiment.

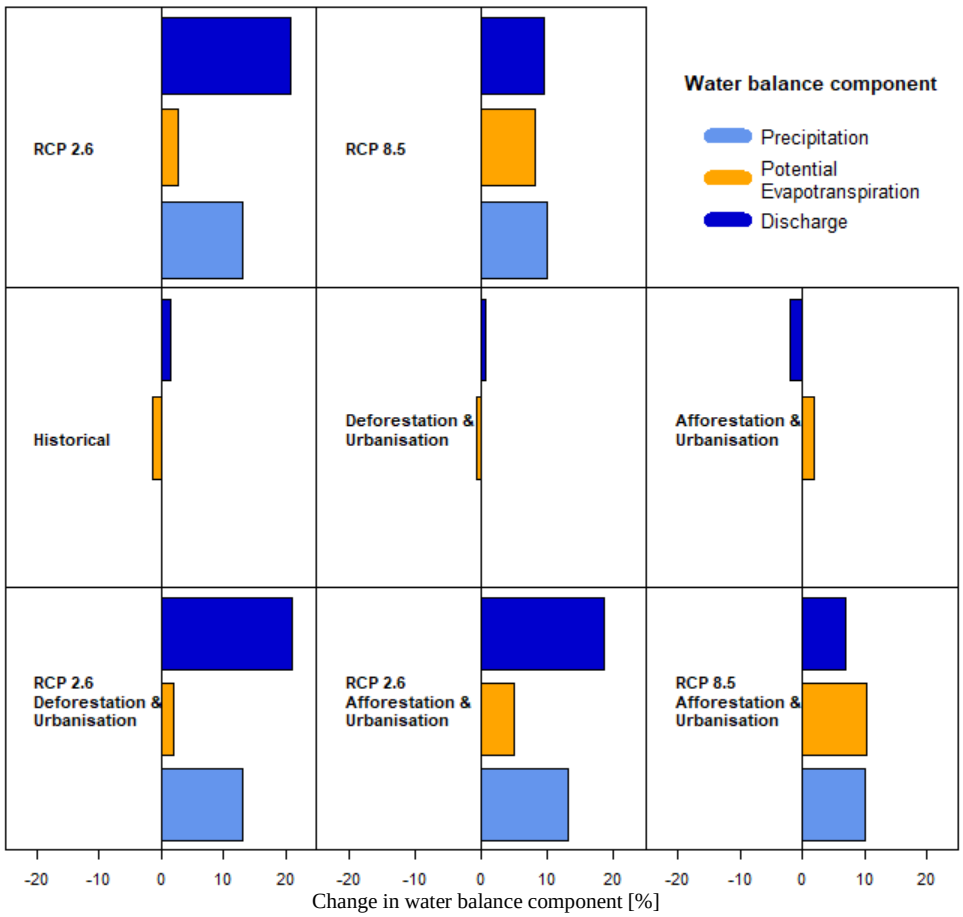

Figure 34: Changes in water balance components for T2

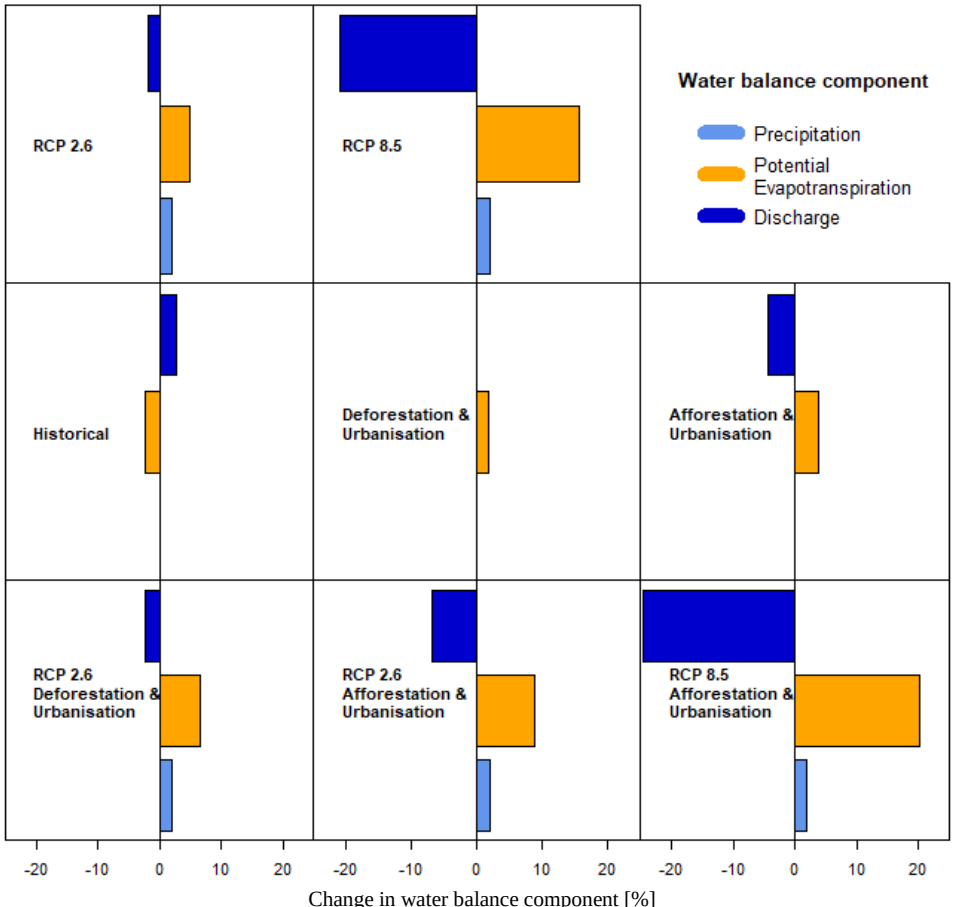

Figure 35: Changes in water balance components for T4

5. Discussion

5.1 Assumptions and resulting uncertainties

Several assumptions and simplifications are made in the modelling approach used in this thesis. They will be discussed in this paragraph as well as the ways in which uncertainties are assessed within the model. Starting with the climate scenarios, there is already a large uncertainty in the climate projections themselves. As it was previously shown, the ranges of the climate projections are rather wide and can differ a lot from the median of the projections. For temperature projections, the width of the uncertainty range can go up to 2.4 °C for the RCP8.5 predictions for autumn. However, all temperature projections show an increase in temperature for all meteorological seasons, even for the lowest uncertainty margin. The direction in which temperature changes will occur is therefore clear, only the extent of the changes is uncertain. For predicted changes in precipitation on the other hand, the uncertainty ranges mostly comprise relative changes below 1, which indicate a decline in precipitation, as well as relative changes above 1, which indicate an increase of precipitation. The only seasons where the direction of change in precipitation is clear are the summer of RCP2.6 with a clear decrease in precipitation, and the autumn of RCP2.6 as well as the winter of RCP8.5, with a clear increase of precipitation. The uncertainty ranges for both temperature and precipitation are wider for the RCP8.5 compared to the RCP2.6. For the RCP2.6 and the RCP8.5 climate scenarios, only the median of the climate projections is considered for the application to the discharge and transport model. The uncertainties within the possible changes of temperature or precipitation are not considered in these climate scenarios. Resulting changes in modelled discharge or transport are therefore only related to the median changes of the RCP scenarios and do not represent the possible impacts of the full range of climate projections. Another simplification applied for the climate scenarios is the delta approach with which the climate projections are considered. In the approach the seasonal mean changes of the climate projections are added to or subtracted from the original input time-series. In this way, only the mean seasonal changes in temperature or precipitation are considered. However, with changing climate conditions it is also possible that for instance the number of heavy precipitation events will increase as well (Pachauri and Mayer, 2015). But other possible effects of climate change besides mean seasonal changes in temperature and precipitation are not considered in the climate scenarios. This simplification can especially influence the modelled impacts of climate changes on karst contaminant vulnerability as those heavy precipitation events can lead to a fast increase of discharge in karst areas with especially high flow velocities, which pose a potential contamination thread to karst springs.

For the land-use scenarios, changes in land-use are only considered through a changed potential evapotranspiration. Other possible influences of different land-use types on the hydrological cycle, for instance through water storage by interception or through changed soil properties (Fohrer et al., 2016), are neglected. Furthermore, the Deforestation & Urbanization and Afforestation & Urbanization land-use scenarios are a simplification as they only consider changes in the shares of forest and urban areas and changes in grassland for compensation. The Historical scenario on the other hand considers changes in all land-use types. Also, the connection between climate and land-use changes are mostly not considered in the scenario analysis. Except for one land-use scenario, the Deforestation & Urbanization scenario, which is based on the study of Kovačič et al. (2020). They analysed observed climate-related land-use changes in the catchment of the Unica Springs. The extent of deforestation in the Deforestation & Urbanization scenario is based on their findings, which is a reduction in growing stock of forest areas. Therefore, the combined RCP2.6 and Deforestation & Urbanization scenario is a combination of direct and indirect effects of climate change. In both other combined scenarios, the climate scenarios are combined with the Afforestation & Urbanization scenario. Here, the land-use change is based on anthropogenic influences rather than on climate influences. Overall, there are many assumptions and simplifications made in the climate and land-use scenarios that need to be considered in the

interpretation of the scenario simulations. However, even though the scenarios are simplified, they are based on realistic possible future changes. Regarding the climate scenarios, the large uncertainties of the climate projections are not considered in the RCP2.6 or RCP8.5 scenarios, but they are assessed exemplary for the RCP8.5 in the climate uncertainty scenario. As the projection ranges of the RCP8.5 are wider than the projection ranges of RCP2.6, the uncertainty scenario therefore should access the maximum uncertainty through climate projections.

Also in the discharge modelling using the VarKarst model, there are some simplifications and assumptions made that need to be considered in the interpretation of the model results. Already in the calculation of the potential evapotranspiration for model input, several assumptions are made. As not all parameters necessary for the calculation were available at the Postojna meteorological station, many of them were derived from other available meteorological parameters using different equations as shown in the Chapter 3.2.1. The calculation of potential evapotranspiration is therefore based on approximations, which imply many assumptions. According to the FAO (1998), "no weather-based evapotranspiration equation can be expected to predict evapotranspiration perfectly under every climatic situation due to simplification in formulation and errors in data measurement". However, the FAO (1998) recommends the Penamn Monteith method for the calculation of potential evapotranspiration in order to achieve comparability between different scientific studies. This can therefore be accomplished in the method used in this thesis. Regarding the application of the climate scenarios, it also has to be noted that only the temperature input to the potential evapotranspiration calculation is changed for the scenario potential evapotranspiration. However, also changes in other meteorological parameters that are used for the calculation of potential evapotranspiration are possible with changing climate conditions. For instance, possible changes of relative humidity or daily sunshine duration due to changed cloud cover are not considered. The calibration of the VarKarst model with discharge data from the Hasberg gauging station is another potential source of uncertainty. As the station cannot measure discharges higher than 80 m³/s, there are no available high discharge data that the model can be calibrated to or that the model performance can be evaluated with. Of course also the discharge model itself is based on simplifications. The lumped structure of the model simulates the heterogeneity of the karst aquifer only globally, not taking into account the actual structure of the karst aquifer. The high complexity of karst systems is therefore only considered in a simplified way. Also, the parameters of lumped models can usually not be determined directly from physical, measureable processes (Mudarra et al., 2019). However, as the VarKarst model consists of several compartments, where the properties vary according to distribution functions, it can be described as a semi-distributed model. Especially through the estimation of the model parameter α_{SE} based on information on the actual distribution of soil depths within the catchment area, a spatial reference is added to the model simulations. Furthermore, in this way less parameters need to be estimated through calibration, decreasing the risk of over-parameterisation of the model. In addition, the model uncertainties are taken into account for discharge simulations as with the model calibration not one single parameter set is determined but a range of parameter sets according to a performance threshold. In his way, over-calibration can be avoided, where the model can be very optimised for the calibration period, but its performance can become much lower for other periods.

The uncertainties for tracer modelling already start at the preprocessing of the tracer test data. The actual measurements of tracer concentrations took place at the two springs separately and were then combined to one cumulative tracer breakthrough curve. This was done by Scheller (2020) by weighting the concentrations measured at the springs by their specific discharge. The combined tracer time series also needed to be in 6 hourly time steps in order to match the time-steps of the discharge model. The observed tracer concentrations were however measured in varying time-steps and not necessarily simultaneously at the two springs. Especially around the peak of observed tracer concentrations the interval of measurements was narrower than 6 hours. This combination of both breakthrough curves could therefore

have caused some inaccuracies. And also the recovered tracer mass was slightly affected by this preprocessing (Scheller, 2020). However, these inaccuracies can mostly be neglected as the breakthrough curves were standardized and simplified for the further analysis. Through the simplification, small inaccuracies did not have large consequences on the analysis. As the fit of the 1D-advection-dispersion model to the observed breakthrough curves is meant to simplify the breakthrough curves, it goes along with some assumptions. First, with the fit of the model to the observed breakthrough curves, it is assumed that the observed breakthrough curves represent full tracer recovery. The assumption here is that all tracer or contaminant that is injected in the catchment area will also reach the springs. This is however not the case for some of the tracer experiments. Second, the model assumes instantaneous tracer injection, which is only approximately the case for the tracer tests. For potential contaminants in the environment however, this is rarely the case (Chu et al., 2021). Third, the 1D-advection-dispersion model only models the main peak of the observed tracer breakthrough curves, secondary peaks are not considered. And last, the model does not consider retardation or reactive transport in any way. The modelled tracers or contaminants are therefore assumed to behave conservative. In the simulation of simplified tracer breakthrough curves based on the established correlations with discharge simulations and the estimated real distance from injection point to the springs, more simplifications were made. Again, the large complexity of the karst system is only considered in a very simplified way. The hydrological condition is considered for transport simulations through the mean discharge during the tracer experiment. However, it is only considered through a statistical relationship. Real processes that can occur in karst aquifers with varying flow conditions, for instance an inversion of flow directions, are not considered. Moreover, the estimated distance is of course only an estimated guess and the real flow distance is unknown. Furthermore, the uncertainties from the discharge simulations also affect the transport simulations that are based on them. However, these uncertainties are also considered in the transport simulations by again simulating a range of breakthrough curves rather than just one single curve. Overall, the approach for transport modelling is simplified in many ways. But as the goal is not to model an exact tracer breakthrough curve and model uncertainties are also assessed, many of these simplifications are reasonable. Furthermore, for every part of the method, model uncertainties are assessed and therefore included in the analysis.

5.2 Model evaluation

In the calibration of the VarKarst discharge model, very high KGE values of up to over 0.8 could be achieved. With all parameter sets that were selected for calibration, the mean KGE for the calibration period is very high with a value of 0.82. The respective mean KGE value for the validation period is also still high with a value of 0.71. And the decline of performance between the calibration period and the validation period is not too large. Thus, over-parametrisation could be avoided. In general, also the visual performance of the model can be described as very high in the calibration period as well as in the validation period because the observed discharge lies mostly within the model uncertainty bands. For the discharge peaks with Q>80 m³/s, the observed discharge shows plateaus. As previously described, this is caused by the inaccuracy of the observed data. Therefore, when the simulated discharge bands deviate from the observed discharge in those high peaks, it does not necessarily affect the model performance. However, these discharge plateaus were still considered in the model calibration, which is not ideal. For some smaller discharge peaks, the uncertainty bands do not entail the observed discharge. The modelled discharge reactions to precipitation input are therefore sometimes not strong enough. This might be partly associated with the consideration of the discharge plateaus at Q > 80 m³/s in the calibration, because this might have led to the preference of parameter sets that do not lead to too high discharge responses. In any way, an exclusion of the discharge plateaus from the calibration would have been preferable as they do not represent correct discharge measurements. Regarding parameter sensitivity, the mean epikarst storage coefficient K_{epi} was found to be the most sensitive parameter.

Within the parameter range up to 50 d, 90 % of the behavioural parameter sets have a K_{epi} of less than 10 d. And in the dotty plot in Figure 16 there is a clear pattern, which shows better performance values for smaller values of K_{epi}. This finding is coherent with other studies, where the best parameter values for K_{epi} were smaller than 3 d (Hartmann et al., 2016; Hartmann et al., 2014b). The two parameters V_{epi} and α_{fsep} show the least sensitivity in the analysis. The parameter V_{epi} is the mean storage capacity of the epikarst. However, even though there is no strong pattern for the behavioural parameter sets, there is a pattern for lower KGE values. The pattern shows that for V_{epi} values larger than 100 mm there are fewer low-performing parameter sets than for values below 100 mm. In literature, the best values for this parameter are also usually at the upper end of the calibration ranges, even higher than the calibration ranges in this thesis (Hartmann et al., 2014b; Mudarra et al., 2019). Therefore, the calibration ranges could maybe have been improved in this thesis by setting the upper range to a higher value. For the recharge separation distribution coefficient α_{fsep} Scheller (2020) describes that this parameter remained insensitive despite all adjustments and model developments so far. This is also the case in this thesis. The groundwater distribution coefficient α_{gw} as well as the conduit storage coefficient K_C were found to be sensitive parameters, but not as sensitive as the parameter K_{epi}. For both parameters, the parameter values with the best performance have similar values as in literature (Hartmann et al., 2014b; Mudarra et al., 2019). All calibrated parameters can therefore be considered to have reached reasonable values.

For the tracer simulations, the fit of the 1D-advection-dispersion model to the observed tracer breakthrough curves in Figure 25 clearly visualises the simplifications discussed earlier. The simplified curves reproduce only the general course of the breakthrough curves. For instance for T4 or T7, some single high concentration pulses in the breakthrough curves are not reproduced. For the transport simulations this could lead to an underestimation of possible maximum contaminant concentrations, which are essential for the assessment of contaminant vulnerability. However, it can be stated that the general course of all observed tracer breakthrough curves can be well represented by the simple model. Regarding the correlations between transport parameters and flow and site characteristics, the best correlation includes the mean discharge during the tracer experiment. This matches the important influence of the hydrological condition on transport in karst systems described previously. Higher mean discharges during the tracer experiment lead to smaller values of t_0 and to larger values of D_L. This can be connected to faster flow velocities at high water levels, leading to an earlier arrival time with higher turbulence and dispersion. This relationship where higher flow rates lead to higher flow velocities and higher dispersivities was for instance also found by Gabrovšek et al. (2010). The other parameter that is considered in the best correlations is the estimated actual distance form injection point to the Unica Springs. In case of the correlation with t_0 a larger estimated distance leads to lower values of t_0. This seems to be contradictory. One possible explanation could be that the estimated actual distances are based on known cave passages. Therefore, when the estimated actual distance of a tracer injection point is much longer compared to the linear distance, it could indicate that more explored cave passages are known between injection point and the Unica Springs. This could indicate a better connectivity of the conduit system between injection point and springs and partly explain the faster arrival times. However, the correlation analysis is not a physically based analysis, it is only statistical. And in statistics, correlation does not necessarily imply cause (Dormann, 2017). One other factor that could have influenced the correlations is the comparably short estimated actual distances of the tracer tests executed at low-water conditions. Compared to the other tracer tests, especially tracer tests T6 and T7 show quite short estimated actual distances (Table 1). These tracer tests were all executed at low water conditions and therefore have comparably large values of t_0. This could be a bias that influences this correlation. In any way, this emphasises the fact that the correlation analysis should be interpreted with care as it is a statistical method that is not directly based on physical processes. Applications of the correlations to other injection points or even study sides could therefore lead to misleading results. In this context, the

tracer tests T3, T5 and T8 are very valuable for the correlations as they are all injected at the same point within the catchment area. Therefore, other factors than the hydrological condition that could influence the correlations are limited. Furthermore, Ravbar et al. (2012) state that the in the tracer tests T6, T7 and T8 the observed transport velocities were among the lowest in karst literature. Their relevance for karst vulnerability assessment, where especially high flow velocities are of concern, is therefore maybe questionable. With the application of the correlations to predict the tracer breakthrough curves in Figure 29, tracer tests T2-T8 can mostly be reproduced within the model uncertainty. In case of T3 and T5, the observed breakthrough curves slightly differ from the simulated range. However, taking into account the different time and concentration scales for the different plots, at least the magnitude of the different tracer tests can be well reproduced for T2-T8. The simulations of tracer tests T1 and T9 however show the limitations of the modelling approach. Due to their special characteristics, they were excluded from the establishment of the correlations. In case of T1, the transport simulations cannot reproduce the complex observed tracer breakthrough curve. The arrival of all tracer is simulated for the first small peak of the complex, elongated observed breakthrough curve and therefore shows much higher concentrations. This complexity of the observed curve is also the reason why T1 was excluded from the establishment of correlations. And it shows that the transport simulation is not able to reproduce this complexity. For tracer test T9 another limitation of the modelling approach is shown. T9 was excluded from the correlation establishment because of the especially long distance of its injection point from the Unica Springs compared to the other tracer tests. The tracer simulations for T9 based on the correlations lead to unreasonably small values for t_0 and unreasonably large values for D_L. Therefore, it is not possible to simulate reasonable tracer breakthrough curves for this tracer test. This might be partly caused by the statistical nature of the approach discussed earlier. As the approach is not directly based on physical processes, the application outside of the calibration conditions can be difficult and misleading.

5.3 Quantitative vulnerability assessment through transport modelling

In this paragraph, the classification of the approach used in this thesis among the different available karst vulnerability methods as well as its applicability and transferability will be discussed. In the classification of different karst vulnerability assessment methods, intrinsic vulnerability and specific vulnerability are distinguished. Intrinsic vulnerability is aquifer specific and independent of the contaminant whereas specific vulnerability is based on a certain contaminant (Zwahlen, 2004; Iván and Mádl-Szőnyi, 2017). The approach in this thesis is based on the data of several tracer tests that were conducted in the catchment area. One assumption that was made during the analysis is that the tracers are considered to behave conservative. Therefore, this approach does not consider the contaminant properties. It only simulates transport of a soluble, non-reactive contaminant and thus assesses intrinsic vulnerability. According to Daly et al. (2002), three aspects need to be considered for intrinsic vulnerability assessment: the advection time, the relative contaminant amount that reaches the target and the occurring physical attenuation through for example dilution or dispersion. While the approach in this thesis does simulate the advection time as well as the dispersion, and therefore the attenuation, it does not simulate the relative contaminant amount that reaches the target. As mentioned before, the contaminant is assumed to be non-reactive in this approach. Decay or degradation of the contaminant are therefore not assessed and full tracer recovery is assumed. Another assumption that was made in the analysis is that all tracer or contaminant that is injected within the catchment area is transported to the Unica Springs. Due to their large heterogeneity, it is possible in karst aquifers that flow directions change with the hydrological conditions and that the recharge area is very variable (Ravbar et al., 2012; Stevanović, 2015). These processes are however not considered in this approach. For contaminant recovery, the transport simulation therefore represents the worst case scenario, which is also the safest scenario for vulnerability assessment. Regarding the origin-pathway-target model of the “European approach” (Zwahlen, 2004), the approach in this thesis considers the target, which are the Unica Springs

in this case, as well as the pathway, from injection point to the springs. The pathway is considered indirectly through the distance to the springs. The origin or hazard refers to activities that can lead to the potential release of a contaminant. In case of this study site, possible hazards could for instance be the military training area at Poček or the settlements in the karst poljes or in the Pivka valley. They are maybe also considered in an indirect way as the tracer injection points in some cases reflect points where contaminants could potentially be released. For instance tracer test T1 was deliberately conducted in the military training area. Tracer tests T3, T5 and T8 are injected into the Pivka River, which can also be potentially polluted by settlements. The injection of T4 into the oil collector also specifically takes place at a location with a high risk of pollution as it deliberately collects and drains polluted water from the highway. And the injection of T2 at Mala Karlovica can reflect possible contamination from the settlements the Cerkniško polje. In the differentiation between source and resource vulnerability the approach used in this study can be described as a source vulnerability assessment approach as tracer breakthrough curves are simulated at the Unica Springs, which are the source in this case. Resource vulnerability on the other hand would describe only the way of the contaminant vertically to the groundwater surface (Iván and Mádl-Szőnyi, 2017). In the transport model, transport in the unsaturated zone from the surface to the groundwater and transport in the saturated zone to the Unica Springs are not distinguished. This is the case because the tracer tests that the method is based on are not all injected in the same way. Some tracer tests are directly injected into sinking rivers whereas others are injected into the vadose zone. However, all tracer tests have in common that they are injected in a way that the soil layer is avoided. Therefore, as the transport model is based on the tracer tests, this implies that the soil layer is not considered in the transport model. In this context, the transport model could maybe be extended to an integrated approach. By coupling the transport model with a vulnerability mapping method for the catchment area, which considers spatial properties that can lead to a bypassing of the soil layer, the approach could probably be improved. For the classification of the approach of this thesis according to the classes proposed by Iván and Mádl-Szőnyi (2017), it can be described as a quantitative method as the result of the approach is a range of simplified breakthrough curves at the Unica Springs. One of the main advantages of quantitative vulnerability methods is the possibility of a simple validation. The importance of this validation is for instance also emphasised by the COST Action 620 (Daly et al., 2002). The quantitative nature of the approach used in this thesis potentially allows for a simple validation of the model. However, tracer tests T2-T8 are all used for the establishment of the correlations and therefore used for the calibration of the method. They are mostly well reproduced by the model, but they are not independent data. Tracer tests T1 and T9 were specifically left out of the analysis because of their special characteristics. They are not well reproduced by the model, but they were also expected to behave different from the other tracer tests. An additional validation of the modelling approach would therefore be preferable, for instance by another tracer test. The approach can furthermore be partly described as a process-based or physically based method. The basis for the approach is the VarKarst model, which is a process-based discharge model. And also the 1D-advection-dispersion model that is used for the transport simulation is based on the mathematical solution to the 1D transport equation and therefore describes a physical process. However, the correlations used in the approach are a statistical method. Overall, the approach is therefore a mixture of a physically based and a statistical method. Theoretically, the modelling approach can estimate transport of a tracer or contaminant from any point in the catchment for any period of time when the injection can bypass the soil and when an estimation of the actual distance from the injection point to the Unica Springs is known. However, the statistical part of the methodology makes the application outside of the calibration conditions more questionable. Again, another validation of the method would be helpful. Especially for the application of the method to other study sites, the statistical part limits the transferability of the approach. The correlation is calibrated to exactly the conditions of the catchment of the Unica Springs. According to Focazio (2002), statistical methods are usually applied for specific contaminant issues at

local scales. Therefore, for the application to other study sites, enough tracer test data would need to be available in order to establish new correlations for the specific study site.

The need for the development of more process- and physically based approaches to assess karst vulnerability in a quantitative way was one of the main motivations for this thesis. The developed approach can partly fulfil this goal as it provides a quantitative way of vulnerability assessment. It is however only partly physically based and partly statistical. This limits the transferability of the approach outside of the calibration conditions. But the approach is able to reproduce the influence of the hydrological condition on contaminant transport and can therefore model the temporal variation of vulnerability. Thus, another main goal for this thesis could be achieved by the developed approach, which is the consideration of the hydrological conditions in the transport simulation. In this way, the temporal variation of vulnerability and therefore the impacts of environmental changes on transport can be assessed. This is not possible using qualitative or semi-quantitative vulnerability methods and even not all quantitative vulnerability methods can consider this. For instance the VULK method by Jeannin et al. (2001) or the Time-input method by Kralik and Keimel (2003) do not account for the hydrological conditions in vulnerability assessment. Another advantage of the approach used in this thesis is the simulation of advection processes, which are essential for the assessment of contaminant arrival times and therefore for vulnerability assessment. For instance the vulnerability method by Butscher and Huggenberger (2008) or the VarKarst-based approach by Mudarra et al. (2019) cannot account for advection processes in tracer transport. The approach of this thesis therefore contributes to the development of more quantitative vulnerability methods. But as the approach is a very simple method based on many assumptions and is partly based on statistical methods, there is still a need for continuous improvements in this field of quantitative vulnerability methods.

5.4 Modelled impacts of climate and land-use change

In this paragraph, the results of the scenario analysis of discharge and transport modelling will be discussed with regards to the methodology used in this thesis as well as in comparison to other literature in this context. For the results of the discharge simulations with climate scenarios RCP2.6 and RCP8.5 the water balances of the analysed time-series show a mean increase of all components, of discharge as well as of precipitation and of potential evapotranspiration (Figure 22). The changes in precipitation and in potential evapotranspiration are predetermined by the scenario input manipulation. The potential evapotranspiration for the climate scenarios is calculated based on the manipulated temperature time-series. Temperatures are projected to increase in every meteorological season in both scenarios. And with an increase in temperature also the calculated potential evapotranspiration increases. For the RCP8.5 scenario this increase is even larger than for the RCP2.6 scenario. For scenario precipitation, the original precipitation time-series is manipulated according to the seasonal projected changes in precipitation. For the RCP2.6 and RCP8.5 scenarios only the median changes are considered. For precipitation, the median changes lead to an increase in precipitation for spring, autumn and winter. The season with the most increase in precipitation for both scenarios is winter. The second-highest increase is in spring and the lowest increase is in autumn with a median increase of only 2 % for both climate scenarios. For summer the projected median changes lead to a decrease of precipitation for both scenarios. The observed time-series in Figure 22 on which the discharge scenarios are based starts in May 2008 and ends in September 2009. Summer is therefore overrepresented in the time-series and winter is underrepresented. However, the mean precipitation over the whole time-series still increases for both scenarios. For the RCP8.5 scenario this increase is however less pronounced than for the RCP2.6. The mean discharge for the time-series is based on the discharge simulations by the VarKarst model with applied climate scenario input. As there is an increase in precipitation as well as in potential evapotranspiration, the discharge could potentially increase or decrease, depending on which process prevails. For both the RCP2.6 scenario as well as the RCP8.5 scenario the mean discharge over the

exemplary time-series increases. The increase of precipitation therefore has a larger impact on the discharge than the increase of temperature and therefore of potential evapotranspiration. This emphasises the importance of the precipitation projections. The precipitation projections are however afflicted with more uncertainty than the temperature projections as their ranges mostly entail values that lead to precipitation increase as well as decrease (Table 3). The increase of mean discharge for the time-series is however less pronounced for the RCP8.5 scenario than for the RCP2.6 scenario as the increase in potential evapotranspiration is higher and the increase in precipitation is lower for the RCP8.5 scenario. While there is clearly an increase in the mean discharge of the time-series for both climate scenarios, the simulated time-series show a large overlap of the uncertainty bands of the initial simulations with the climate scenario simulations. The model uncertainty is therefore larger than the predicted changes caused by the climate scenarios. However, in some periods the scenario simulations reach higher values at the top of the uncertainty band as well as on the bottom of the uncertainty band than the initial discharge simulations. This indicates a shift of discharge simulations towards higher values. However, as the uncertainty bands still overlap, the shifts are not larger than model uncertainty. These shifts towards higher discharge simulations can mostly be observed for the high discharge peaks of the time-series in winter and spring. As previously described, the projected median increase in precipitation for these two seasons is higher than for the seasons summer and autumn. The seasonal input manipulation pattern is therefore reflected in the scenario discharge simulations. For discharge simulations in summer and autumn, some shifts can be observed towards lower discharge simulations, especially for the RCP8.5. For scenario simulations in autumn, the projected increase in temperature therefore prevails over the slight projected increase in precipitation. These shifts for summer and autumn are however not as pronounced as the shifts towards higher discharge simulations in winter and spring. In general, the shifts of the uncertainty bands are most pronounced for discharge peaks. This can be associated to the higher precipitation amounts which are necessary to cause peaks in discharge. The scenario precipitation is calculated based on projections of relative changes in precipitation, not on absolute changes. Thus, when high precipitation amounts occur in the initial time-series, the absolute increase of precipitation is higher than for lower initial precipitation amounts. And this can therefore also lead to bigger changes in simulated discharge for peak discharges.

For the climate uncertainty scenario, exemplary for RCP8.5 also the ranges of the climate projections were considered in the analysis. The water balance shows that the resulting ranges of the predicted changes in water balance components are very wide. While the mean change of potential evapotranspiration for the analysed time-series is always positive and just varies in its extent, the mean precipitation changes vary from a decrease to a high increase. Also the resulting changes in mean discharge range from a decrease in discharge to a very high increase of discharge. The respective uncertainty band of the discharge simulations is therefore very wide. It completely entails the initial discharge simulations. Due to the complete overlap of both uncertainty bands, no statement can be made about the direction of future changes. This climate uncertainty scenario therefore emphasised that the climate scenarios RCP2.6 and RCP8.5 are only representative for the median of the projected changes. They do not represent the climate projections with their whole spectrum of possible changes. Also further transport analysis that are based on the RCP2.6 scenario and the RCP8.5 scenario are only valid for the median values of the projections. This high uncertainty in climate change projections that leads to unclear expected changes for discharge is also emphasised by Sapač et al. (2019). They however also came to similar results for the discharge characteristics of two karst rivers in Slovenia as the RCP2.6 and RCP8.5 climate scenarios that were discussed in this thesis. They state that while they found that mean discharge as well as the magnitude of extreme events could increase, low-flow could still decrease due to a decrease of summer precipitation. The study by Wu et al. (2017) on the other hand found that for their study side in Southwest China, there was a continuous decrease of precipitation and of discharge. This shows that climate-related changes can vary a lot between different regions and that

there is no uniform pattern of expectable changes. This stresses the importance of the execution of climate-impact studies in different regions around the world.

For all land-use scenarios, the mean changes of the water balance components for the analysed time-series are much smaller than the mean changes of the climate scenarios. As the land-use scenarios do not influence the amount of precipitation, the precipitation input is not manipulated and there are no changes for this water balance component. The land-use types are only considered through the calculation of the potential evapotranspiration. The changes in potential evapotranspiration therefore differ between the different land-use scenarios and lead to changes in discharge. For the Afforestation & Urbanisation scenario, a mean increase in potential evapotranspiration and therefore a mean decrease in discharge can be observed. This is likely caused by the increased share of forests as they are the land-use type that leads to the highest potential evapotranspiration rates. Therefore, in the Deforestation & Urbanisation scenario, the opposite changes can be observed with a decrease of the mean potential evapotranspiration leading to a mean increase of discharge for the time-series. For the Historical land-use scenario, there is also a decrease of mean potential evapotranspiration and an increase of mean discharge. The share of forest in this scenario is also smaller than in the initial conditions, which could partly cause this similar shift. For the simulated discharge time-series, the uncertainty bands of all land-use discharge simulations almost completely overlap with the initial uncertainty bands. No shifts of the discharge simulations can be observed, which indicates that the changes caused by different land-use compositions are very small compared to the model uncertainty. This low impact of the land-use scenarios could partly be caused by the fact that in the VarKarst model the land-use types are only considered in the calculation of the potential evapotranspiration. Therefore, as discussed before, other effects of land-use changes, like a changed interception or soil properties are not accounted for by the model. Furthermore, already for the climate scenarios it was shown that the impacts of changes in potential evapotranspiration are smaller than the impacts of changes in precipitation. And the precipitation input is not altered by the land-use composition in the catchment. The significant impact of land-use changes on the spring hydrology found by Kovačič et al. (2020) therefore cannot be represented by the model. However, similarly to the much smaller effects of land-use changes compared to climate changes found in this study, also Wu et al. (2017) found in their analysis that the contribution of climatic factors to discharge changes was much stronger than the contribution of anthropogenic activities.

As the climate scenarios have a much larger impact on the discharge simulations than the land-use scenarios, they dominate the results of the combined scenarios. In the mean changes of the water balance components it can however be observed that the Afforestation & Urbanisation scenario slightly reduces the effects of the climate scenarios on the mean discharge. The Deforestation & Urbanisation on the other hand slightly enhances the effects of the climate scenarios on the mean discharge. This should be valid especially for the seasons of winter and spring. For the seasons of summer and autumn however, the combined effects of the climate scenario input changes lead to a decrease of discharge. In this case, the Afforestation & Urbanisation scenario can enhance the decrease of discharge whereas the Deforestation & Urbanisation scenario can reduce the decrease of discharge.

In the simulation of the scenario breakthrough curves, the climate and land-use scenarios are considered over the changes of mean discharge during the tracer experiment. Therefore, the scenario transport modelling is dependent on the scenario discharge modelling. Thus, in the same way as for the scenario discharge simulations, the impacts of the climate scenarios on the transport simulations are much stronger than the impacts of the land-use scenarios. And the combined scenarios are always dominated by the climate scenarios. This connection between discharge and transport scenarios is exemplary shown for tracer tests T2 and T4, where the changes in the water balance components are calculated for the duration of the tracer experiments (Figure 34 and Figure 35). The transport parameters and therefore the

simulated breakthrough curves are calculated based on the established correlations, which include the mean discharge during the tracer experiment. For tracer test T2 this therefore shows how the increased discharge of the climate scenarios for the period of the tracer experiment leads to a shift of the simulated breakthrough curve ranges towards earlier arrival times with higher maximum concentrations. In this way, the climate scenarios lead to an increased vulnerability of the Unica Springs to contamination. For the climate scenarios it can be noted that tracer test T2 is executed in spring. Therefore, this increased vulnerability can be associated with the projected increasing precipitation in spring and winter. The changes of the water balance components for the period of tracer experiment T2 for the land-use scenarios are again much smaller than the changes for the climate scenarios. The Afforestation & Urbanisation scenario is the only scenario here that leads to a decrease of the mean discharge. A very small shift towards later arrival times with lower concentrations can be observed in the respective simulated range of breakthrough curves.

The impact of the land-use scenarios on the transport simulations is the same for all tracer tests because the impact of the land-use change on the discharge simulations is not dependent on the season. Only the extent of the changes can vary slightly as the seasonality of vegetation is considered in the calculation of potential evapotranspiration. The Afforestation & Urbanisation scenario leads to a very small shift of the simulate breakthrough curve ranges towards later arrival times for all tracer tests. The other two land-use scenarios on the other hand always lead to very small shifts towards faster arrival times. Based on this observation it could be stated that more forests in the catchment area lead to a decrease of spring vulnerability to contamination. The simulated changes are however very small compared to the model uncertainty. In the analysis of the impact of land-use on the vulnerability of the Unica Springs to contamination in this study, the focus was only on the impact of land-use on transport. In the objective environment, land-use can also influence other aspects of vulnerability, for instance through changed filtration or even through changed contaminant input, e.g. in case of cropland or urban areas. The simulated differences between contaminant transport characteristics of different land-use compositions in this thesis are not sufficient to make a clear statement about which land-use composition is preferable regarding spring vulnerability to contamination. However, according to Glavan et al. (2013), generally forest is “the most environmentally acceptable land-use” regarding water quality.

For tracer test T4, the changes in the water balance components for the period of the tracer experiment are in general smaller than for T2. For climate scenario RCP8.5 however, a strong decrease of the mean discharge during the tracer experiment is simulated. Even though there is a slight increase in precipitation, the increase in potential evapotranspiration is much larger and leads to an overall decrease in discharge. The respective simulated range of breakthrough curves is therefore shifted towards later arrival times with lower maximum concentrations. This can indicate a slight decrease of spring vulnerability to contamination. Tracer test T4 is injected in autumn and the tracer experiment extends until winter. This partial execution in autumn and in general after summer and autumn can be associated with the decrease in mean discharge. For instance also for T1, which is injected in summer, the climate scenario transport simulations show a similar shift towards later arrival times, also especially for the RCP8.5 scenario. The same is true for tracer test T5, which was injected at the same time as tracer test T4. Tracer test T3 was injected at the same time as tracer test T2. The simulated changes of the climate scenarios therefore follow the same pattern as for T2. For tracer tests T6, T7 and T8, the simulated changes in the transport simulations are small, even for the climate scenarios. Regarding the climate uncertainty scenario, it is unclear in the discharge simulation whether discharge will increase or decrease. Therefore, the development of transport for the climate uncertainty scenario is also unclear. For all tracer tests, the simulated climate uncertainty ranges completely contain the initial simulated ranges of breakthrough curves. This effect is also described by Butscher and Huggenberger (2009b), where they state that the large uncertainties of regional climate models can interfere with the

uncertainties of the groundwater models. The analysis of future impacts of climate change thus becomes very difficult.

The results of the scenario analysis for contaminant transport show tendencies towards an increase of the vulnerability of the Unica Springs with climate change due to increasing precipitation and discharge in winter and spring. For summer and autumn, decreasing discharges lead to a tendency towards a decreased vulnerability of the Unica Springs according to the approach used in this thesis. Similar findings were made by the analysis of the impact of changing climate conditions on source vulnerability by Butscher and Huggenberger (2009b). For their "summer heat wave" scenario, which resembles the predictions for summer and autumn in this thesis, they also found a decrease of conduit flow vulnerability. For their "severe rainfall event" scenario, which can be associated with the predictions for winter and spring in this thesis, they also found that directly after the event conduit flow vulnerability increases. However, they state that for the long-term also the "severe rainfall event" scenario leads to a slight decrease of conduit flow vulnerability due to enhanced dilution. In this study, the standardised breakthrough curves are simulated. Possible dilution effects are therefore not analysed. If the same mass of tracer or contaminant is injected and the standardised concentration is the same, an increased discharge during the tracer experiment leads to a lower absolute concentration of tracer or contaminant at the spring. This relation would need to be further analysed in order to improve the estimation of spring vulnerability with the approach of this thesis. However, the earlier transport arrival times which are caused by the increase of discharge in winter and spring still lead to an increased spring vulnerability despite the neglected possible dilution effect. The advection time is not assessed by the approach of Butscher and Huggenberger (2009b).

For all tracer tests under all applied scenarios, model uncertainty is rather wide. There is no scenario or tracer test where the simulated changes between scenario and initial transport are larger than the model uncertainty. However, shifts can be observed, which can in winter and spring lead to a faster arrival time of contaminants with higher maximum concentrations. Thus, with changing climate conditions in certain periods there is a tendency towards an increased vulnerability of the Unica Springs to contamination. This shows the importance of further analysis on the impacts of environmental changes on karst contamination vulnerability, especially for changing climate conditions, in order to ensure a safe and sustainable management of karst water resources in the future. Because despite many simplifications in the approach of this study resulting in large uncertainties, it could be shown that climate change can pose a potential thread to karst spring vulnerability to contamination.

6. Conclusion

In this thesis, a new approach for contaminant transport modelling in a karst aquifer was developed based on the VarKarst discharge model. Using observed tracer test data, correlations between transport parameters and flow and site characteristics were established. These correlations were then used in order to simulate transport parameters, and therefore simplified breakthrough curves. The transport parameters were estimated based on information on the injection location within the catchment and on discharge simulations by the VarKarst model. Through the calculation of potential evapotranspiration with the Penman Monteith method, the land-use composition in the catchment area was considered in the VarKarst model. Furthermore, simple climate scenarios, land-use scenarios and combined scenarios were established for the catchment area. Based on them the original input data was manipulated and applied to the discharge and transport models. The resulting simulations of discharge and transport under changed climate and land-use conditions were compared to the discharge and transport simulations with initial conditions. As an important part of modelling, the occurring uncertainties were also included in the analysis. For one exemplary climate scenario, uncertainties in future climate projections were assessed and in discharge and transport simulations model uncertainty was accounted for.

The results of the analysis show that most observed discharge time-series and tracer tests could be reproduced within the model uncertainty. The model uncertainty is however large and limitations of the model through many implied simplifications and through its partly statistical methodology were also shown. In the application of the climate and land-use scenarios to the discharge and transport modelling it was found that changes in climate input have a stronger impact on the simulation results than changes in land-use. For the climate scenarios, especially the changes in precipitation had the most impact on discharge and transport simulations. For both climate scenarios an increase of the mean discharge for the analysed time-periods was found. The changes in discharge however vary over the time-series according to the seasonal differences in scenario input manipulation. The simulated changes for the land-use scenarios very small compared to the model uncertainty so that for the discharge and tracer simulations, hardly any changes could be observed. In general, the uncertainty ranges of the scenario simulations and the uncertainty ranges of the initial simulations overlapped for all scenario analysis, indicating that simulated changes were never larger than the model uncertainty. In addition, the climate uncertainty scenario showed that the RCP2.6 and RCP8.5 scenario simulations are only valid for the projected median changes. When also the uncertainty of climate projections was accounted for, the uncertainty became even larger. However, shifts in the discharge and transport simulations could be observed. For transport simulations in winter and spring, these changes led to faster solute transport with earlier arrival times and higher maximum concentrations of potential contaminants. Thus, an increase of the vulnerability of the Unica Springs to contamination could be possible in the future based on the model.

This shows the importance of the assessment of climate and land-use change impacts on karst vulnerability, as they could pose a possible thread on karst water resources, especially if the resources are used for drinking water supply. It also emphasises the need for the consideration of the hydrological conditions in karst vulnerability assessment in order to make such analysis possible. The approach used in this thesis can be seen as a contribution to the development of more quantitative vulnerability assessment methods, which also include different hydrological conditions in the vulnerability assessment. But it also shows the need for continuous improvements in the further development of methods with less limitations. And it especially emphasises the need for further analysis on climate and land-use change impacts on karst water resources.

References

Aller, L., Lehr, J.H., Petty, R., Bennett, T., 1987. DRASTIC: a standardized system to evaluate groundwater pollution potential using hydrogeologic settings. Journal of the Geological Society of India 29, 23–37.

Andreo, B., Vías, J., Durán, J.J., Jiménez, P., López-Geta, J.A., Carrasco, F., 2008. Methodology for groundwater recharge assessment in carbonate aquifers: application to pilot sites in southern Spain. Hydrogeol J 16 (5), 911–925.

ARSO, 2021a. ARHIV - opazovani in merjeni meteorološki podatki po Sloveniji. https://meteo.arso.gov.si/met/sl/archive/. Accessed November 25, 2021.

ARSO, 2021b. Arhiv hidroloških podatkov - dnevni podatki. http://vode.arso.gov.si/hidarhiv/pov_arhiv_tab.php?p_vodotok=Unica. Accessed October 1, 2021.

Bakalowicz, M., 2005. Karst groundwater: a challenge for new resources. Hydrogeol J 13 (1), 148–160.

Beaujean, J., Lemieux, J.-M., Dassargues, A., Therrien, R., Brouyère, S., 2014. Physically based groundwater vulnerability assessment using sensitivity analysis methods. Ground water 52 (6), 864–874.

Bertalanič, R., Dolinar, M., Draksler, A., Honzak, L., Kobold, M., Kozjek, K., Lokošek, N., Medved, A., Vertačnik, G., Vlahović, Ž., Žust, A., 2018. Ocena podnebnih sprememb v Sloveniji do konca 21. stoletja. Sintezno poročilo – prvi del.

Bertalanič, R., Dolinar, M., Honzak, L., Lokošek, N., Medved, A., Vertačnik, G., Vlahović, Ž., 2019. Climate change projections for Slovenia over the 21st century: Temperature and precipitation summary. http://meteo.arso.gov.si/met/en/climate/. Accessed October 31, 2021.

Blatnik, M., Frantar, P., Kosec, D., Gabrovšek, F., 2017. Measurements of the outflow along the eastern border of Planinsko Polje, Slovenia. Acta Carsologica 46 (1), 83–93.

Brenner, S., Coxon, G., Howden, N.J.K., Freer, J., Hartmann, A., 2018. Process-based modelling to evaluate simulated groundwater levels and frequencies in a Chalk catchment in south-western England. Nat. Hazards Earth Syst. Sci. 18 (2), 445–461.

Butscher, C., Huggenberger, P., 2008. Intrinsic vulnerability assessment in karst areas: A numerical modeling approach. Water Resour. Res. 44 (3), 161.

Butscher, C., Huggenberger, P., 2009a. Enhanced vulnerability assessment in karst areas by combining mapping with modeling approaches. The Science of the total environment 407 (3), 1153–1163.

Butscher, C., Huggenberger, P., 2009b. Modeling the temporal variability of karst groundwater vulnerability, with implications for climate change. Environmental science & technology 43 (6), 1665–1669.

Chu, X., Ding, H., Zhang, X., 2021. Simulation of solute transport behaviors in saturated karst aquifer system. Scientific reports 11 (1), 1–17.

Daly, D., Dassargues, A., Drew, D., Dunne, S., Goldscheider, N., Neale, S., Popescu, I., Zwahlen, F., 2002. Main concepts of the "European approach" to karst-groundwater-vulnerability assessment and mapping. Hydrogeology Journal 10 (2), 340–345.

Doerfliger, N., Jeannin, P.-Y., Zwahlen, F., 1999. Water vulnerability assessment in karst environments: a new method of defining protection areas using a multi-attribute approach and GIS tools (EPIK method). Environmental Geology 39 (2), 165–176.

Dormann, C.F., 2017. Parametrische Statistik. Verteilungen, maximum likelihood und GLM in R. Springer Berlin Heidelberg, Berlin, Heidelberg.

FAO, 1998. Crop evapotranspiration. Guidelines for computing crop water requirements, Rome.

Field, M.S., Nash, S.G., 1997. Risk assessment methodology for karst aquifers: (1) Estimating karst conduit-flow parameters. Environmental Monitoring and Assessment 47, 1–21.

Fiorillo, F., 2014. The Recession of Spring Hydrographs, Focused on Karst Aquifers. Water Resour Manage 28 (7), 1781–1805.

Focazio, M.J., 2002. Assessing ground-water vulnerability to contamination. Providing scientifically defensible information for decision makers. U.S. Dept. of the Interior U.S. Geological Survey; U.S. Geological Survey Information Services, Reston, Va, Denver, CO.

Fohrer, N., Bormann, H., Miegel, K., Casper, M., Bronstert, A., Schumann, A.H., Weiler, M. (Eds.), 2016. Hydrologie. Haupt Verlag; UTB GmbH, Bern, Stuttgart.

Ford, D., Williams, P.W., 2007. Karst hydrogeology and geomorphology. John Wiley & Sons, Chichester, England, A Hoboken, NJ.

Foster, S., Hirata, R., 1988. Groundwter pollution risk assessment : a methodology using available data. CEPIS, Lima.

Gabrovšek, F., Kogovšek, J., Kovačič, G., Petrič, M., Ravbar, N., Turk, J., 2010. Recent results of tracer tests in the catchment of the Unica river (SW Slovenia). Acta Carsologica 39 (1), 27–37.

Geyer, T., 2008. Process-based characterisation of flow and transport in karst aquifers at catchment scale. Dissertation, Georg-August-Universität zu Göttingen, Göttingen.

Ghasemizadeh, R., Hellweger, F., Butscher, C., Padilla, I., Vesper, D., Field, M., Alshawabkeh, A., 2012. Review: Groundwater flow and transport modeling of karst aquifers, with particular reference to the North Coast Limestone aquifer system of Puerto Rico. Hydrogeology Journal 20 (8), 1441–1461.

Ghasemizadeh, R., Yu, X., Butscher, C., Hellweger, F., Padilla, I., Alshawabkeh, A., 2015. Equivalent Porous Media (EPM) Simulation of Groundwater Hydraulics and Contaminant Transport in Karst Aquifers. PloS one 10 (9), 1-21.

Glavan, M., Miličić, V., Pintar, M., 2013. Finding options to improve catchment water quality—Lessons learned from historical land use situations in a Mediterranean catchment in Slovenia. Ecological Modelling 261-262, 58–73.

Goldscheider, N., 2000. The PI method – a GIS-based approach to mapping groundwater vulnerability with special consideration of karst aquifers. Zeitschrift für angewandte Geologie 46 (3), 157–166.

Goldscheider, N., Drew, D. (Eds.), 2007. Methods in karst hydrogeology. Taylor & Francis, London.

Gupta, H.V., Kling, H., Yilmaz, K.K., Martinez, G.F., 2009. Decomposition of the mean squared error and NSE performance criteria: Implications for improving hydrological modelling. Journal of Hydrology 377 (1-2), 80–91.

Hartmann, A., Barberá, J.A., Lange, J., Andreo, B., Weiler, M., 2013. Progress in the hydrologic simulation of time variant recharge areas of karst systems – Exemplified at a karst spring in Southern Spain. Advances in Water Resources 54, 149–160.

Hartmann, A., Goldscheider, N., Wagener, T., Lange, J., Weiler, M., 2014a. Karst water resources in a changing world: Review of hydrological modeling approaches. Rev. Geophys. 52 (3), 218–242.

Hartmann, A., Kobler, J., Kralik, M., Dirnböck, T., Humer, F., Weiler, M., 2016. Model-aided quantification of dissolved carbon and nitrogen release after windthrow disturbance in an Austrian karst system. Biogeosciences 13 (1), 159–174.

Hartmann, A., Mudarra, M., Andreo, B., Marín, A., Wagener, T., Lange, J., 2014b. Modeling spatiotemporal impacts of hydroclimatic extremes on groundwater recharge at a Mediterranean karst aquifer. Water Resour. Res. 50 (8), 6507–6521.

Iván, V., Mádl-Szőnyi, J., 2017. State of the art of karst vulnerability assessment: overview, evaluation and outlook. Environ Earth Sci 76 (3), 13.

Jeannin, P.-Y., Cornaton, F., Zwahlen, F., Perrochet, P., 2001. VULK: a tool for intrinsic vulnerability assessment and validation. Sciences et techniques de l'environnement. Mémoire hors-série, 185–190.

Kaufman, G., Mayaud, C., Kogovšek, B., Gabrovšek, F., 2020. Understanding the temporal variation of flow direction in a complex karst system (Planinska Jama, Slovenia). AC 49 (2-3).

Kaufmann, G., Gabrovšek, F., Turk, J., 2016. Modelling flow of subterranean Pivka River in Postojnska Jama, Slovenia. Acta Carsologica 45 (1), 57–70.

Kogovšek, J., Knez, M., Mihevc, A., Petric, M., Slabe T., Šebela, S., 1999. Military training area in Kras (Slovenia). Environmental Geology 38 (1).

Kovačič, G., Petrič, M., Ravbar, N., 2020. Evaluation and Quantification of the Effects of Climate and Vegetation Cover Change on Karst Water Sources: Case Studies of Two Springs in South-Western Slovenia. Water 12 (11), 3087.

Kovačič, G., Ravbar, N., 2010. Extreme hydrological events in karst areas of Slovenia, the case of the Unica River basin. Geodinamica Acta 23 (1-3), 89–100.

Kralik, M., Keimel, T., 2003. Time-input, an innovative groundwater-vulnerability assessment scheme: application to an alpine test site. Environmental Geology 44 (6), 679–686.

Leibundgut, C., 2009. Tracers in hydrology. Wiley-Blackwell, Chichester, UK, Hoboken, NJ.

Maček, U., Bezak, N., Šraj, M., 2018. Reference evapotranspiration changes in Slovenia, Europe. Agricultural and Forest Meteorology 260-261 (2), 183–192.

Malík, P., 2015. Evaluating Discharge Regimes of Karst Aqifer. In: Z. Stevanović (Editor), Karst Aquifers—Characterization and Engineering. Springer, Cham.

Mayaud, C., Gabrovšek, F., Blatnik, M., Kogovšek, B., Petrič, M., Ravbar, N., 2019. Understanding flooding in poljes: A modelling perspective. Journal of Hydrology 575 (2), 874–889.

Monteith, J.L., 1965. Evaporation and environment. Symposia of the Society for Experimental Biology 19, 205–234.

Moreno-Gómez, M., Pacheco, J., Liedl, R., Stefan, C., 2018. Evaluating the applicability of European karst vulnerability assessment methods to the Yucatan karst, Mexico. Environ Earth Sci 77 (19), 51.

Mudarra, M., Hartmann, A., Andreo, B., 2019. Combining Experimental Methods and Modeling to Quantify the Complex Recharge Behavior of Karst Aquifers. Water Resour. Res. 55 (2), 1384–1404.

Niu, G.-Y., Yang, Z.-L., Mitchell, K.E., Chen, F., Ek, M.B., Barlage, M., Kumar, A., Manning, K., Niyogi, D., Rosero, E., Tewari, M., Xia, Y., 2011. The community Noah land surface model with multiparameterization options (Noah-MP): 1. Model description and evaluation with local-scale measurements. J. Geophys. Res. 116 (D12), 1381.

Pachauri, R.K., Mayer, L. (Eds.), 2015. Climate change 2014: Synthesis report. Contribution of Working Groups I, II and III to the Fifth Assessment Report of the Intergovernmental Panel on Climate Change. IPCC, Geneva, Switzerland.

Penman, H.L., 1948. Natural evaporation from open water, hare soil and grass. Proceedings of the Royal Society of London. Series A, Mathematical and physical sciences 193 (1032), 120–145.

Perko, D., Ciglič, R., Zorn, M., 2020. The Geography of Slovenia. Springer International Publishing, Cham.

Petrič, M., Kogovšek, J., Ravbar, N., 2018. Effects of the vadose zone on groundwater flow and solute transport characteristics in mountainous karst aquifers - The case of the Javroniki-Sneznik massif (SW Slovenia). Acta Carsologica 47 (1), 35–51.

Ravbar, N., Barberá, J.A., Petrič, M., Kogovšek, J., Andreo, B., 2012. The study of hydrodynamic behaviour of a complex karst system under low-flow conditions using natural and artificial tracers (the catchment of the Unica River, SW Slovenia). Environ Earth Sci 65 (8), 2259–2272.

Ravbar, N., Kovačič, G., Petrič, M., Kogovšek, J., Brun, C., Koželj, A., 2018. Climatological trends and anticipated karst spring quantity and quality: case study of the Slovene Istria. Geological Society, London, Special Publications 466 (1), 295–305.

Ravbar, N., Mayaud, C., Blatnik, M., Petrič, M., 2021. Determination of inundation areas within karst poljes and intermittent lakes for the purposes of ephemeral flood mapping. Hydrogeol J 29 (1), 213–228.

Sapač, K., Medved, A., Rusjan, S., Bezak, N., 2019. Investigation of Low- and High-Flow Characteristics of Karst Catchments under Climate Change. Water 11 (5), 925.

Sarrazin, F., Hartmann, A., Pianosi, F., Rosolem, R., Wagener, T., 2018. V2Karst V1.1: a parsimonious large-scale integrated vegetation–recharge model to simulate the impact of climate and land cover change in karst regions. Geosci. Model Dev. 11 (12), 4933–4964.

Scheller, M., 2020. Evaluation of karst vulnerability methods by tracer tests and modeling. Master thesis, Albert-Ludwigs University of Freiburg, Freiburg.

Stevanović, Z. (Ed.), 2015. Karst Aquifers—Characterization and Engineering. Springer, Cham.

Stevanović, Z., Eftimi, R., 2010. Karstic sources of water supply for large consumers in Southeastern Europe – sustainability, disputes and advantagesty. Geologia Croatia 63 (2), 179–185.

Vesper, D.J., Loop, C.M., White, W.B., 2003. Contaminant transport in karst aquifers. Speleogenesis and Evolution of Karst Aquifers 1 (2), 1–11.

Vrba, J., Zaporožec, A. (Eds.), 1994. Guidebook on mapping groundwater vulnerability. Heise, Hannover.

White, W.B., Herman, J.S., Herman, E.K., Rutigliano, M., 2018. Karst Groundwater Contamination and Public Health. Springer International Publishing, Cham.

Wu, L., Wang, S., Bai, X., Luo, W., Tian, Y., Zeng, C., Luo, G., He, S., 2017. Quantitative assessment of the impacts of climate change and human activities on runoff change in a typical karst watershed, SW China. The Science of the total environment 601-602, 1449–1465.

Yang, Z.-L., Niu, G.-Y., Mitchell, K.E., Chen, F., Ek, M.B., Barlage, M., Longuevergne, L., Manning, K., Niyogi, D., Tewari, M., Xia, Y., 2011. The community Noah land surface model with multiparameterization options (Noah-MP): 2. Evaluation over global river basins. J. Geophys. Res. 116 (D12), 4257.

Živanović, V., Jemcov, I., Dragišić, V., Atanacković, N., Magazinović, S., 2016. Karst groundwater source protection based on the time-dependent vulnerability assessment model: Crnica springs case study, Eastern Serbia. Environ Earth Sci 75 (17), 749.

Zwahlen, F. (Ed.), 2004. COST action 620. Vulnerability and risk mapping for the protection of carbonate (karst) aquifers : final report. Office for Official Publications of the European Communities, Luxembourg.

Declaration

Hiermit versichere ich, Tamara Leins,

dass ich die eingereichte Masterarbeit selbständig verfasst habe, keine anderen als die angegebenen Quellen und Hilfsmittel benutzt und alle wörtlich oder sinngemäß aus anderen Werken übernommenen Inhalte als solche kenntlich gemacht habe.

Die eingereichte Masterarbeit ist oder war weder vollständig noch in wesentlichen Teilen Gegenstand eines anderen Prüfungsverfahrens.

_____ _____

Datum, Ort Unterschrift

Appendix

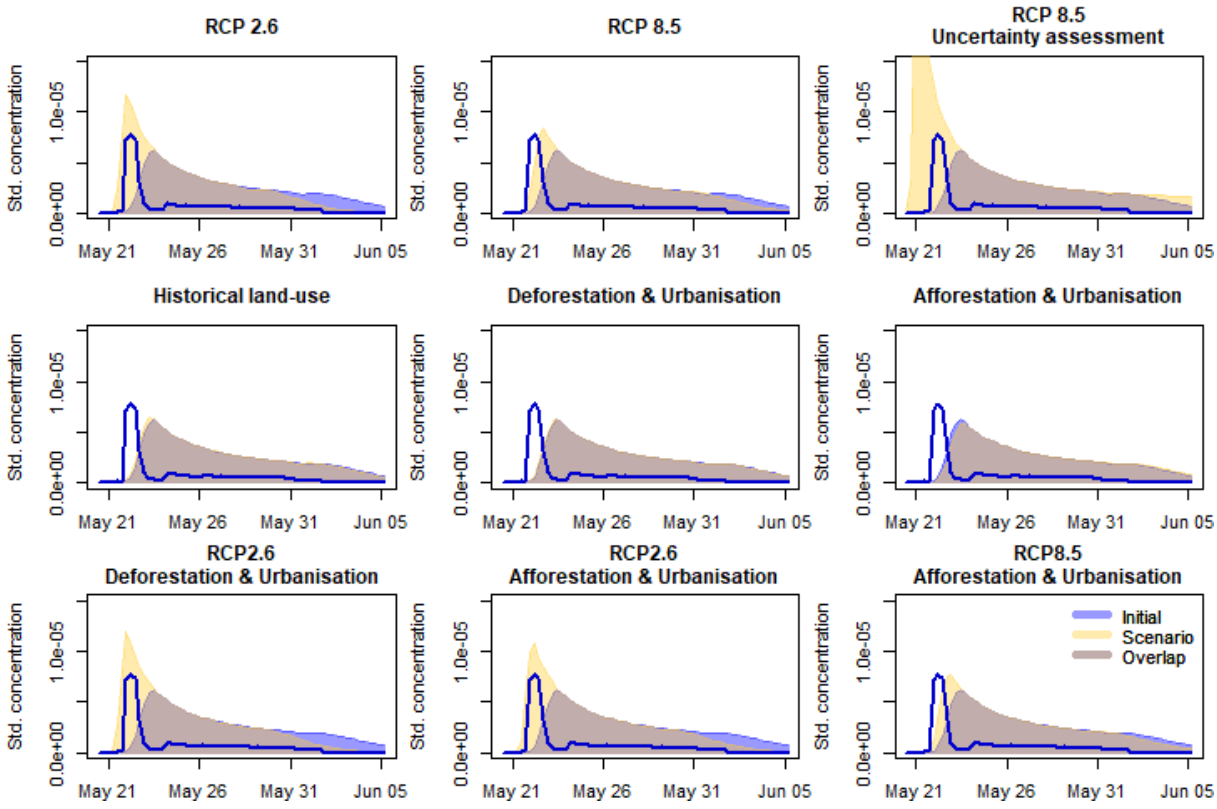

Figure 36: Tracer breakthrough curve simulations with climate and land-use scenarios including tracer breakthrough curve simulations with initial conditions for T3

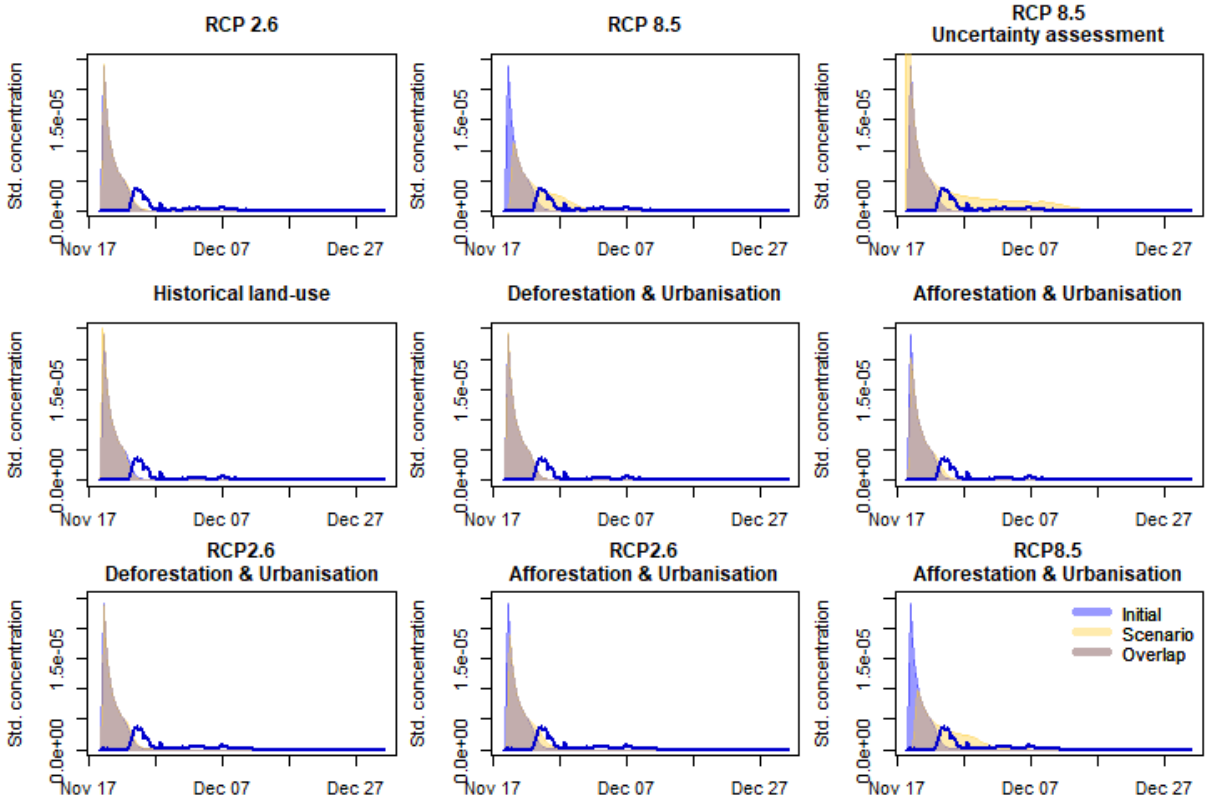

Figure 37: Tracer breakthrough curve simulations with climate and land-use scenarios including tracer breakthrough curve simulations with initial conditions for T5

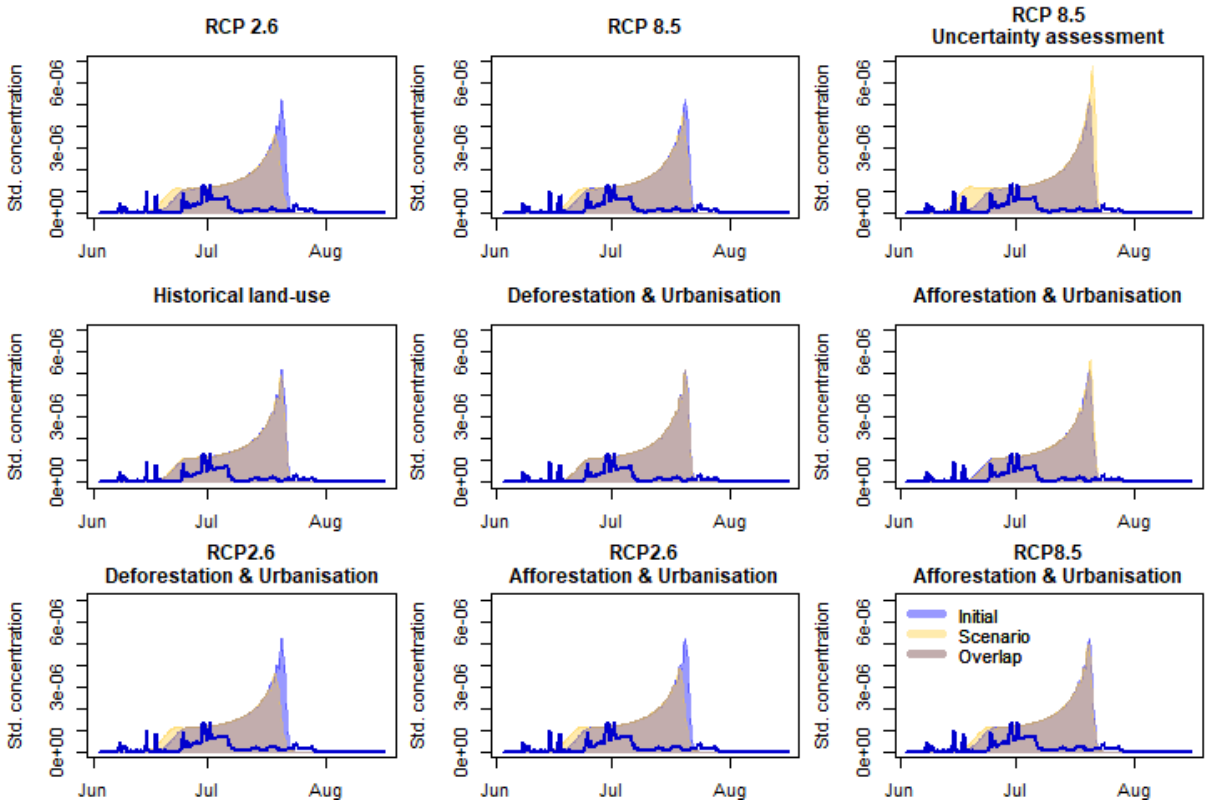

Figure 38: Tracer breakthrough curve simulations with climate and land-use scenarios including tracer breakthrough curve simulations with initial conditions for T7

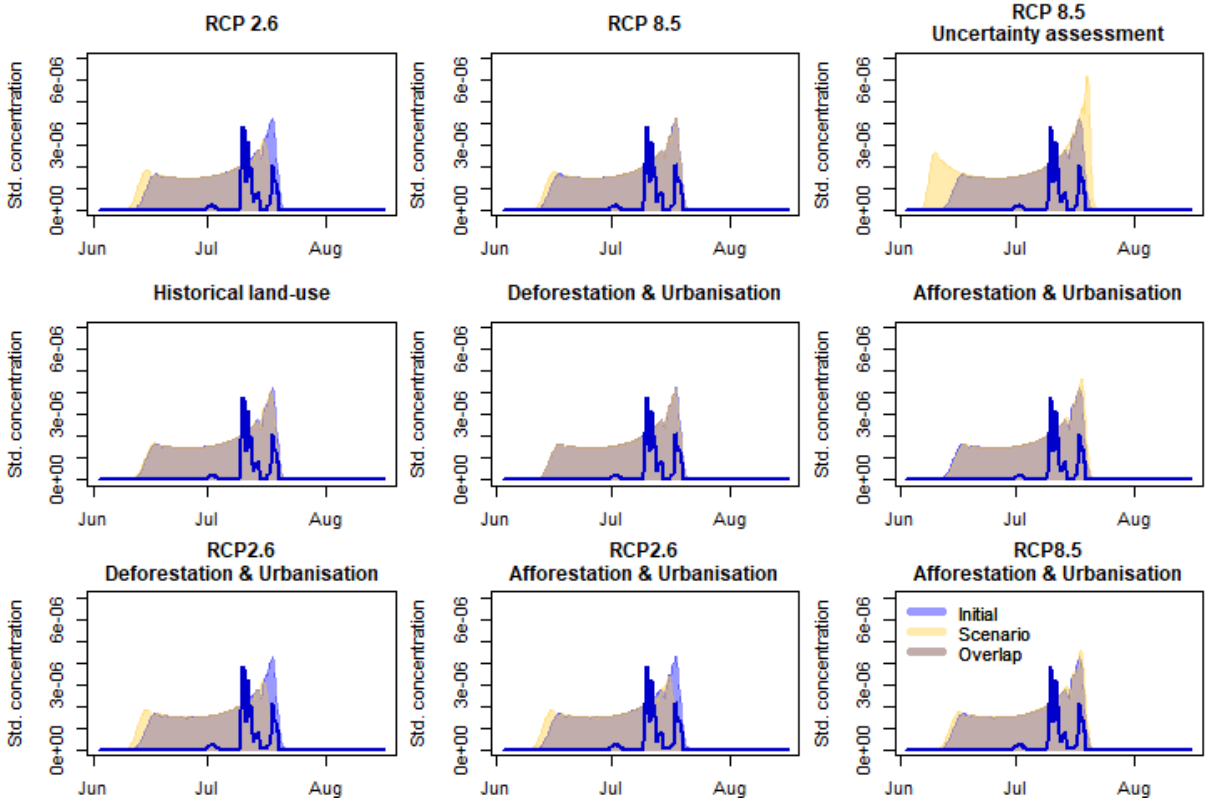

Figure 39: Tracer breakthrough curve simulations with climate and land-use scenarios including tracer breakthrough curve simulations with initial conditions for T8